Characterizing and Comparing the ADS Maneuver Execution Subsystem Performance of Two Vehicles

Joseph-Brandon Bueno Gopiao

Thesis submitted to the faculty of the Virginia Polytechnic Institute and State University in partial fulfillment of the requirements for the degree of

Master of Science
In
Mechanical Engineering

Zachary Doerzaph, Chair
Warren Hardy, Co-Chair
Azim Eskandarian

01 May 2023
Blacksburg, Virginia

Keywords: automated vehicles, motion control systems, vehicle dynamics, AV testing

Characterizing and Comparing the ADS Maneuver Execution Subsystem Performance of Two Vehicles

Joseph-Brandon Bueno Gopiao

ABSTRACT

Automated driving systems (ADS) are projected to bring a plethora of benefits to society, such as enhanced road safety and heightened quality of life. However, placing one's trust in the hands of an automated system is still a large concern to society. To facilitate the large-scale adoption of ADSs, they must be stringently tested and evaluated prior to their deployment on public roadways due to their direct impact on the safety of other motorists and vulnerable road users. Currently, no standardized method of quantifying ADS performance exists, so this research project contributes to the evaluation of ADSs by developing and demonstrating a test method that solely characterizes the motion control subsystem of an ADS. The developed test method involved generating representative driving scenarios that exercised both the longitudinal and lateral control elements of an ADS. This method was then demonstrated using two test vehicles with different control system architectures by (1) defining and injecting a ground truth trajectory into the ADS, (2) characterizing the motion control subsystem by quantifying its ability to follow the ground truth path under both nominal conditions and conditions where disturbances were introduced, and (3) analyzing the response of each vehicle to characterize their respective control systems as well as identify differences between the two control architectures.

First, a set of representative driving scenarios was created to test the longitudinal and lateral control elements both in isolation and in tandem. Multiple unique design variations of each scenario were created by implementing various target speeds, accelerations, and turning radii that map to both standard and emergency maneuvers. The parameters were set to match naturalistic driving or regulatory requirements identified as part of a literature review. Next, a reference trajectory—the ground truth set of waypoints that define the position and speed of the ADS—was generated for each driving scenario. This reference trajectory was implemented using three methods: recording the waypoint trail of a human driver and creating a synthetic waypoint list mathematically or with CarMaker, a simulation platform for automobile testing (IPG Automotive 2021). Once this step was completed, the reference trajectory was inserted into the ADS to isolate the motion control system and facilitate a repeatable test input. When the test vehicle was under ADS control, the experimenter served as the designated fallback user so they

could take control of the vehicle if necessary. Finally, a set of test metrics related to the operation of the ADS (lateral offset, heading error, speed error, longitudinal stop position error, and test completion percentage) were calculated using kinematic data to characterize each motion control system architecture.

The analysis of the kinematic metrics for each test scenario demonstrated that the method could effectively evaluate the performance of ADS in various scenarios and highlight the strengths and weaknesses of each system. The control system of Vehicle A consistently lagged in throttle and brake actuation and rounded corners by turning early and with a larger cornering radius. This control system also could not exceed a lateral acceleration of 3.5 m/s^2 when under ADS control and limited its yaw rate to keep the lateral acceleration below this level. Consequently, this limitation caused the vehicle to turn wide for radius and speed combinations with a lateral acceleration greater than 3.5 m/s^2. On the other hand, the control system of Vehicle B consistently exhibited a small delay before turning and tended to overshoot lane changes at higher lateral accelerations. Regarding disturbances, only the road grade significantly affected the response of both vehicles.

Characterizing and Comparing the ADS Maneuver Execution Subsystem Performance of Two Vehicles

Joseph-Brandon Bueno Gopiao

GENERAL AUDIENCE ABSTRACT

Automated driving systems (ADS) are projected to improve road safety and quality of life, but they must be comprehensively tested and evaluated before their deployment on public roadways. Currently, no standardized method of quantifying ADS performance exists, so this research project contributes to the evaluation of ADSs by developing and demonstrating a test method that identifies limitations of two dissimilar ADS motion controllers.

First, real-world driving scenarios were used to test the longitudinal (throttle/brake) and lateral (steering) control elements both in isolation and in tandem. Multiple levels of maneuver harshness were tested to simulate both standard and emergency maneuvers, and these levels were determined by conducting a literature review of human driving behavior. Roadway and vehicle disturbances were also implemented to investigate if the control systems could adjust for external factors. Next, a reference path was generated for each driving scenario using three separate methods, and once this was done, the vehicle attempted to follow the reference path. Finally, a set of test metrics related to the path-following ability of the ADS were calculated, and this data was used to characterize each motion control system architecture.

The analysis of metrics demonstrated that the method could effectively evaluate the performance of each control system by highlighting their weaknesses. The control system of Vehicle A consistently accelerated and braked late as well as rounded corners by turning early and with a larger radius. This control system also could not complete harsh cornering maneuvers. On the other hand, the control system of Vehicle B consistently turned late and tended to overshoot lane changes, especially those with a higher speed or harsher steering maneuver. Regarding disturbances, only the road grade significantly affected the response of both vehicles.

ACKNOWLEDGMENTS

Regarding project acknowledgments, a big thank-you goes to thank Loren Stowe, one of the Co-PIs on the ADS Maneuvers project, for granting me the opportunity to contribute towards the project and use it as a thesis topic for my M.S. Mechanical Engineering degree. I would also like to thank Jonathan Cowan and Joshua Quesenberry, two senior research associates at Virginia Tech Transportation Institute, for their tremendous help with the data collection and processing stages of this project as well as debugging issues with the test vehicles. Lastly, I would like to acknowledge the National Highway Traffic Safety Administration (NHTSA) for funding this work.

I would also like to thank Dr. Luke Riexinger and the SAFETY IMPACT Lab for giving me the chance to present two conference presentations on head-on vehicle crashes at the Association for the Advancement of Automotive Medicine 66th Annual Scientific Conference in Portland, Oregon, and the 27th International Technical Conference on the Enhanced Safety of Vehicles in Yokohama, Japan. During these conferences, I was able to learn and network with great minds in industry, government, and academia, all while exploring a new area and forming deeper connections with the rest of the lab.

As my sixth and final year at Virginia Tech comes to an end, I would like to acknowledge my family for making me the person I am today and for supporting me in many facets of life. In addition to my family, a shout-out goes to the many friendships I've made throughout this Blacksburg adventure. Whether it was through class, work, graduate school, the Filipino-American Student Association, the Society of Hip-Hop Legacy, or escapades in downtown Blacksburg, I feel extremely lucky to have great friends that have made the lows less low and the highs even higher.

DEDICATION

This work was completed in memoriam of Clay. You transformed my dream of pursuing a graduate degree into a reality and introduced me to the fascinating world of vehicle safety and crash data analytics. I will forever be grateful for your mentorship, friendship, and dedication to making our roadways a safer place for both motorists and pedestrians alike. You are greatly missed by so many.

Dr. Hampton Clay Gabler III

31 January 1954 – 11 January 2021

TABLE OF CONTENTS

LIST OF FIGURES

LIST OF TABLES

1 BACKGROUND

1.1 Introduction

For many decades, the idea of an autonomous vehicle (AV), otherwise known as a self-driving vehicle or driverless vehicle) was seen as nothing more than science-fiction. Whether the AV was a driverless passenger vehicle, light rail vehicle, aircraft, boat, submarine, or unmanned autonomous vehicle (UAV), successfully deploying an AV into the real world appeared to be impossible because it tasked a computer with navigating a complex, dynamic environment under various conditions while remaining vigilant of its surroundings (Sarmento et al., 2017). However, significant advancements in the computational capabilities of both hardware and software technologies have greatly benefitted intelligent transportation systems, transforming the concept of a self-driving vehicle into a tangible engineering challenge (Frazzoli et al., 2002).

Many of these technological strides have been facilitated by a tremendous amount of funding from both private and public stakeholders; this may include private companies and investors, original equipment manufacturers (OEMs), and insurance companies for the former, and academic institutions, government bodies, national labs, and non-profit organizations for the latter (Doerzaph, 2022). Regarding autonomous passenger vehicles, an estimated $220 billion has been invested since 2010 across four main spheres encompassing the future of mobility: autonomous driving, connected cars, electrified vehicles, and smart mobility (Holland-Letz et al., 2019). This combination of enormous funding and increased research and development efforts have made modern vehicles more powerful than ever—now able to acquire and process more data, utilize more sophisticated hardware architectures, and implement more robust vehicle control methods, artificial intelligence algorithms, and data fusion techniques (Sarmento et al., 2017). A report from Statista predicts that one in 10 passenger vehicles across the globe will be self-driving by the year of 2030 (Statista DossierPlus, 2019), so driverless vehicles must accurately understand and predict a vast range of human driving behaviors to successfully preserve the safety of its passengers and surrounding vehicles or pedestrians.

The large-scale deployment of fully autonomous passenger vehicles is projected to bring about many benefits to society, with the most prominent benefits comprising of crash prevention, traffic alleviation, and cost savings (Urmson & Whittaker, 2008; Karnouskos, 2020; Daily et al., 2017). According to the National Motor Vehicle Crash Causation Survey (NMVCCS), a study

conducted between 2005 and 2007 that investigated the factors related to pre-crash events, the critical cause of almost 94% of passenger vehicle crashes was attributed to driver errors, which are categorized in Table 1 and Table 2 (NHTSA, 2015). These mistakes can be mitigated by an AV because they do not experience fatigue or perform irresponsible driving behaviors like humans.

Table 1. Frequency of driver-related causation factors according to NMVCCS

Critical Reason	Number	Percentage ± 95% Confidence Limits
Recognition error	845,000	41% ±2.2%
Decision error	684,000	33% ±3.7%
Performance error	210,000	11% ±2.7%
Non-performance error	145,000	7% ±1.0%
Other	162,000	8% ±1.9%
Total	2,046,000	100%

Table 2. Description of driver-related causation factors according to NMVCCS

Critical Reason	Description
Recognition error	• Inattention • Distractions (internal, external) • Inadequate surveillance
Decision error	• Driving too fast for road geometry or conditions • False assumption of others' actions • Misjudgment of gap spacing or others' speed • Aggressive driving • Illegal maneuver
Performance error	• Overcompensation • Poor directional control • Panicking/freezing
Non-performance error	• Physical impairment • Critical health condition (e.g., heart attack) • Drowsiness/sleeping due to fatigue • Unconsciousness due to alcohol or drugs

Additionally, autonomous passenger vehicles are also expected to relieve traffic congestion. Crashes causing roadway bottlenecks are one of the main causes of traffic, so decreasing the frequency of crashes will inherently decrease traffic congestion. However, there are also many instances when traffic congestion occurs despite the obvious presence of any

external factors, known as a phantom traffic jam (Malvin & Pudjaprasetya, 2020). When the average vehicle density on a roadway exceeds a critical value of approximately 25 vehicles per kilometer, these types of traffic jams can be triggered by minor disturbances, such as a driver braking due to being distracted or the negligent behavior of other drivers. Over time, the phantom traffic jam naturally accumulates and propagates down the road, and it is exacerbated by a chain of delayed driver reaction times to the congestion (Bando et al., 1995). As fully autonomous vehicles become more available and accessible, it can be concluded that the frequency of phantom traffic jams will decrease for the same reasons as decreasing crash frequency: human error and reaction time will be eliminated.

Reducing the amount of vehicle crashes and occurrence of traffic also promises associated cost and environmental benefits. The 2019 Traffic Safety Facts report published by the National Highway Traffic Safety Administration (NHTSA) estimates that the economic cost of police-reported and unreported crashes in 2010 was approximately $242 billion (NHTSA, 2021). Similarly, the National Safety Council (NSC) Injury Facts report estimates that the calculable costs of motor-vehicle crashes (costs associated with vehicle damage, medical expenses, wage and productivity losses, administrative expenses, and employers' uninsured costs) can range between a few thousand dollars to almost $1.8 million per crash depending on the crash severity (NSC, 2022). Regarding traffic savings, the 2021 Urban Mobility Report determined that traffic congestion in urban areas forced travel delays aggregating to 8.7 billion hours, which corresponded to 3.5 billion gallons of excess fuel consumption in 2019. Furthermore, this excess fuel consumption was estimated to cost a total of $190 billion and produce 36 million tons of greenhouse gas emissions (Schrank et al., 2021). The advancement of AVs, and later their production and accessibility, will yield a decrease in the wastage of both economic and environmental resources and an increase in quality of life for all members of society.

1.2 Defining Levels of Automation

Currently, the SAE International Standard no. J3016, "Taxonomy and Definitions for Terms Related to Driving Automation Systems for On-Road Motor Vehicles," is the most widely accepted document providing a taxonomy of the six levels of on-road vehicle automation: levels

0 – 5, with L0 corresponding with no driving automation and L5 describing full driving automation (SAE International, 2021). A summary of each can be seen in Table 3.

Table 3. SAE J3016 levels of driving automation

<table>
<tr><td>0</td><td>1</td><td>2</td><td>3</td><td>4</td><td>5</td></tr>
<tr><td colspan="3">You <u>are</u> driving whenever these driver support features are engaged, even if your feet are off the pedals and you are not steering</td><td colspan="3">You <u>are not</u> driving whenever these driver support features are engaged, even if you are sitting in “the driver’s seat”</td></tr>
<tr><td colspan="3" rowspan="2">You must constantly supervise these support features; you must steer, brake, or accelerate as needed to maintain safety</td><td>When the feature requests,</td><td colspan="2" rowspan="2">These automated driving features will not require you to take over driving</td></tr>
<tr><td>you must drive</td></tr>
<tr><td colspan="3">Driver Support Features</td><td colspan="3">Automated Driving Features</td></tr>
<tr><td>Limited to providing warnings and momentary assistance</td><td>Provide steering or brake or acceleration support</td><td>Provide steering and brake or acceleration support</td><td>Features can drive the vehicle under limited conditions and will not operate unless all requirements are met</td><td colspan="2">Same as L4, but features can drive anywhere in all conditions</td></tr>
</table>

The standard also thoroughly defines terminology that are necessary for describing actions, concepts, and considerations required to operate a motor vehicle. An important concept that is extensively and repeatedly mentioned in SAE J3016 is the dynamic driving task (DDT), which is defined as the operational and tactical functions that must be performed in real-time to successfully operate a vehicle in the presence of other moving and stopped vehicles. The DDT may include the following subtasks: lateral and longitudinal motion control (steering and longitudinal acceleration), maneuver planning, object and event detection and response (OEDR), and increasing conspicuity by using signals, lighting, and gesturing when necessary. The complete driving task (Figure 1) includes the strategic functions that must be taken by the driver in addition to the DDT, such as planning the time of reaching the destination and selecting an optimal route.

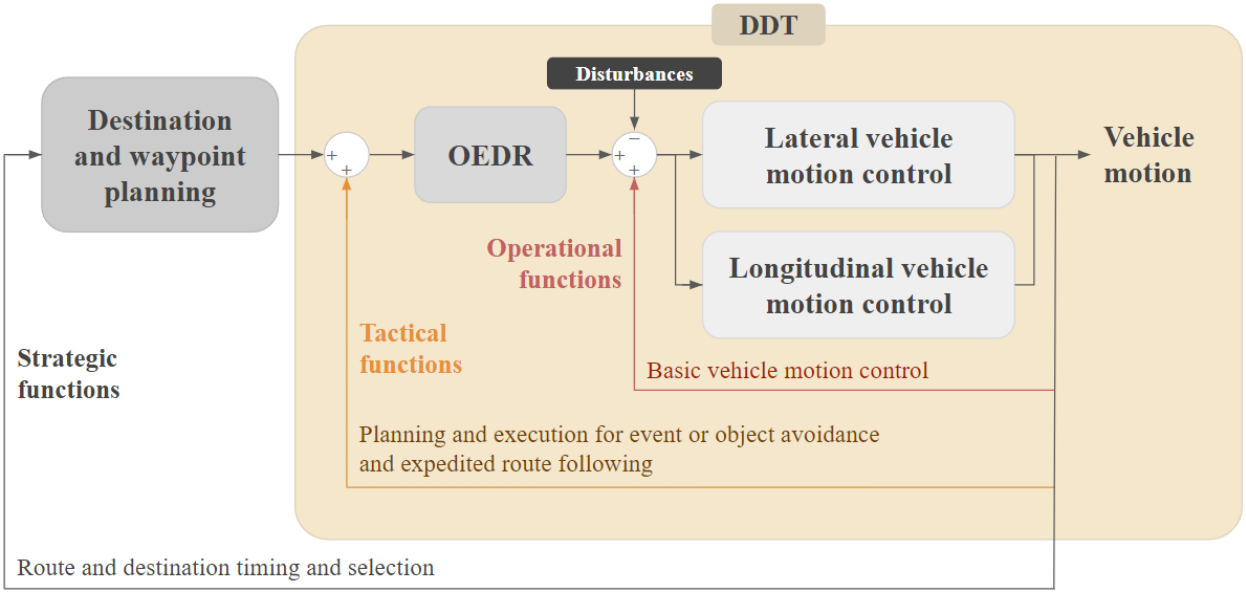

Figure 1. Block diagram describing the entire driving task

The standard also defines the operational design domain (ODD) as the set of conditions that a driving feature or system are specifically designed to operate. This may include restrictions on time-of-day, weather conditions, traffic volume, or geographical position. Automation Levels L0 to L2 contain only driver support features, so the human is always responsible for partially or entirely completing the DDT, and the automated features will always be operating under a restricted ODD. On the other hand, automated driving systems (ADS) are capable of L3 to L5 automation, so the ADS is entirely responsible for the DDT. However, if a DDT performance-relevant system failure occurs, or the vehicle exits its intended ODD, a DDT fallback has been defined as the response that must be taken by the human or the system to achieve what SAE J3016 has defined as a "minimal risk condition." In L3, the ADS performs the entire DDT, but the human may be designated as the DDT fallback-ready user, requiring them to take control of the vehicle and achieve a minimal risk condition before transferring control back to the ADS. Automation levels L4 and L5 designate the ADS as the DDT fallback-ready user, so it is entirely responsible for transporting the passengers and are not required to have steering or longitudinal acceleration controls. However, the only difference between these levels is the fact that L4 is constrained to a specific ODD while L5 can perform the same actions under any ODD.

1.3 Functional Decomposition of a Typical ADS

The functional architecture of an automated driving system (ADS) can be broken into three core competencies that allow an ADS to successfully navigate complex, dynamic environments: perceive, plan, and maneuver (Behere & Torngren, 2015). An overview of all three systems and how they interact with each other is presented in Figure 2.

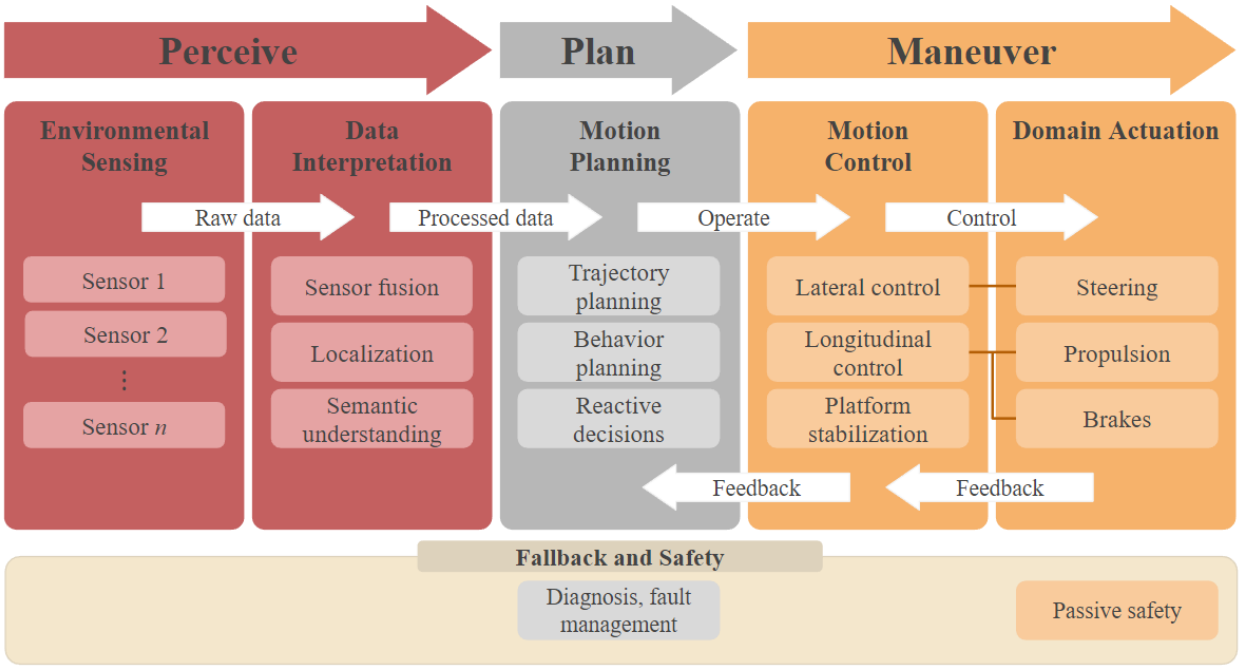

Figure 2. Functional decomposition of the ADS architecture

1.3.1 Perceive

The perception stage begins with collecting information about the vehicle's surroundings with a suite of sensors, which may include camera, radar, ultrasonic, or light detection and ranging (LiDAR) sensors. The sensory data from each source is then fused together, which forges a more robust description of the environment and allows the ADS to localize itself with respect to its surroundings. Finally, the perception system must utilize semantic understanding to characterize the meaning of signs, roadway markings, or surrounding vehicles and vulnerable road users. Some perception systems combine these elements into a world model that visualizes and labels the external environment from the perspective of the ego vehicle (Behere & Torngren, 2015).

1.3.2 Plan

Next, the planning competency describes how the ADS makes purposeful decisions to optimally reach its destination, obey traffic ordinances, and maintain a minimal risk condition. The vehicle must first analyze its environment and kinematic state to generate a set of waypoints that determine its trajectory and plan its motion with a high level of computational completeness (always finding a solution) and efficiency (minimizing the time and effort to find a solution) (Behere & Torngren, 2015). The generated waypoints may also be projected onto the world model developed by the perception system. Once this is completed, the vehicle must then engage in behavior planning to ensure that it interacts with other road users in a predictable and safe manner while avoiding obstacles. Reactive control elements, which include "reflex" decisions during unexpected events, are also encompassed in this core competency. Lastly, diagnosis and fault management allow the ADS to continuously assess its capabilities and current state. If the ADS experiences an error that elevates the risk of its passengers, the vehicle can make decisions (e.g., transferring control to the human or temporarily disabling vehicle capabilities) that preserve a minimal risk condition (Behere & Torngren, 2015).

1.3.3 Maneuver

Lastly, the maneuver stage is primarily responsible for controlling the motion of the vehicle. The trajectory execution subsystem manipulates the throttle, brakes, and steering to manage the longitudinal and lateral motion of the vehicle. After this, the outputted vehicle kinematics are fed back to the planning stage of the ADS for trajectory planning. In addition to motion actuation, platform stabilization controllers aim to keep a vehicle in a stable condition by coordinating with ABS and ESC sensors. Motion control requests that violate these constraints may be rejected or scaled down to prevent dangerous situations like wheel lock-up or rear spin-out. Passive safety systems are also part of the control competency because they must be successfully actuated when a crash occurs (Behere & Torngren, 2015).

1.4 Isolation of the ADS Maneuver Subsystems

Previous studies have aimed to evaluate ADS performance across all three competencies (Thorn et al., 2018). However, there is value in evaluating the individual subsystems. By isolating each subsystem, the performance of each can be characterized independently, revealing ways the systems interact and compensate for possible limitations of the other subsystems.

Figure 3 provides an example block diagram for the maneuver subsystem with example inputs and outputs to each block in grey. In this example, the motion control functions first receive the trajectory plan—a list of positional coordinates with timestamps and/or velocities that the vehicle will be requested to follow—and calculates the difference between the desired path and actual trajectory. Using this information, the ADS motion controller generates a command that is sent to the vehicle actuators. Finally, the response of the actuators governs the vehicle's motion, and this information is fed back into the loop through sensors. Aside from the waypoints, external disturbances—such as road, vehicle, or environmental—are also inputted into the feedback loop because they may affect the vehicle's response. The performance of the total system can be measured by quantifying how much the vehicle and deviations from the target trajectory.

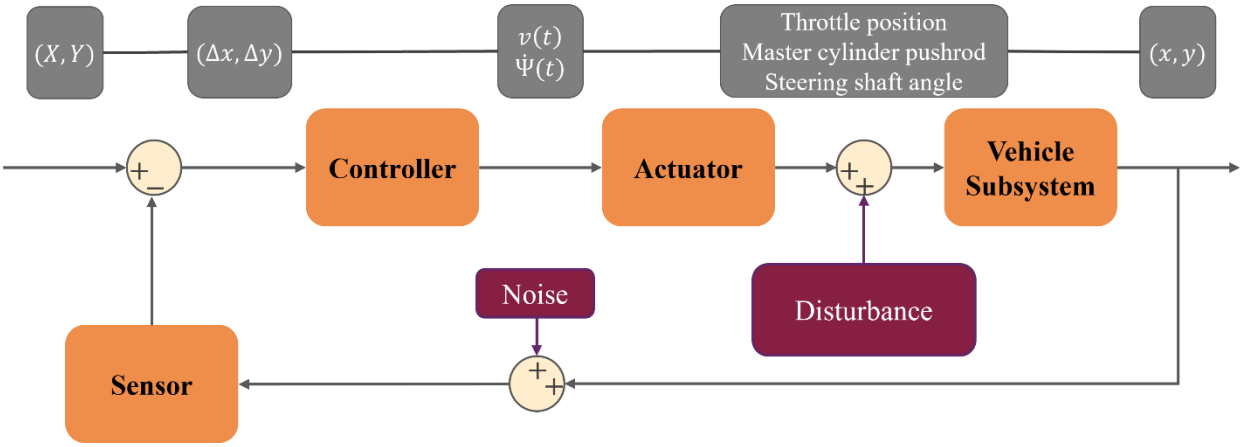

Figure 3. Control system diagram describing the ADS motion control subsystem

1.5 Current Efforts Regarding the Evaluation of ADS

Although one of the primary goals of large-scale deployment of ADS is to enhance road safety, concerns with entrusting an automated system with one's safety have remained prominent. To facilitate the large-scale adoption of ADSs, they must be stringently tested and evaluated prior to their deployment on public roadways due to their direct impact on the safety of other motorists and vulnerable road users. Currently, the automotive industry utilizes ISO 26262 as an international functional safety standard of electronic systems in the event of system failures. Notably, the standard outlines a risk-based framework for determining automotive safety integrity levels (ASILs) and provides validation requirements to ensure an acceptable level of safety is achieved (International Organization for Standardization, 2018). However, ISO

26262 cannot be applied to ADSs because the DDT shifts from a human driver to the machine. To address these gaps, ISO 21448 was published to complement ISO 26262 by addressing scenarios involving the safety of the intended functionality (SOTIF), a concept stating that an ADS must not only perform its intended function, but also do so safely, even in the absence of system faults (International Organization for Standardization, 2022). More specifically, ISO 21448 informs the design, operation, validation measures that must be fulfilled to achieve and maintain the SOTIF.

Despite these additional guidelines from ISO 21448, a standardized method of evaluating ADS performance remains an open question, leading researchers to propose their own methods of evaluating various aspects of ADS operation. For example, Rehrl and Gröchenig evaluated the localization accuracy of an ADS with respect to four different ground truth trajectories using a simulation-based approach. The authors first simulated an environment that mimicked real-world driving by incorporating lane markings, traffic signs, and obstacles before simulating the perception system of the ADS. The perception data was then used to calculate the position and orientation of the vehicle, and the authors evaluated the accuracy of the localization system with aggregate statistics such as the mean error, standard deviation, and root mean square error (Rehrl & Gröchenig, 2021). Pütz et al. analyzed real-world driving data to identify common scenarios to develop a comprehensive database of relevant traffic scenarios. The authors then demonstrated a validation framework that utilized this database of scenarios, along with other testing methods such as physical testing and software simulations, to comprehensively validate the performance of ADSs. The framework included methods for selecting and prioritizing scenarios based on their relevance and frequency in real-world driving, as well as metrics for evaluating ADS performance (Pütz et al., 2017). Zhang et al. objectively and subjectively evaluated ADS performance by first developing logical scenarios that were challenging enough to test performance while remaining representative enough to ensure applicability to real-world driving. From here, a driving simulator with participants was used to execute the scenarios and collect kinematic data on the performance of the ADS. Finally, the performance was evaluated with both subjective (human feedback on safety and comfort) and objective (deviation from the trajectory or speed profile) metrics (Zhang et al, 2022).

1.6 Problem Statement and Scope

Currently, there is an absence of regulations regarding the evaluation of ADS operation and performance. The main goal of this thesis is to address these gaps and contribute toward ADS evaluation efforts by (1) developing a method to characterize the motion control subsystem of an ADS and (2) demonstrating the characterization method by applying it to two exemplar control systems. Functions involving the perception and/or planning stages (e.g., object avoidance) were not within the scope of this experiment. Also, the purpose of the method was to characterize the vehicle behavior, not evaluate or score the performance of the vehicles. The developed method was designed to be objective, repeatable, and practicable, as defined below:

- Objective: utilize clear and measurable performance-driven metrics derived from analyzing kinematic data and system response
- Repeatable: produce consistent performance measures for a broad selection of ADS system architectures
- Practicable: maintain a high degree of effectiveness while remaining both cost-effective and time efficient

To achieve the project goals while remaining objective, repeatable, and practicable, four key project tasks were defined:

1. Define representative driving scenarios and road/vehicle disturbances to test system performance and robustness
2. Establish metrics that evaluate the system's path following ability
3. Develop analysis techniques to convey the metrics
4. Demonstrate the application of the proposed test methods via on-road testing

2 SCENARIO DEVELOPMENT

Characterizing the maneuver subsystem of an ADS first required defining representative test scenarios. First, a set of scenarios were defined to correspond to common driving maneuvers: straight-line, lane change, intersection, and traffic circle scenarios. A stop-and-go and slalom maneuver were also included to test the throttle and brake controls and investigate the effect of lateral sinusoidal motion on vehicle dynamics, respectively. These scenarios were specifically chosen to exercise the primary control elements of the DDT both in isolation and in combination to provide insight into the individual and combined performance of each motion control system and domain actuator. Table 4 lists the maneuvers and the respective control element(s) being tested, and Appendix B gives details on how the maneuvers were set up with cones and executed.

Table 4. Overview of the test scenarios and the respective control element(s) being tested

Group	Scenario	Maneuver	Lat.	Long.	Lat. + Long.
Straight Line	1.0	Accelerate, Constant speed, and Brake		X	
	1.1	Stop/slow and go (cyclic speed)		X	
Lane Change	2.0	Double lane change, brake to a stop			X
Intersection	3.0	Right/left turn, constant speed	X		
	3.1	Right/left turn, from rest			X
	3.2	Right/left turn, transient			X
Circle	4.0	Accel to constant speed			X
	4.1	Lane change, constant speed	X		
Slalom	5.0	Constant Speed left/right slalom	X		

Next, a set of kinematic parameters were established for each scenario, which included target speed, cornering radius, or acceleration (longitudinal and lateral). The magnitudes of these parameters were determined by conducting an extensive review of roadway design documents and naturalistic driving data to ensure that the test conditions are representative of typical driving environments and consistent with what vehicle occupants currently find acceptable (see Appendix A for more details). Multiple levels of each kinematic parameter were defined to exercise the system across multiple ODDs, such as low speed shuttle or highway driving, to demonstrate the applicability of the proposed method. The test scenarios were also designed to use minimal test track real estate and limit the use of unique features of a single test facility to make the method more practicable and repeatable. A unique combination of various kinematic parameters formed a design variation (DV), and tables listing each unique DV per scenario are given in Appendix B.

2.1 Straight-Line Maneuvers

The straight-line scenarios were defined as accelerating from rest, holding a target constant speed, and braking to rest (Scenario 1.0) and a longitudinal sinusoid (Scenario 1.1). Scenario 1.0 was created to test different levels of longitudinal acceleration and braking and to provide a basic baseline capability. Scenario 1.1 was included in the test matrix to consecutively test the throttle and brake controls and to simulate stop-and-go traffic conditions. Figure 4 and Figure 5 describe both Scenario 1.0 and 1.1, respectively.

Figure 4. Layout and execution of the start-to-stop maneuver

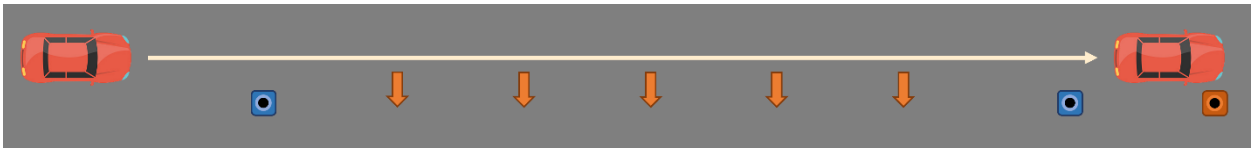

Figure 5. Layout and execution of the longitudinal sinusoid maneuver

2.1.1 Scenario 1.0

The target speeds of 6.7, 11.2, 17.9, and 24.6 m/s (15, 25, 40, and 55 mph) were selected in accordance with Virginia state laws, which outline general guidelines for statutory speed limits in four different ODDs: low-speed areas/school zones, urban/business areas, suburban areas/arterial roads, and country roads/interstate highways (VA Code). Academic literature, naturalistic driving data, and roadway design documents from the Institute of Transportation Engineers (ITE) and American Association of State Highway and Transportation Officials (AASHTO) were used to ensure that the longitudinal acceleration magnitudes were representative of road user behavior and current vehicle requirements, roadway requirements, or best practices. Similarly, emergency braking values were determined based on test requirements from FMVSS 135 and crash/near-crash naturalistic data (see Appendix A). Using these sources, two acceleration magnitudes—a typical value of 1.5 m/s^2 and a harsher value of 2.5 m/s^2—and three braking magnitudes—a light braking value of 2.0 m/s^2, a harsher braking of 3.9 m/s^2, and an emergency braking magnitude of 5.9 m/s^2—were implemented. A list of the velocity and acceleration parameters is given in Table 5.

Table 5. Selected maneuver parameters and their respective ODD for Scenario 1.0

Quantity	Value	Description or ODD
v_{target}	6.7 m/s (15 mph) 11.2 m/s (25 mph) 17.9 m/s (40 mph) 24.6 m/s (55 mph)	• School zones • Urban/business areas • Suburban areas, arterial roads • Country roads, interstate highways
a_x^+	1.5 m/s^2 (0.15 g) 2.5 m/s^2 (0.25 g)	• Typical • Harsh
a_x^-	-2.0 m/s^2 (-0.20 g) -3.9 m/s^2 (-0.40 g) -5.9 m/s^2 (-0.60 g)	• Typical • Harsh • Emergency

2.1.2 Scenario 1.1

For the longitudinal sinusoid, a target speed of 11.2 m/s (25 mph) was selected to fit more sinusoidal periods along the test track while remaining representative of traffic jam speeds. Two lowered target speeds, 0 and 6.7 m/s (15 mph), were chosen to recreate traffic conditions requiring either a complete stop or a noticeable reduction in speed. An acceleration magnitude of 2.0 m/s^2 (0.2 g) was implemented based on the average from Scenario 1.0. All three braking magnitudes from Scenario 1.0 were utilized for the 11.2 m/s to 0 m/s sinusoid, but the 11.2 m/s to 6.7 m/s sinusoid excluded the 5.9 m/s^2 braking magnitude because it could not be adequately executed during the testing phase. This was because typical motorists decelerate with an average jerk of 10.7 m/s^2, and braking from 11.2 to 6.7 m/s with a 5.9 m/s^2 magnitude equates to only 0.76 seconds of braking (Kusano & Gabler, 2011). Because of this short time frame, the 5.9 m/s^2 braking condition could not be accurately reached and sustained. A list of the velocity and acceleration parameters is given in Table 6.

Table 6. Selected maneuver parameters and their respective ODD for Scenario 1.1

Quantity	Value	Description or ODD
v_{target}	11.4 m/s (25 mph)	• Major roadways with heavy traffic
v_{lower}	0 m/s (0 mph) 6.7 m/s (15 mph)	• Stop-and-go traffic • Decreased speeds due to traffic
a_x^+	1.98 m/s^2 (0.20 g)	• Average
a_x^-	-2.0 m/s^2 (-0.20 g) -3.9 m/s^2 (-0.40 g) -5.9 m/s^2 (-0.60 g)	• Safe • Harsh • Emergency

2.2 Lane Change Maneuver

Scenario 2.0 consisted of a double lane change maneuver followed by moderate braking to consecutively test the steering and brake controls and is shown in Figure 6.

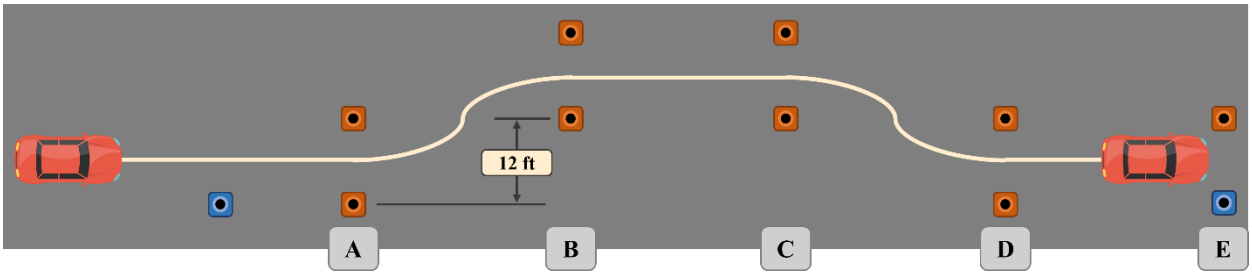

Figure 6. Layout and execution of the double lane change and braking maneuver

Target speed values of 11.2 m/s (25 mph) and 17.9 m/s (40 mph) were selected using a similar rationale as for Scenario 1.0, replicating suburban areas/arterial roads and country roads/interstate highways. The gate distances for each lane change were determined via simulation using CarMaker and limiting the lateral acceleration to approximately 2.9 m/s^2 (IPG Automotive, 2021). However, variations with higher lateral accelerations could be used for emergency avoidance testing. After the lane change was completed, a moderate braking magnitude of 3.9 m/s^2 brought the vehicle to rest. A list of the velocity and acceleration parameters is given in Table 7.

Table 7. Selected maneuver parameters and their respective ODD for Scenario 2.0

Quantity	Value	Description or ODD
v_{target}	11.2 m/s (25 mph) 17.9 m/s (40 mph)	• Urban/business areas • Suburban areas, arterial roads
$a_{y,\max}$	2.9 m/s^2 (0.30 g)	• Harsh
a_x^-	-3.9 m/s^2 (-0.40 g)	• Harsh

2.3 Intersection Maneuvers

The intersection maneuvers were outlined as three separate tests: constant speed turns (Scenario 3.0), turning from rest (Scenario 3.1), and braking into a turn (Scenario 3.2). These tests were implemented to assess the vehicle's response to a step steer input under both steady-state and transient longitudinal acceleration conditions. Figure 7, Figure 8, and Figure 9 provide a diagram of the intersection maneuvers.

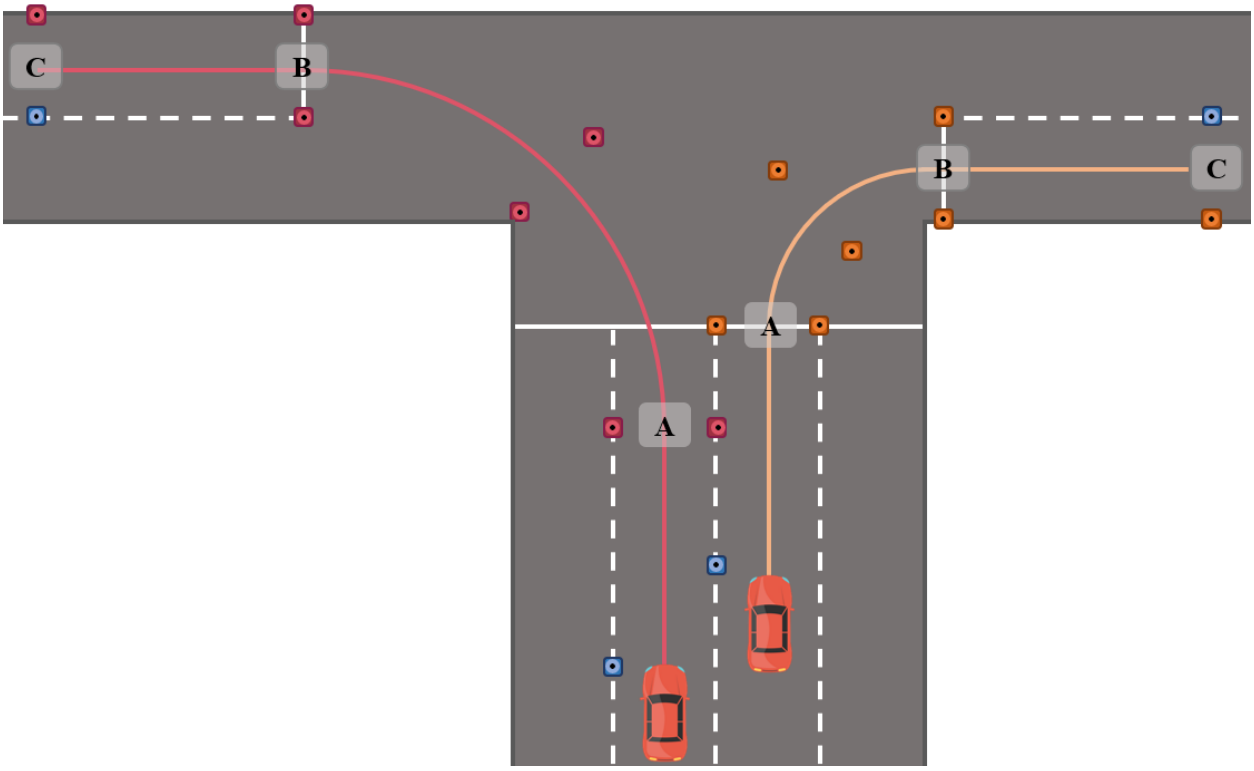

Figure 7. Layout and execution of the constant speed intersection turn maneuver

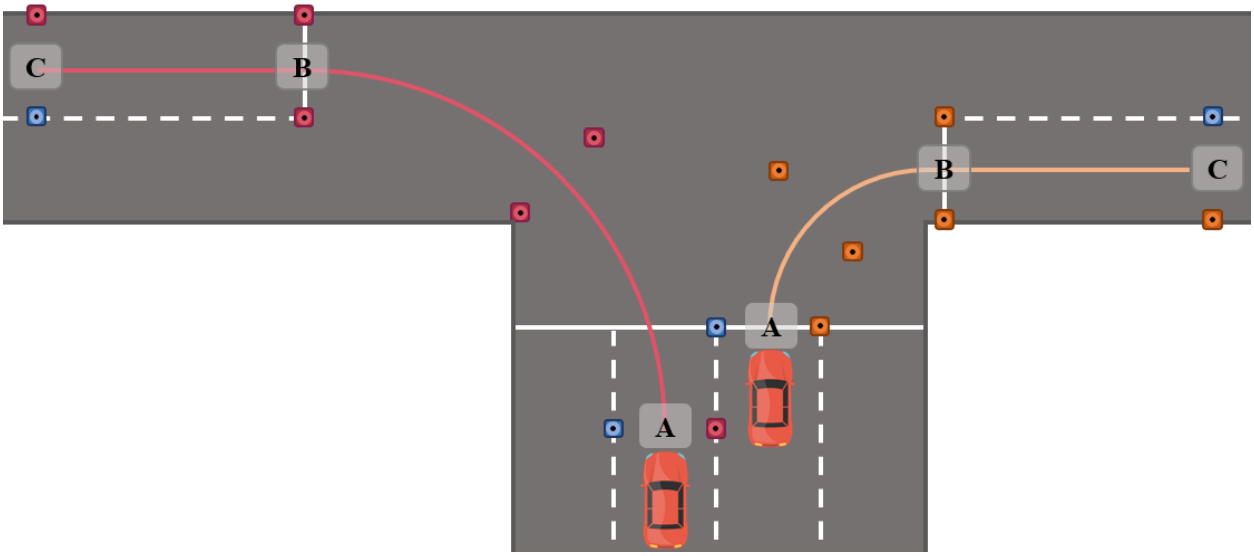

Figure 8. Layout and execution of the intersection turn from rest maneuver

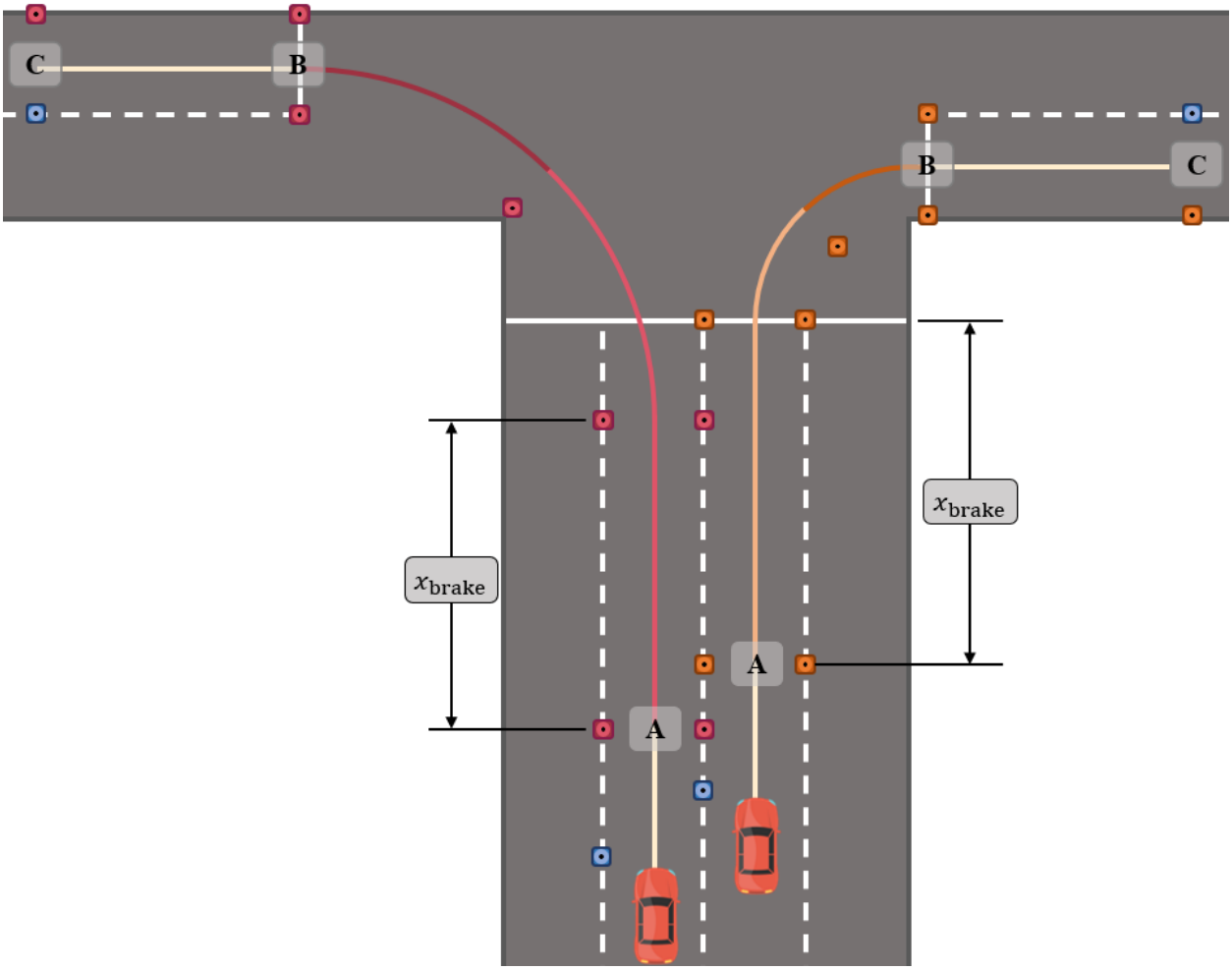

Figure 9. Layout and execution of the transient intersection turn maneuver

For all three scenarios, turning radii of 6.7 m and 18.3 m were selected for right and left turns, respectively. Section 5.3.5 of the AASHTO Green Book suggests that the effective radius of right turns should be at least 6.7 m (AASHTO, 2018). In a study that assessed the kinematics of left-turning vehicles in an intersection with three lanes in each direction, the authors determined that the distribution of actual traveled radius of the vehicles was skewed right with a median radius of 19.8 m (Happer et al., 2009). A similar value of 18.3 m was selected due to test track constraints.

Regarding the lateral acceleration limits, lower limits of 1.5 m/s^2 and 2.9 m/s^2 were allowed for vehicles accelerating into a turn from rest because lateral acceleration is proportional to a vehicle's longitudinal speed squared. Conversely, higher lateral acceleration limits of 2.9 m/s^2 or 4.4 m/s^2 were used for turning maneuvers that did not begin from rest. These values were

selected based on the lateral accelerations seen in Table A–3 of Appendix A, which contain the results of naturalistic driving studies in intersection environments and AASHTO recommendations. Longitudinal accelerations and braking magnitudes of up to 1.5 m/s^2 and 2.0 m/s^2, respectively, were allowed according to the results of the naturalistic driving studies in Table A–4 of Appendix A. The turning speeds were calculated according to the equation below, adopted from AASHTO:

$$v = \sqrt{15R(0.01e_{\max} + f_{\max})},$$

where v (mph) is the vehicle's longitudinal speed, R (ft) is the turn radius, $f_{\max}$ (g) is the maximum friction factor—which is equivalent to the maximum lateral acceleration—and $e_{\max}$ (%) is the superelevation of the turn. For Scenario 3.2, approach speeds of 11.2 m/s (25 mph) and 17.9 m/s (40 mph) were selected because they are representative of intersections with traffic lights in city and suburban environments.

2.3.1 Scenario 3.0

In Scenario 3.0, a typical and harsh constant speed cornering maneuver were created with lateral acceleration limits of 2.9 m/s^2 and 4.4 m/s^2, respectively. The lateral acceleration limits and turn radii are listed in Table 8.

Table 8. Selected maneuver parameters and their respective ODD for Scenario 3.0

Quantity	Value	Description or ODD
r	7.6 m (25 ft) 18.3 m (60 ft)	• Right turn radius (small city block) • Left turn radius (large intersection)
$a_{y,\max}$	2.9 m/s^2 (0.30 g) 4.4 m/s^2 (0.45 g)	• Typical • Harsh

2.3.2 Scenario 3.1

In Scenario 3.1, lower lateral acceleration limits of 1.5 m/s^2 and 2.9 m/s^2 were allowed for vehicles accelerating into a turn from rest because lateral acceleration is proportional to a vehicle's longitudinal speed squared. The lateral acceleration limits and turn radii are listed in Table 9.

Table 9. Selected maneuver parameters and their respective ODD for Scenario 3.1

Quantity	Value	Description or ODD
r	7.6 m (25 ft) 18.3 m (60 ft)	• Right turn radius (small city block) • Left turn radius (large intersection)
$a_{y,\max}$	1.5 m/s2 (0.15 g) 2.9 m/s2 (0.30 g)	• Typical • Harsh

2.3.3 Scenario 3.2

In Scenario 3.2, a typical lateral acceleration value of 2.9 m/s^2 was selected. Longitudinal accelerations and braking magnitudes of up to 1.5 m/s^2 and 2.0 m/s^2, respectively, were allowed. Approach speeds of 11.2 m/s and 17.9 m/s were selected because they are representative of intersections with traffic lights in city and suburban environments, as mentioned above. The lateral acceleration limits, turn radii, and approach speeds are listed in Table 10.

Table 10. Selected maneuver parameters and their respective ODD for Scenario 3.2

Quantity	Value	Description or ODD
$v_{approach}$	7.6 m (25 ft) 18.3 m (60 ft)	• City • Suburban
r	2.9 m/s^2 (0.30 g) 4.4 m/s^2 (0.45 g)	• Right turn radius (small city block) • Left turn radius (small city block)
$a_{y,\max}$	2.9 m/s^2 (0.30 g)	• Typical
a_x^-	-2.0 m/s^2 (-0.20 g)	• Typical

2.4 Traffic Circle Maneuvers

The traffic circle maneuvers were grouped into two separate tests: accelerating from rest followed by holding a constant speed (Scenario 4.0) and a constant speed single lane change (Scenario 4.1). Both tests were included to investigate the control system's response to a constant, non-zero yaw input under both steady-state and transient longitudinal acceleration conditions as shown in Figure 10.

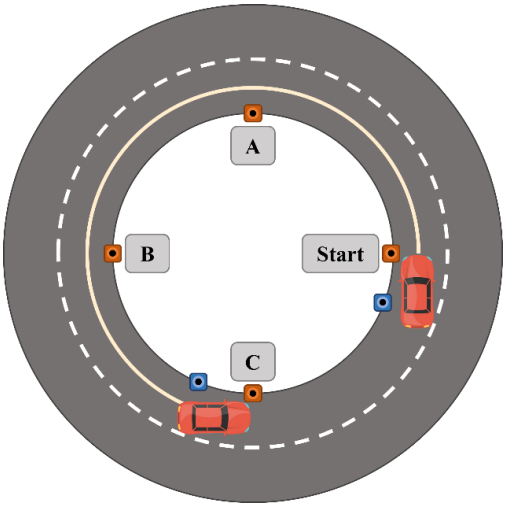

Figure 10. Layout and execution of the acceleration and constant speed traffic circle maneuver

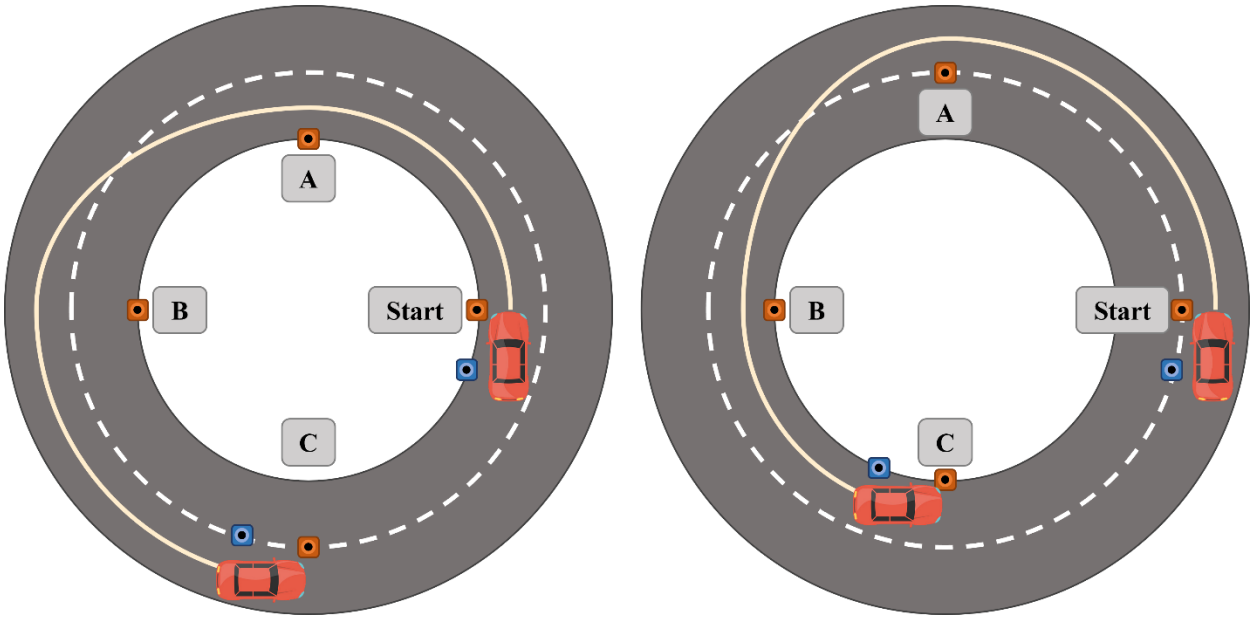

Figure 11. Layout and execution of the constant speed traffic circle lane change maneuver

The traffic circle radii of 15.2 m (50 feet) and 30.4 m (100 feet) were selected for both maneuvers. Due to sizing constraints at the test facilities, only the 15.2 m radius was tested. Like the intersection maneuvers, AASHTO recommendations and results from naturalistic driving studies were used to determine the lateral acceleration limit of 2.9 m/s^2 and longitudinal acceleration limit of 2.0 m/s^2. In Scenario 4.1, the lane change maneuver utilized a standard lane width of 3.65 m (12 feet). The maneuver parameters for both tests are listed in Table 11.

Table 11. Selected maneuver parameters and their respective ODD for Scenario 4.0 and 4.1

Quantity	Value	Description or ODD
r	15.2 m (50 ft)	• Traffic circles
$a_{y,\max}$	2.9 m/s^2 (0.30 g)	• Typical

2.5 Slalom Maneuver

A slalom maneuver was included in the study to test the limits of the vehicle's lateral controller under transient conditions and assess the response of the vehicle dynamics. The slalom maneuver is described in Figure 12.

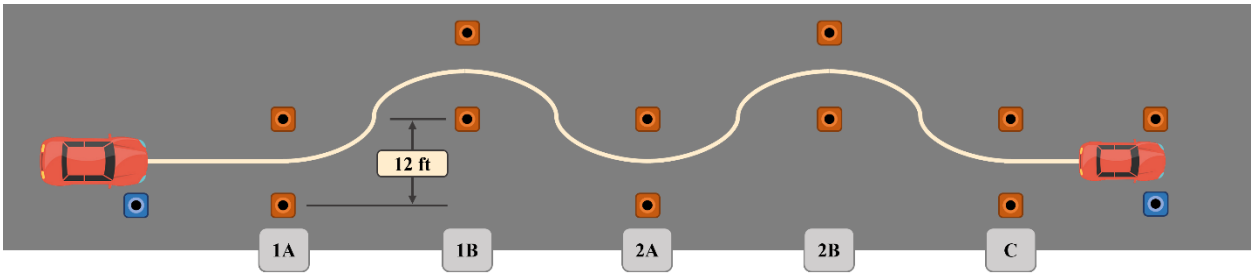

Figure 12. Layout and execution of the constant speed lateral sinusoid maneuver

This maneuver is equivalent to a repeated double lane change test without the dwell portion, so the target speed values of 11.2 m/s and 17.9 m/s and lateral acceleration limit of 2.9 m/s^2 were selected in accordance with Scenario 2.0. Similarly, the gate distances for each lane change were also determined via simulation using CarMaker. The maneuver parameters describing the slalom test are listed in Table 12.

Table 12. Selected maneuver parameters and their respective ODD for Scenario 5.0

Quantity	Value	Description or ODD
v_{target}	11.2 m/s (25 mph) 17.9 m/s (40 mph)	• Urban/business areas • Suburban areas, arterial roads
$a_{y,\max}$	2.9 m/s^2 (0.30 g)	• Harsh

2.6 Disturbances

To assess the response of an ADS to outside disturbances during maneuver operation, various alterations to both the vehicle setup and roadway were introduced. These include reduction in tire pressure below federal requirements, variation in roadway, and presence of

roadway bumps. The following sections explore the chosen disturbances and give justification to the selected disturbance levels.

2.6.1 Tire Pressure

Tire pressure reduction was selected as a vehicle disturbance because it could be easily modified and reversed, making it a practicable and repeatable disturbance to implement. The left-side tire pressures were lowered to 20 psi from the manufacturer recommend inflation, triggering the required tire pressure monitoring system (TPMS) warning per FMVSS 138 (49 CFR § 571.138, 2005). After testing the ADS with reduced left-side tire pressure, the left-side tires were inflated, and the process was repeated with the right-side tires. Pressures were lowered on both tires per side to induce steering to the left or right, respectively, and this disturbance was tested across multiple test scenarios to capture both longitudinal and lateral affects.

2.6.2 Roadway Grade

Road grade was selected because it induced a longitudinal force due to gravity that accelerates or decelerates the vehicle. In this experiment, the test vehicles were operated on the Highway section of the Virginia Tech Transportation Institute (VTTI) Smart Road, which provided a grade of ±8%. This magnitude is consistent with AASHTO (2018), which recommends maximum road grades between 5% to 15% depending on design speed and road type. The straight-line and slalom scenarios were selected to assess the vehicle's longitudinal and lateral response to the disturbance.

2.6.3 Roadway Bumps

Road bumps were chosen because they perturbed the control system by providing an impulse-like input into the vehicle system and were easy to implement. In this experiment, bumps were created by stacking two PSS RoadQuake temporary rumble strips, creating a 38-mm (1.5 in) bump that stretched across the entire lane. This disturbance was implemented to the intersection and traffic circle scenarios to understand how the system responds while under lateral loading. For the intersection scenarios, the bump was placed in two locations: (1) the middle of the turn, where the ADS experiences the largest lateral acceleration, and (2) the end of the turn, where there was a transition from cornering to straight-line behavior. For the traffic circle scenarios, two consecutive bumps were placed immediately after the acceleration phase to study if coupling from the first to second bump existed.

3 DATA COLLECTION AND PROCESSING

Once representative test scenarios were defined, a method implementation and data collection framework were established (Figure 13). For each maneuver, a reference path was defined in the form of a waypoint list containing information on the vehicle position and velocity. The waypoints of each scenario were generated from either a skilled driver or a synthetic path, and the same reference path files were used for both test vehicles to keep the inputted waypoints constant. Once this was done, the reference paths were fed into the motion control system as a trajectory. Both vehicles were also equipped with data acquisition systems (DAS), a differential GPS (DGPS), and an inertial measurement unit (IMU) to collect basic kinematic data and ADS information without accessing the internal control system architecture. Finally, the ADS response to the test scenario was recorded, and the performance of the vehicles was evaluated based on metrics defined in Section 3.5.

Table 13 provides the channels needed for the DAS within the test vehicles. A limitation that should be noted was the fact that no analog filter was implemented prior to sampling the GPS and IMU data, so it was possible that the sampling frequency was not high enough to satisfy the Nyquist-Shannon theorem. In addition, a lowpass filter was used prior to down sampling the IMU data to match the sampling rate of the GPS data, so the full dataset is a mixture of data sampled without anti-alias filtering and data sampled without anti-aliasing filtering but filtered before down sampling. *This data collection error has served as a lesson to myself, and in future endeavors I will ensure that best practices are adhered (especially when data collection takes three months to complete).*

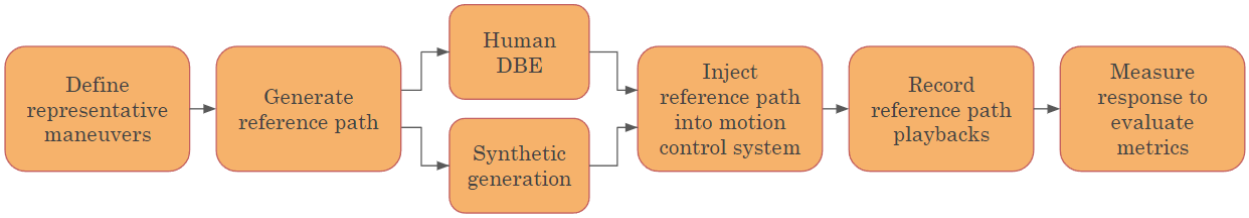

Figure 13. Data collection and test execution framework

Table 13. DAS channels required for analysis

Variable	Source
System time	DAS
Latitude from DGPS	DGPS
Longitude from DGPS	DGPS
Vehicle velocity along path	DGPS/IMU
Heading Direction	DGPS/IMU
Lateral Acceleration	IMU
Longitudinal Acceleration	IMU
Yaw rate	IMU
Flag for if ADS active	Vehicle/DAS
Test trigger for human DBEs	DAS

3.1 Test Vehicles

Two test vehicles instrumented with ADS capability (Table 14) were utilized for this study and will be referred to as "Vehicle A" and "Vehicle B." Some information about each control system was known prior to experimentation and is outlined below. Regarding Vehicle A, the longitudinal controller was governed by a proportional-integral-derivative (PID) controller that was tuned in-house to minimize rise time and steady-state error, and the lateral controller utilized a geometric path-tracking algorithm that computed the required angular velocity command to move the vehicle from its current position some look-ahead point (Coulter, 1992). For Vehicle B, the longitudinal controller was designed for adaptive cruise control (ACC), so its acceleration and braking abilities were limited to approximately 1.5 m/s^2. The lateral controller of Vehicle B was tuned for occupant comfort. Despite prior knowledge of each control system, the results of the characterization method also demonstrated the known limitations, indicating that the method is also applicable to black-box ADSs. It should be noted that this project evaluated two exemplar controllers, not necessarily production-intent control architectures, because the primary focus of this thesis is to demonstrate characterization methods. Because of this, the results in the following chapter are not representative of a production ADS's control precision.

Table 14. Specifications of the control system architectures for each test vehicle

Vehicle Function	Vehicle Make and Model	
	2015 Infiniti Q50 (VTTI)	2018 Volkswagen Passat (CNXMotion)
Steering	Infiniti electronic power steering with control access via MicroAutoBox	Nexteer Automotive prototype dual pinion electric power steering actuated via CAN
Powertrain	Infiniti throttle by wire via CAN message request	Continental instrumented engine controller with prototype software to accept control messages via CAN
Brakes	In-house VTTI linear actuated brake pedal control	Continental foundation brakes with Mk100 instrumented ECU with prototype software to accept control messages via CAN
Control System	In-house VTTI ROS based software running on VTTI's FlexDAS system	In-house prototype control software with path management on separate controller
Sensing	DGPS via Novatel with differential corrections and IMU via Vectornav VN300	OSTx RT4003 IMU/GPS w/ differential corrections
DAS	FlexDAS	VN6030

3.2 Reference Path Generation

The reference path injected into the control system represented the ground truth against which the subsequent playback was measured. As mentioned above, one reference path generation method required driver's best effort (DBE) where a skilled driver executed a maneuver while the DGPS recorded the waypoint trail. With this method, the maneuver path was defined with cones based on the kinematic parameters of each scenario to aid with the repeatability (see Appendix B for details on driver instructions and cone setup). Kinematic tolerances of ±0.5 m/s^2 and ±0.5 m/s were allowed for the mean acceleration and speeds, respectively, to ensure that the DBE closely reflected the defined maneuver without enforcing unrealistic expectations on the driver.

Although collecting reference paths with a skilled driver was successful, the cone setup and capture of the DBEs proved to be the longest portion of testing, so reference paths were also generated synthetically. For the straight-line, intersection, and traffic circle scenarios, the reference path was mathematically derived by defining an initial heading vector and the

beginning and end points, and the synthetic paths were verified by plotting their coordinates in a mapping software. As an example, Figure 14 shows a comparison of a DBE and synthetic reference path for a straight-line acceleration and braking scenario, and Figure 15 maps the synthetic paths plotted using MATLAB's geoplayer function. On the other hand, the double lane change with a stop and the slalom maneuver utilized CarMaker to create the reference paths while constraining the lateral acceleration to 2.9 m/s^2.

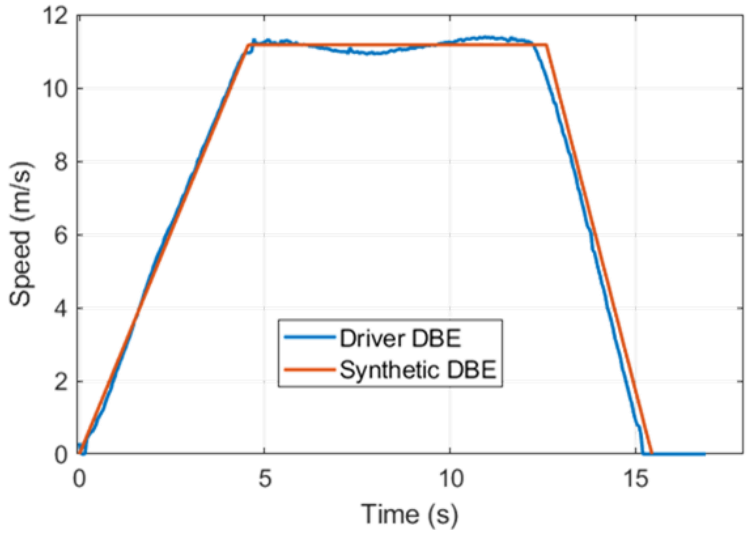

Figure 14. Validation of the synthetic reference paths via comparison with the DBE reference path for Scenario 1.0

Figure 15. Example of using the geoplayer function to map and localize the synthetic reference path for Scenario 1.0

3.2.1 Advantages of Synthetic Reference Paths

Three aspects of the synthetically derived reference paths significantly improved the reproducibility of the project method: setup time, modification, and translation. As mentioned before, the most time-consuming portion of the human driver conducting the DBE was setting up the cones and remaining within the kinematic constraints, so the synthetic reference paths removed this issue. On top of quicker reference path generation, these paths could also be modified synthetically by tuning the waypoint files. For example, the lateral acceleration of constant speed cornering maneuvers (e.g., constant speed intersection and slalom scenarios) was adjusted by modifying the speed profile of the waypoints while maintaining the same positional coordinates. This was useful when exploring lateral acceleration values between the planned DVs to understand when the control system's performance begins to decline. In addition to modification, the synthetic paths could be translated to different portions of the test track. This translation was useful for studying the effect of roadway grades. The synthetic paths from the level Surface Street section of VTTI were translated to the graded Highway section of the VTTI Smart Road, ensuring that the disturbance was compared directly to the original test inputs (Figure 16). A quantitative comparison between the human DBE and synthetic reference paths is given in Section 4.7 of the Results and Discussion.

Figure 16. Example of translating the synthetic reference path from VTTI Surface Street to the Highway section

3.3 Test Execution

After feeding the reference trajectory to the ADS, the vehicle attempted each unique DV eight times while under ADS control. During the trajectory playback phase, both vehicles utilized a triggering mechanism to flag the active test regions during the post-processing phase. For the DBE reference path, an optical sensor system was utilized. First, a reflective beacon was placed at both the beginning and the end of the maneuver path. The test active flag was triggered when the optical sensor detected the first reflective cone until passing the second reflective cone; a five-second buffer window was also included at the end of each maneuver to capture any stop error and to prevent data clipping. For the synthetic trajectories, the test active flags were built into the reference path files, and this trigger location was applied to the subsequent playback tests in the post-processing by using a k-nearest neighbor search algorithm of the trigger's position data. On top of the gates that mark the beginning and end of a test maneuver, the automation state of the vehicle was also recorded to indicate when the vehicle is in ADS active mode.

3.4 Processing and Visualization Pipeline

After the kinematic response data was collected with the DAS for each test vehicle, a post-processing framework was developed in MATLAB to filter the data and calculate several derived variables and system metrics. Each step within the post-processing framework is outlined in Figure 17 and described in the following paragraphs.

1	Data importing, filtering, and interpolation	Read data as .csv or ROS and align DAS channels to GPS
2	Select test active portions	Remove test portions where the test collection flag was marked as FALSE
3	Kinematic data preparation	Calculate derived quantities from the raw GPS and IMU data
4		Calculate difference in the vehicle's response relative to the reference path
5	Select automation portions	Remove test portions where the ADS was not active
6	Ensemble averaging	Create an ensemble average of the response data with respect to path completion

Figure 17. Data processing framework

First, a MATLAB script was created to extract the vehicle data from the test files, and the reference paths were converted to the required variables outlined in Table 13 because the GPS

and IMU sampling rates differed from each other, the IMU data ($f_s = 50$ Hz) was interpolated onto the GPS data ($f_s = 20$ Hz). A post-processing filter (8^{th}-order Butterworth lowpass filter with a cutoff frequency of 8 Hz) was used on the IMU data to prepare the data for interpolation and mitigate potential aliasing. However, it should be noted that in practice, an anti-aliasing filter should be implemented upstream of the data sampling stage to ensure that Nyquist-Shannon is obeyed.

The next step involved removing all data that were not marked with the test active flag, aligning all tests at the starting position of the maneuver. As mentioned in the previous section, the test active flags were implemented with optical gate sensor for DBE reference paths or built into the synthetic reference paths. A second filter removed any data where the vehicle's ADS was not activated, ensuring that the collected data solely reflect the response of the control system during automation mode.

After the initial filtering, the derived variables from the raw data were calculated. Next, the difference between the reference path and the test trials was then calculated for several kinematic parameters. These variables are denoted with $\Delta\Theta$, where Θ represents some kinematic parameter; more details about the calculations of the derived variables are given in Appendix C.

Finally, an ensemble average of the eight trials was calculated for all the DVs. First, each playback trial was aligned on the test's normalized path completion (distance along the path divided by the total path distance), and the mean and standard deviation of all trials was calculated at each point along the path. Figure 18 shows the per test and then ensemble average of the lateral offset (ΔY) data, where the shaded regions represent ±2 standard deviations (σ) of the test trial data and provide insight into the precision of the ADS motion control. When comparing ensemble average traces, significance between groups was denoted by a lack over overlapping between two traces and their respective $\pm 2\sigma$ bounds.

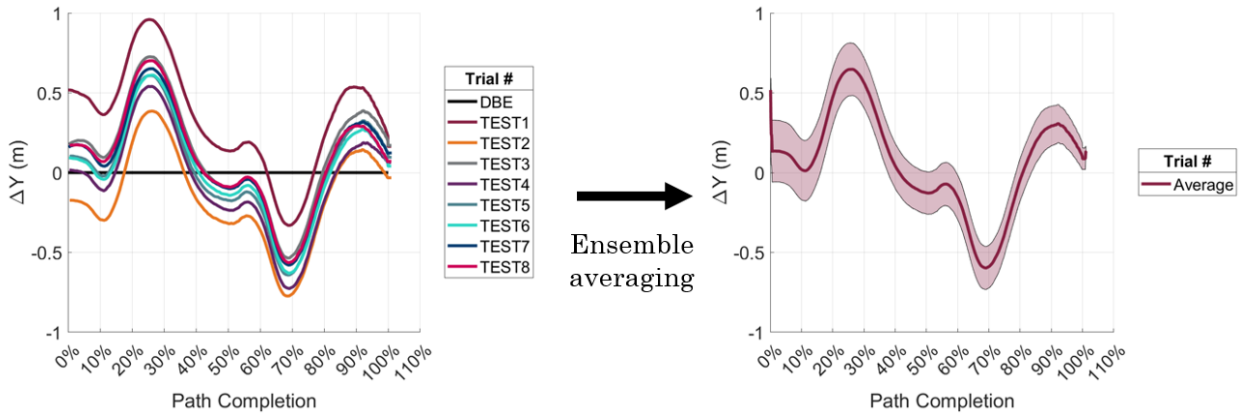

Figure 18. Example of the ensemble average plots. The shaded regions represent ±2SD

3.5 Performance Metrics

A set of performance metrics were defined to quantify how closely the vehicle followed the reference path. These metrics were derived from kinematic parameters (position, speed, accelerations) that were capable of being collected by a data source independent of vehicle sensors or the ADS. This provides an independent measurement device and eliminates the potential challenge of accessing data from the vehicle. All metrics and data were calculated with respect to the *z*-down SAE J670 convention shown in Figure 19 (SAE International, 2022). The metrics were sorted into two types, primary and secondary. The methods used to calculate these metrics can be found in Appendix C.

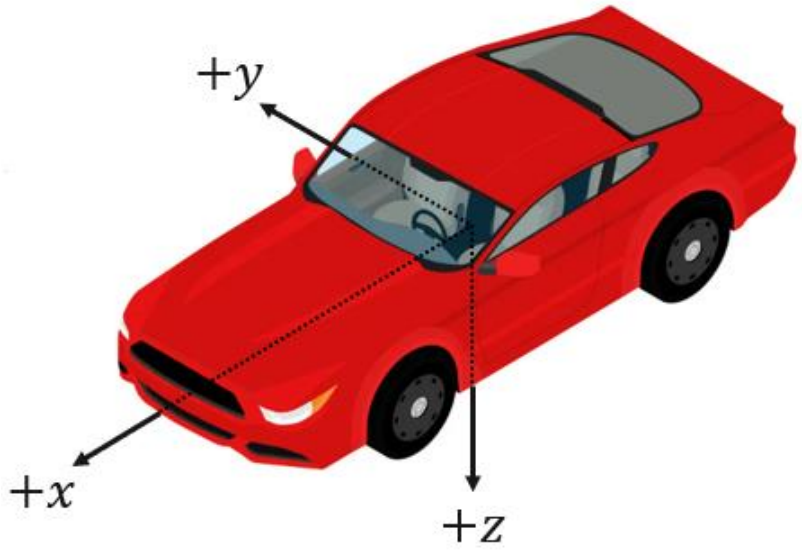

Figure 19. SAE J670 *z*-down convention

3.5.1 Primary Metrics

The primary metrics were defined as the parameters that most directly affect the operation of the vehicle. All metrics are listed in Table 15 and include a graphical description in Figure 20. The lateral offset and heading error, ΔY and $\Delta \Psi$, indicated how well the vehicle followed the reference path, which relates to how well the ADS remained within its travelled lane. The speed error, Δv, indicated how well the vehicle followed the requested speed profile and is connected to other safety metrics such as following distance and time to collision (TTC). For maneuvers with a stop event, the stop error, Δx_{stop}, quantified the longitudinal distance overshoot from the designated stopping point and directly related to collisions with lead vehicles or pedestrians. Finally, test completion percentage, $\text{TC}_{\%}$, tracked if a vehicle was unable to complete a maneuver safely and how far the vehicle was along the path before requiring the fallback user (the human) to immediately take control.

Table 15. List of primary metrics for evaluating the control systems

Variable	Name	Description
ΔY	Lateral offset	Lateral displacement from reference path
$\Delta \Psi$	Heading error	Heading difference from reference path
Δv	Speed error	Speed difference from reference profile
Δx_{stop}	Stop error	Longitudinal distance error at stop point
$\text{TC}_{\%}$	Test completion percent	Test completion before the user had to take control

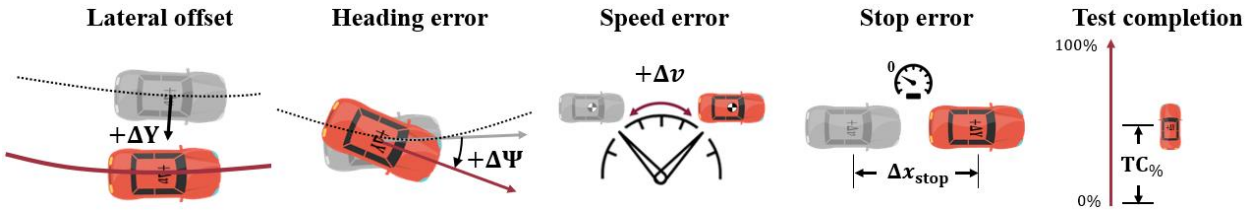

Figure 20. Diagrams describing each primary test metric

3.5.2 Secondary Metrics

In addition to the primary metrics, a set of secondary metrics were defined to give insight into how or why the ADS control system may be functioning as observed (Table 16). The local time lag metric measured the response of the brake and throttle controls from a more standard controls paradigm (e.g., lag, rise time), and the local distance lag described the corresponding distance overshoot/undershoot due to the time lag. The adjusted lateral offset variable provided a

measure of the path deviation after removing localization errors. The rest of the metrics encompassed kinematic behaviors such as accelerations errors and yaw rate.

Table 16. List of secondary metrics for evaluating the control systems

Variable	Name	Description
t_T	Local time lag	Distance or time lag of the ADS relative to the reference speed profile during longitudinal acceleration events
t_X	Local distance lag	
ΔY_{offset}	Adjusted lateral offset	Adjusted ΔY for bias reduction
Δa_y	Lateral acceleration error	Lateral acceleration difference from reference path
Δa_x	Longitudinal acceleration error	Longitudinal acceleration difference from reference path
$\dot{\psi}$	Yaw rate	Yaw rate change from reference path

4 RESULTS AND DISCUSSION

The analysis of the kinematic metrics for each test scenario demonstrated that the method could effectively evaluate the performance of each ADS in various scenarios. A total of 102 unique DVs encompassing all scenarios, kinematic parameters, and disturbances were tested for Vehicle A. Vehicle B was tested across the same test suite with some tests removed due to the longitudinal requests exceeding the system's design constraints, leaving 62 unique DVs. Each unique DV was attempted by the ADS eight times, totaling 1,664 trials across all DVs. The method determined that Vehicle A's control system consistently lagged in longitudinal actuation and turned early and with a larger cornering radius. The control system of Vehicle A also could not exceed a lateral acceleration of 3.5 m/s^2 when under ADS control, which caused the vehicle to turn wide for radius and speed combinations with a lateral acceleration greater than 3.5 m/s^2. On the other hand, Vehicle B's control system consistently exhibited a small delay before turning and tended to overshoot lane changes at higher lateral accelerations. Regarding disturbances, only the road grade significantly affected the response of both vehicles.

4.1 Straight Line Maneuvers

4.1.1 Scenario 1.0

The constant speed portion of the straight-line acceleration, constant speed, and braking maneuver (Scenario 1.0) provided a baseline characterization of each vehicle's longitudinal performance with respect to the primary metrics and are summarized in Table 15. The results indicated that Vehicle A showed a right-side lateral bias of 0.2 meters on average. Vehicle A also had minimal heading or speed offsets, but the heading did have a standard deviation of 0.7 degrees. On the other hand, Vehicle B had a significantly smaller lateral offset to the right and minimal heading error with low standard deviation, but the vehicle tended to lag in speed by 0.2 m/s on average. It should be noted that for the remainder of the straight-line maneuver analysis, only Vehicle A was explored because many of the braking and acceleration requests fell outside the ODD of Vehicle B.

Table 17. Average of ΔY_{avg}, $\Delta \Psi_{avg}$, and Δv_{avg} ±2SD during the constant speed portion across all DVs (S1.0, non-disturbance, both vehicles)

Test Vehicle	ΔY_{avg} (m)	$\Delta \Psi_{avg}$ (deg)	Δv_{avg} (m/s)
A	0.22 ± 0.20	0.0 ± 0.7	0.0 ± 0.1
B	0.06 ± 0.02	0.0 ± 0.1	-0.2 ± 0.3

Stratifying the analysis across the acceleration, constant speed, and braking conditions exhibited clear tendencies of the longitudinal control system. According to Figure 21, the speed of the ADS ($\pm 2\sigma$) was below reference speed request by approximately 1 m/s on average during the acceleration portion. Subsequently, the speed of the ADS was above the reference speed request by approximately 1 m/s on average during braking. It should be noted that the 24.6 m/s DV did include a downhill grade influence (-3%) because the VTTI test facility did not have a level strip of roadway long enough to accommodate the entire maneuver, which is likely the source of the increased Δv.

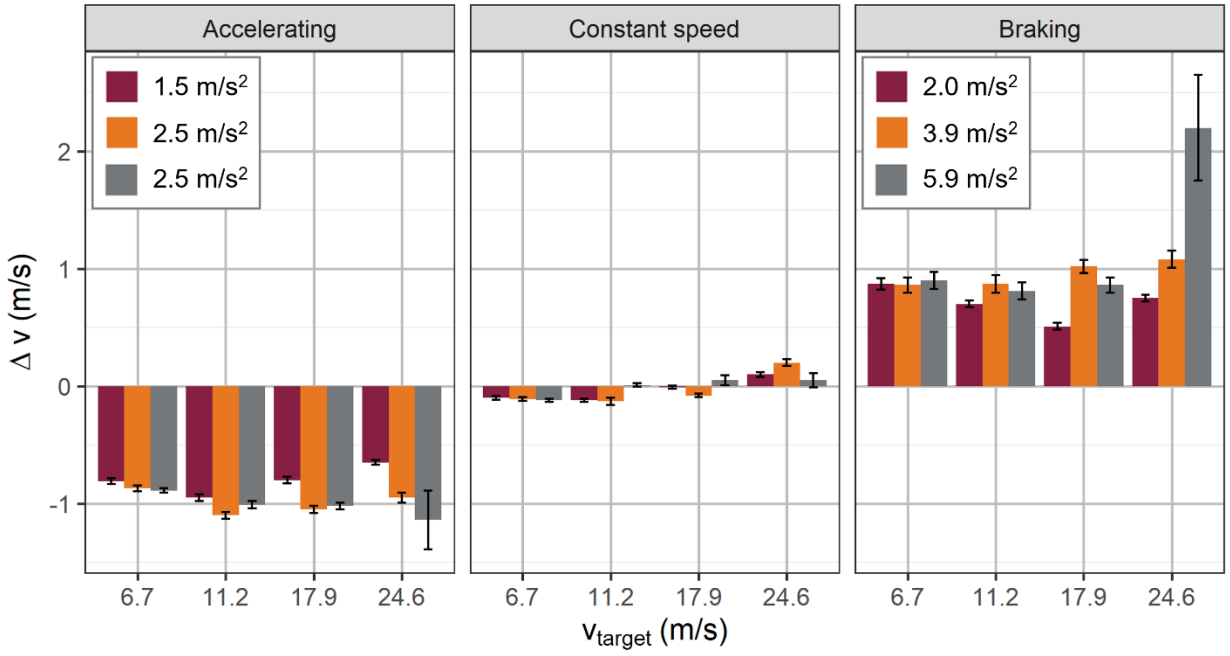

Figure 21. Average Δv for each start-to-stop DV segmented across the acceleration, constant speed, and braking phases (S1.0, non-disturbance, Vehicle A)

The ensemble averaged results of a single DV (v = 17.9 m/s, a_x^+ = 0.25 m/s^2, and a_x^- = 0.39 m/s^2; n = 8 trials) were also analyzed in Figure 22 to gain further insight into the vehicle's control system. The ensembled Δv vs. path completion plot revealed that the vehicle was not

able to meet the desired speed profile for the entire acceleration phase and had to use the beginning of the constant speed phase of the reference path to catch up to the target speed. Additionally, the response of the ADS accumulated speed error during the braking phase and was still travelling 2.5 m/s at the end of the test, posing a safety risk to pedestrians and lead vehicles. From an experimental design standpoint, these traces contained a narrow standard deviation along the trajectory, demonstrating the precision of the ADS response and the repeatability of the method even during transient phases of the maneuver.

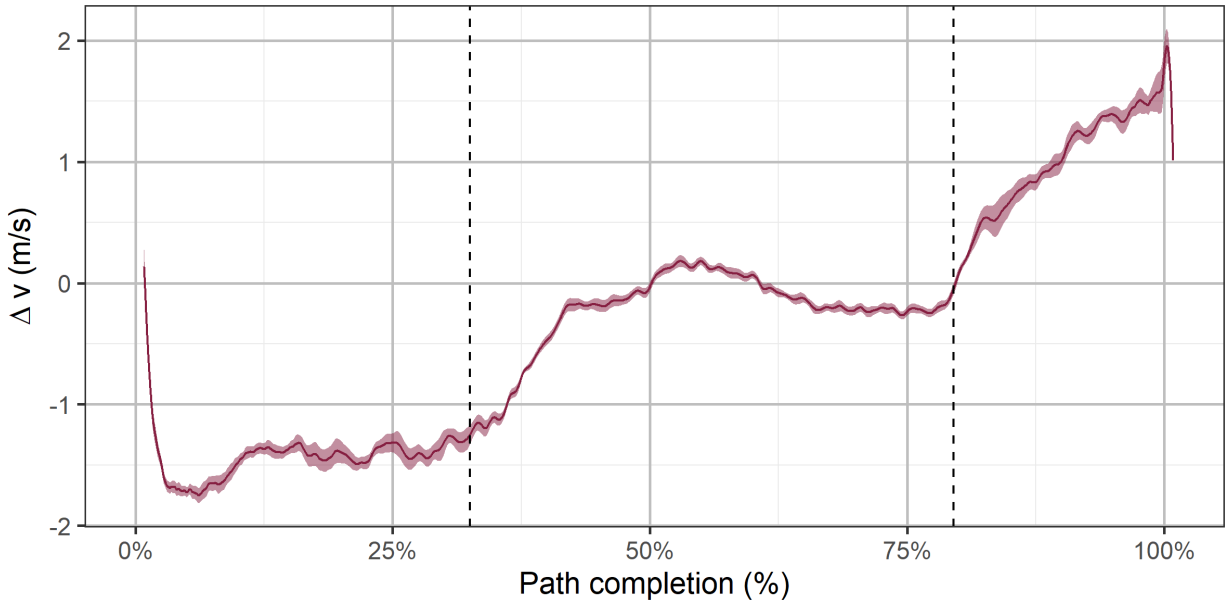

Figure 22. Ensemble average Δv vs. TC$_{\%}$ for the v_{target} = 17.9 m/s, a_x^+ 2.5 m/s^2, a_x^- = 3.9 m/s^2 start-to-stop DV (S1.0, non-disturbance, Vehicle A)

Investigating the secondary metrics gave further insight into the control system characterization. Figure 23 shows the difference in longitudinal acceleration between the ADS response and the reference profile, and Figure 24 shows the instantaneous local time lag. Both figures show that the control system lagged in the throttle tip-in. The local time lag slowly grew during the acceleration phase because the longitudinal acceleration was never able to compensate for the initial throttle lag until during the constant speed phase. Next, the lag in brake actuation occurred during the transition from constant speed to braking. After matching the brake request, the control system compensated for the initial lag by braking harder than requested. Finally, the brake torque lessened as the system approached the end of the path, overshooting the stopping point.

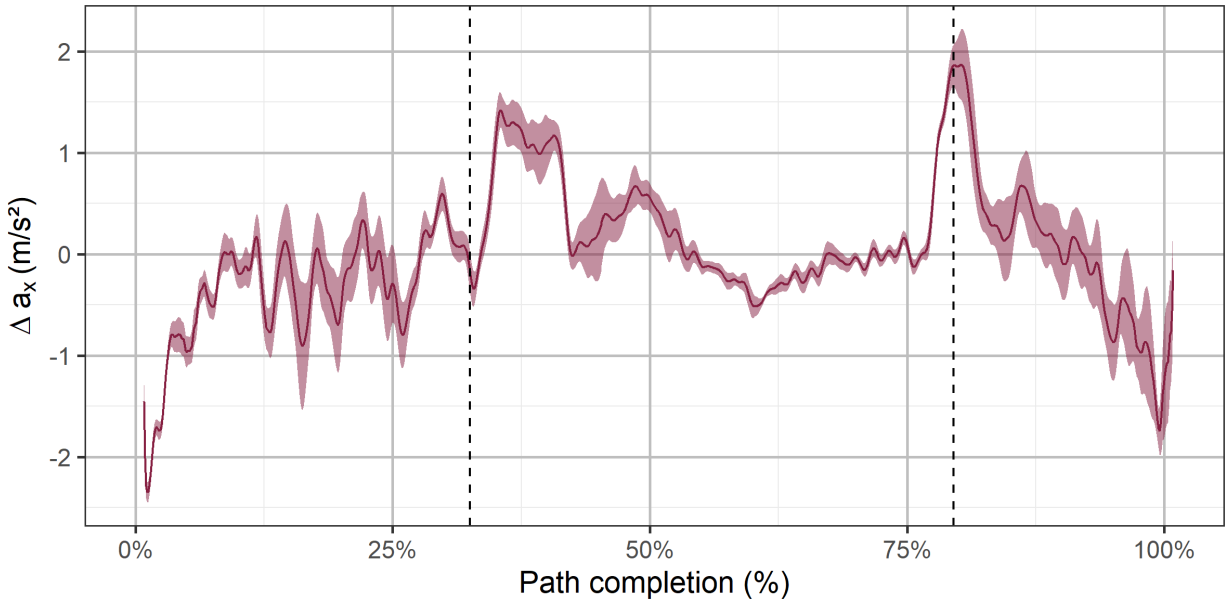

Figure 23. Ensemble average Δa_x vs. TC$_{\%}$ for the v_{target} = 17.9 m/s, a_x^+ 2.5 m/s^2, a_x^- = 3.9 m/s^2 m/s^2 start-to-stop DV (S1.0, non-disturbance, Vehicle A)

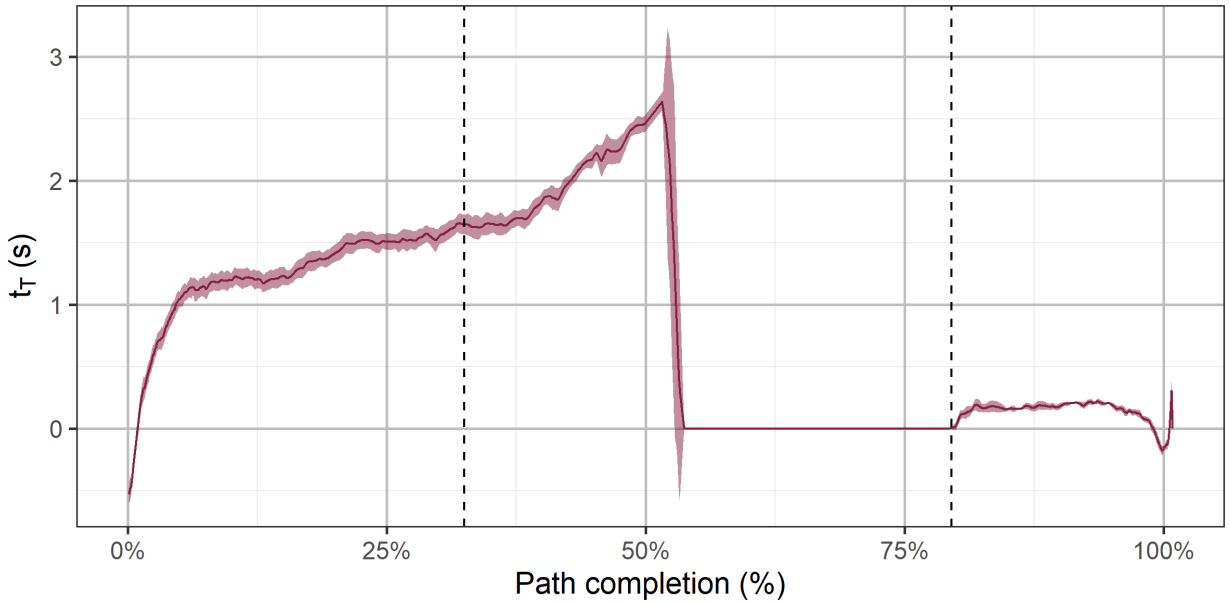

Figure 24. Ensemble average t_T vs. TC$_{\%}$ for the v_{target} = 17.9 m/s, a_x^+ 2.5 m/s^2, a_x^- = 3.9 m/s^2 start-to-stop DV (S1.0, non-disturbance, Vehicle A)

The stopping point error for each DV is given in Figure 25. All errors were positive, indicating that the vehicle always overshot the stop point. Increasing braking magnitudes yielded a larger stop error. Conversely, increasing the target speed showed a diverging trend; at lower target speeds, low braking magnitudes slightly improved stop error while high braking magnitudes worsened stop error. This observation is possibly because there was more time for

the control system to recover from the initial brake lag at higher speeds and low deceleration rates. As mentioned above, the heightened stop error for the 24.6 m/s target speed was possibly due to the slight downhill grade of the test track.

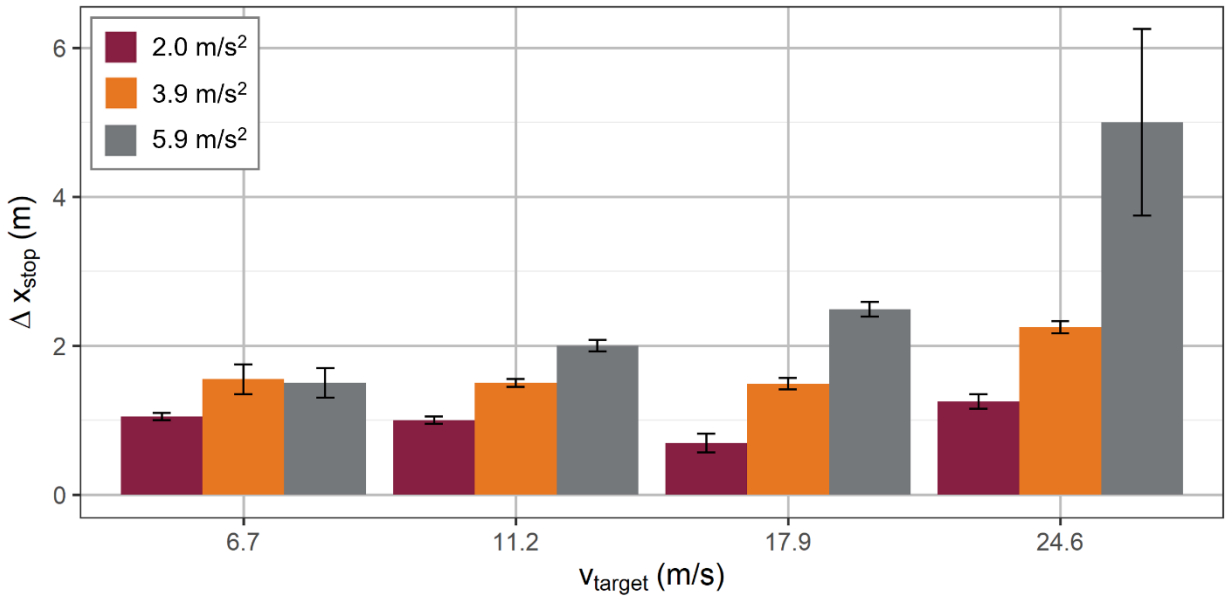

Figure 25. Average Δx_{stop} for each v_{target} and a_x^- magnitude (S1.0, non-disturbance, Vehicle A)

4.1.2 Scenario 1.1

The longitudinal sinusoid helped characterized the transient response of the longitudinal control mechanisms. When comparing the reduced travel speed (v_{lower} = 6.7 m/s) and full stop sinusoids (v_{lower} = 0 m/s), Figure 26 indicated that the average Δv for the acceleration and braking phases showed similar performance across all DVs. Conversely, Figure 27 showed that the average local time lag showed some differences, primarily in the acceleration regime. The full stop DVs produced significantly larger average local time lags; most of this increase occurred during the initial acceleration from the stop event, which suggests that there was a delay in throttle actuation after each stop event. Overall, the behavior of the system lags during braking were similar, on average, to Scenario 1.0.

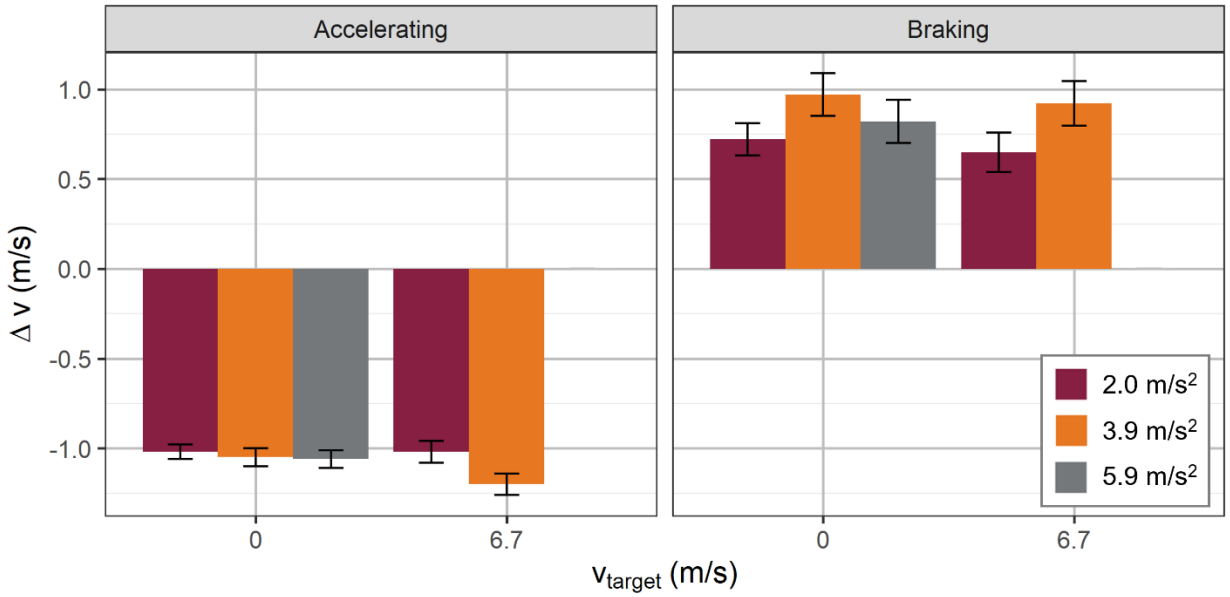

Figure 26. Average Δ*v* for each longitudinal sinusoid segmented across the acceleration and braking phases (S1.1, Vehicle A)

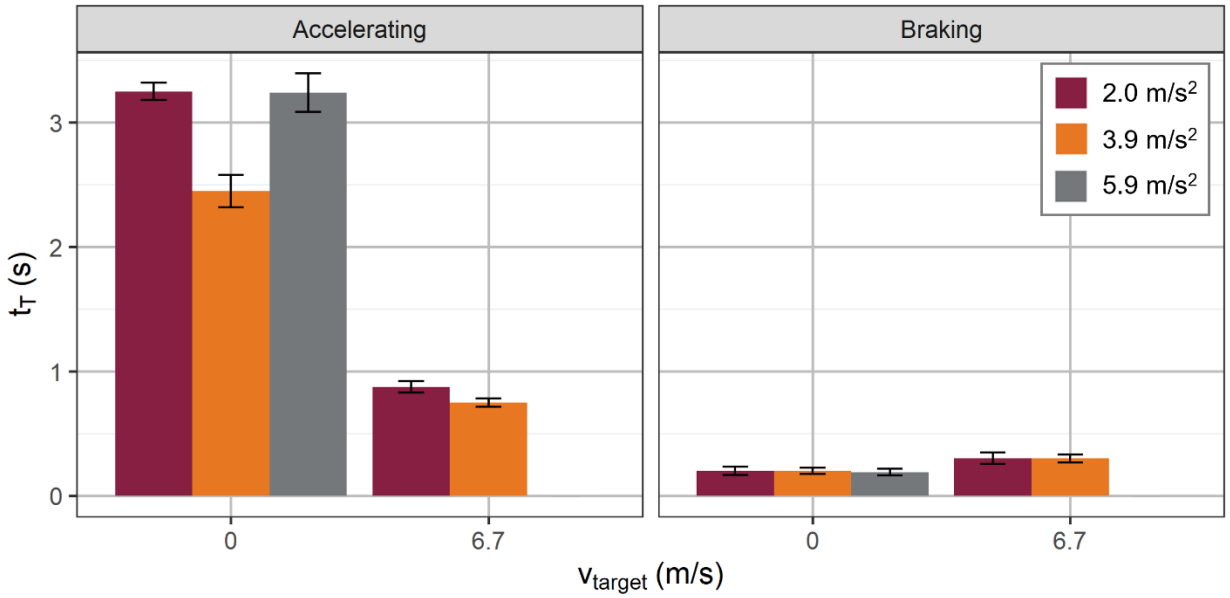

Figure 27. Average t_T for each longitudinal sinusoid segmented across the acceleration and braking phases (S1.1, non-disturbance, Vehicle A)

In addition to aggregate statistics, the speed traces relative to the reference speed profile provided further insight into the motion control system. Figure 28 and Figure 29 give the absolute speed traces for the v_{lower} = 0 and 6.7 m/s DVs at a 3.9 m/s^2 deceleration magnitude, respectively. For the v_{lower} = 0 m/s maneuver, there was a consistent phase lag for the entire maneuver, and the acceleration portion never reached the initial target velocity after the first

braking event. Also, the reference profile did not come to a complete stop after the third braking event, which is possibly why the ADS playback never reached the minimum velocity during that braking event. On the other hand, the ADS playback of the v_{lower} = 6.7 m/s maneuver yielded a slight phase lag and reduced amplitude sinusoid, where both the velocity peaks and troughs were rounded. In addition to the throttle and brake actuator lag observed from Scenario 1.0, the reduced speed amplitude likely occurred because Vehicle A's longitudinal controller utilized a velocity look-ahead algorithm that may soften speed transitions.

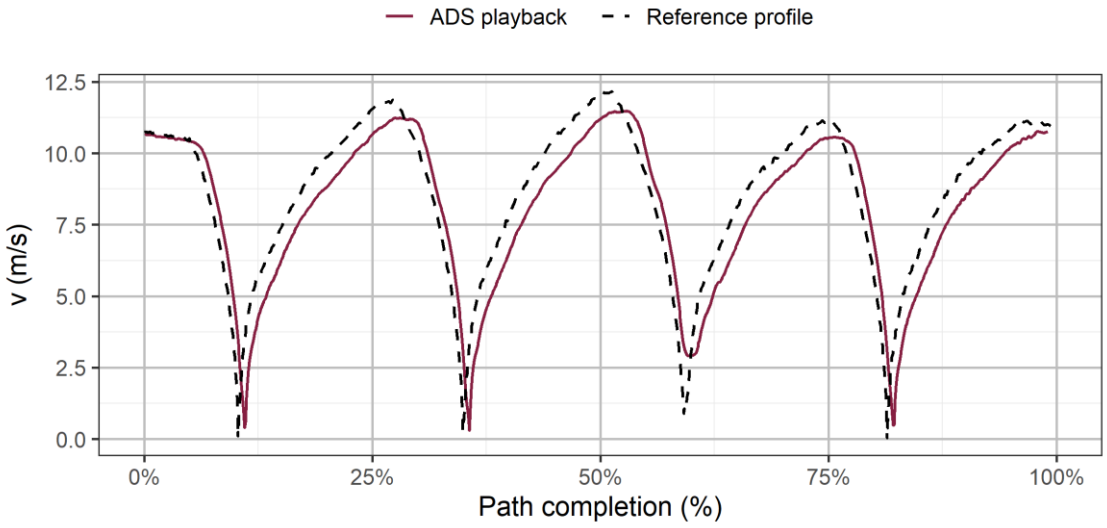

Figure 28. Ensemble average v vs. TC$_{\%}$ for the v_{lower} = 0 m/s, a_x^- = 3.9 m/s^2 longitudinal sinusoid (S1.1, non-disturbance, Vehicle A)

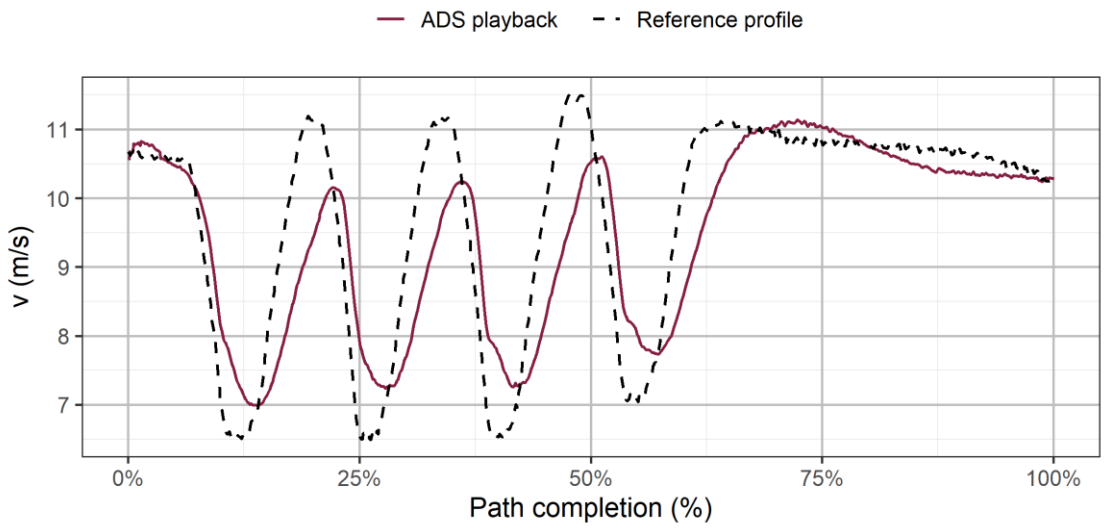

Figure 29. Ensemble average v vs. TC$_{\%}$ for the v_{lower} = 6.7 m/s, a_x^- = 3.9 m/s^2 longitudinal sinusoid (S1.1, non-disturbance, Vehicle A)

Figure 30 compares the stops error in Scenario 1.0 and 1.1 for each braking magnitude. The Scenario 1.1 stop error was slightly higher than Scenario 1.0 for matching deceleration parameters.

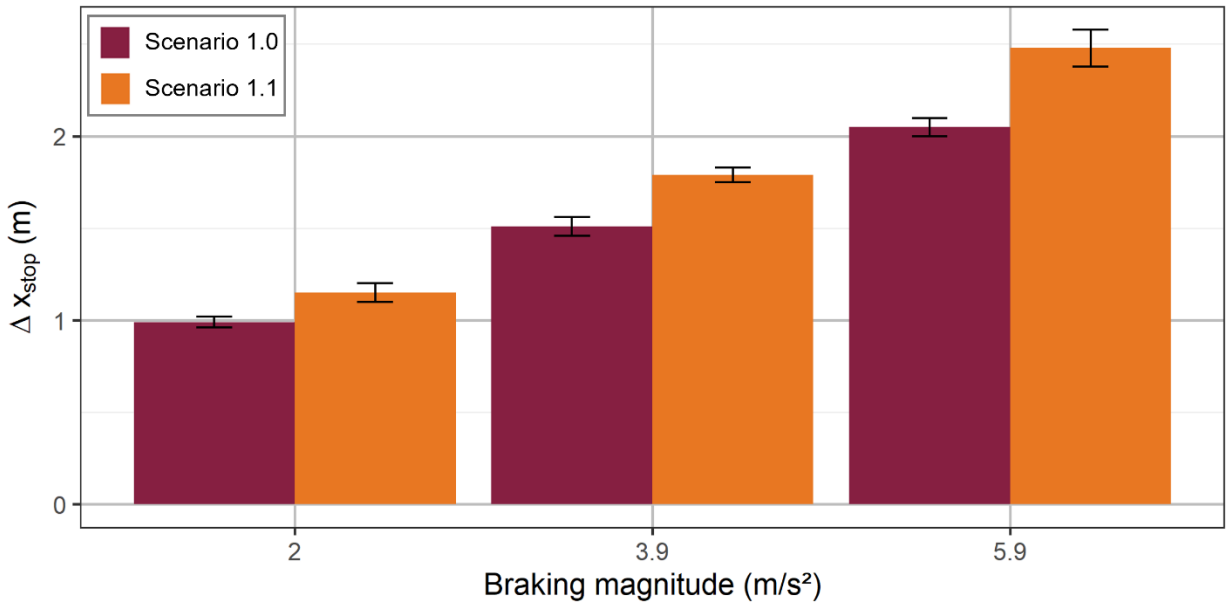

Figure 30. Comparison of the average Δx_{stop} for each a_x^- magnitude (S1.0 vs. S1.1, non-disturbance, Vehicle A)

4.2 Lane Change Maneuver

4.2.1 Scenario 2.0

Scenario 2.0 was used to characterize the response of the lateral control system to a step steer input and the response of the brake actuators immediately after a lane change. Figure 31 illustrates the method's ability to characterize the control systems by showing the path trajectory differences between both test vehicles during the double lane change maneuver. The control system of Vehicle A softened the corner relative to the reference path at both design speeds. Conversely, Vehicle B consistently showed a small lag at the lane change initiation followed by a speed-dependent response at the completion of the lane change. At 11.2 m/s, Vehicle B exhibited minimal overshoot and followed the path closely, but at 17.9 m/s, the vehicle exhibited almost 2 meters of overshoot in the first lane change. To compensate for this initial overshoot, the vehicle shifted to the right during the dwell section. The second lane change demonstrated a similar behavior; the vehicle overshot by approximately 1.5 meters before the system applied corrective steering.

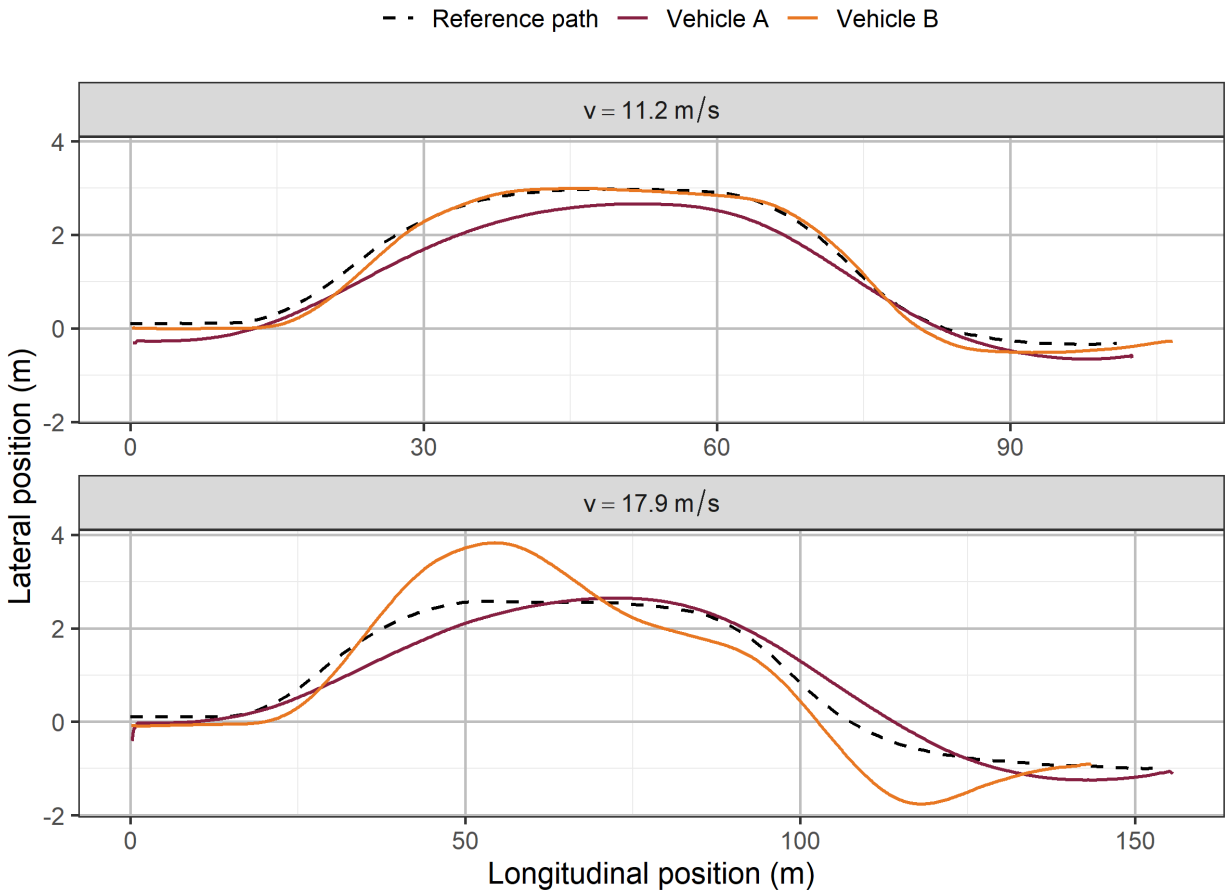

Figure 31. Trajectory plots for the v_{target} = 11.2 m/s (top) and 17.9 m/s (bottom) double lane change with braking at a_x^- = 3.9 m/s^2 (S2.0, non-disturbance, both vehicles). The dashed line represents the reference path

Figure 32 shows ΔY for the double lane change maneuvers, and Table 18 gives the average RMS and average absolute maximum of ΔY. Like the straight-line scenarios, Vehicle A showed a right-side bias with nearly constant variance. For the 17.9 m/s lane change, the vehicle also exhibited a slight phase lag, causing the response to be to the right of the reference path during the first lane change and to the left of the reference path during the second lane change. Aside from the initial lag and final overshoot, Vehicle B followed the path of the 11.2 m/s lane closely with standard deviation of below 0.1 meters. Conversely, Vehicle B demonstrated an overshoot of over 1 meter for both lane changes for the 17.9 m/s design variation. Additionally, Vehicle B departed from its precision during the first lane change, which had a ΔY with an average standard deviation of approximately 0.62 meters.

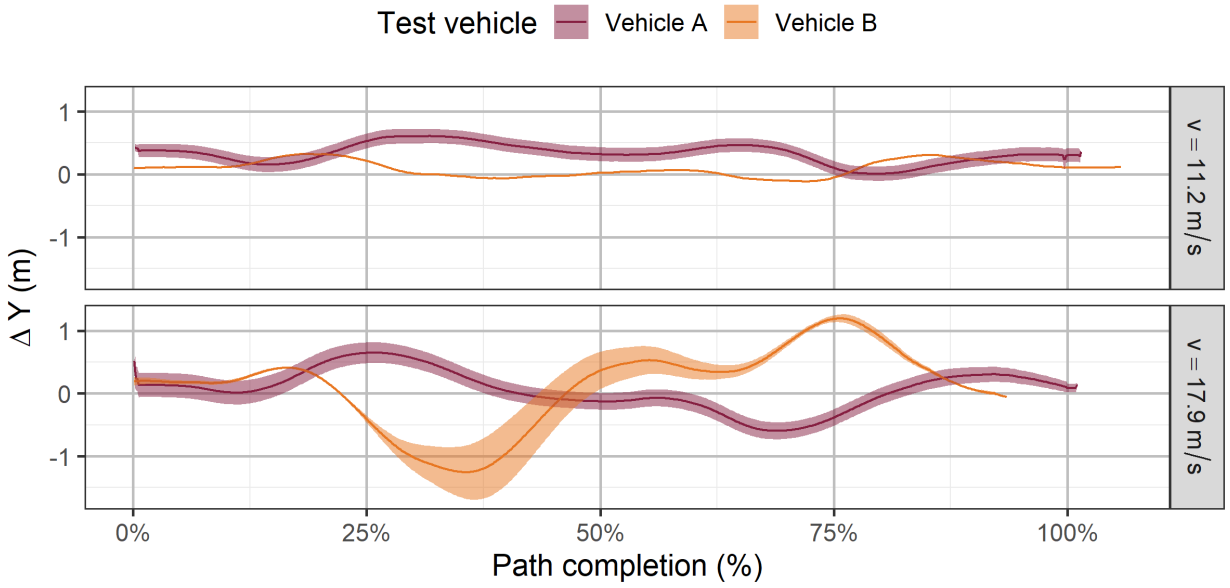

Figure 32. Ensemble average ΔY vs. $TC_{\%}$ for the v_{target} = 11.2 m/s (top) and 17.9 m/s (bottom) double lane change with braking at a_x^- = 3.9 m/s^2 (S2.0, non-disturbance, both vehicles)

Table 18. Average of ΔY_{RMS} and ΔY_{absmax} across all lane change with braking tests for both DVs (S2.0, non-disturbance, both vehicles)

Test Vehicle	v_{target} (m/s)	ΔY_{RMS} (m)	ΔY_{absmax} (m)
A	11.2	0.36	0.61
B	11.2	0.16	0.32
A	17.9	0.32	0.65
B	17.9	0.64	1.25

Figure 33 investigates the corrected lateral offset, which subtracts the mean ΔY during the first 5% of the maneuver from the entire ΔY trace. After applying this correction, the standard deviation of the response shrunk. This observation indicated that the lateral controller of Vehicle A was precise but not accurate, and these accuracy issues occurred because the ΔY bias stemmed from input errors in the localization. On the other hand, Vehicle B did not exhibit noticeable input errors during the localization as seen by the similar ΔY and ΔY_{offset} traces. In short, the method demonstrated the ability of the metrics to quantify the accuracy and precision of the system responses.

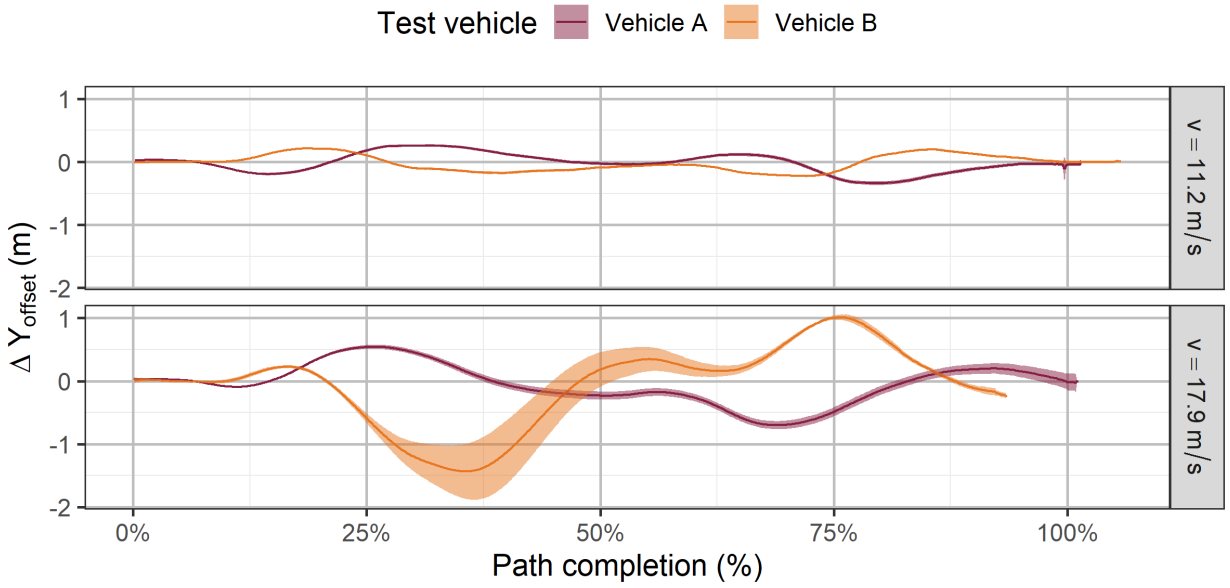

Figure 33. Ensemble average ΔY_{offset} vs. $TC_{\%}$ for the v_{target} = 11.2 m/s (top) and 17.9 m/s (bottom) double lane change with braking (S2.0, non-disturbance, both vehicles)

Comparing the stop points in Scenario 1.0 and Scenario 2.0 in Figure 34 shows that the addition of the double lane change yielded no practical difference in stop error. Because the 3.9 m/s^2 deceleration was outside the design constraints of Vehicle B, the stop points were not evaluated for this vehicle.

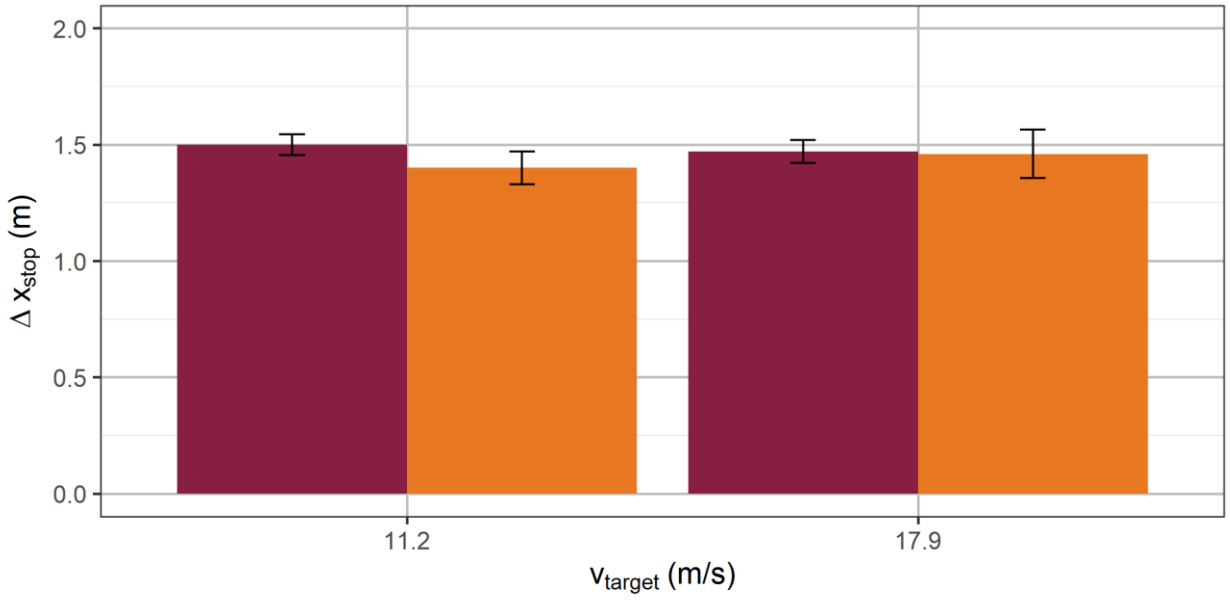

Figure 34. Comparison of the average Δx_{stop} for the v_{target} = 11.2 m/s and 17.9 m/s DVs (S1.0 vs. S2.0, non-disturbance, Vehicle A)

4.3 Intersection Maneuvers

4.3.1 Scenario 3.0

Scenario 3.0 investigated the effect of various cornering radii at a given lateral acceleration. Figure 35 and Figure 36 show the trajectory of both test vehicles during the constant speed cornering maneuver for the typical (2.9 m/s^2) and harsh (4.4 m/s^2) lateral acceleration DVs, respectively. Like the lane change maneuvers, Vehicle A cut the corners relative to the reference path for both lateral acceleration DVs. However, Vehicle A also cut the corner more (i.e., larger absolute ΔY) for smaller turn radii due to the speed-dependent look-ahead parameter in the steering algorithm. Most notably, Vehicle A was unable to fully complete the DV with the 7.6-meter radius and harsh lateral acceleration because it would run off the test track, proving that the method was able to detect control system failures. On the other hand, Vehicle B accurately and precisely followed the reference path. To further study the path following ability of each vehicle, Table 19 summarizes the aggregate statistics of ΔY, and Figure 37 shows the ensemble averaged ΔY for each test trial to clearly capture the path deviation. Vehicle B was able to follow the path with a maximum deviation of 0.2 meters and RMS ΔY of 0.1 meters. Vehicle A exhibited larger path deviations, particularly at 4.4 m/s^2, where the vehicle was over 2.5 meters off path with a root-mean-square (RMS) value approaching 1 meter.

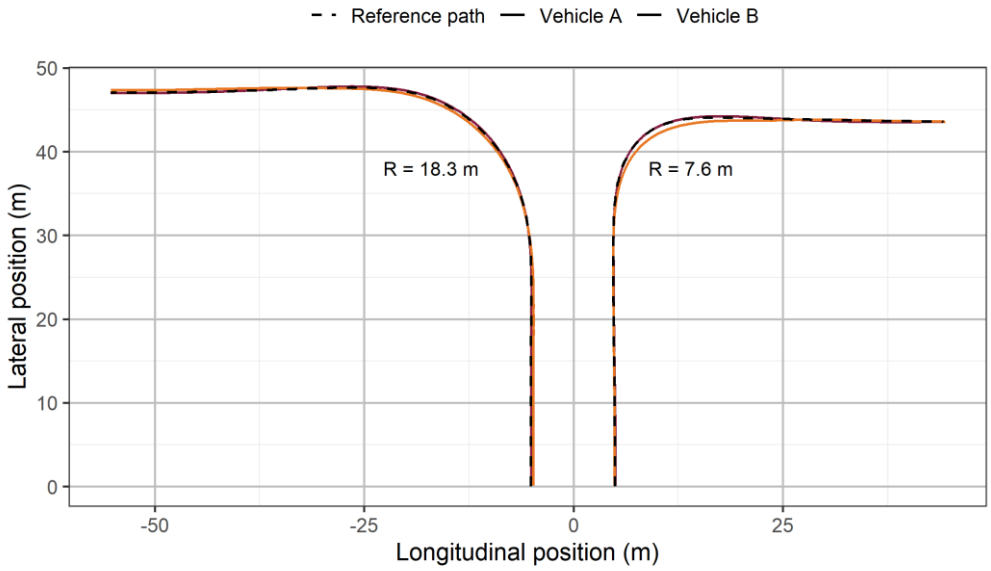

Figure 35. Trajectory plots for the *R* = 18.3 m (left) and *R* = 7.6 m (right) constant speed turns at a_y = 2.9 m/s^2 (S3.0, non-disturbance, both vehicles). The dashed line represents the reference path

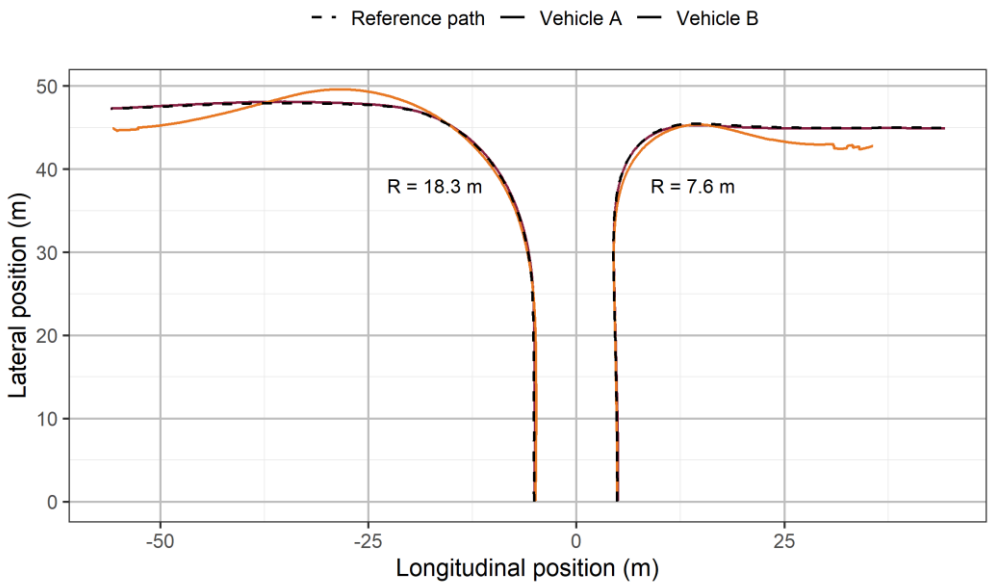

Figure 36. Trajectory plots for the *R* = 18.3 m (left) and *R* = 7.6 m (right) constant speed turns at a_y = 4.4 m/s^2 (S3.0, non-disturbance, both vehicles). The dashed line represents the reference path

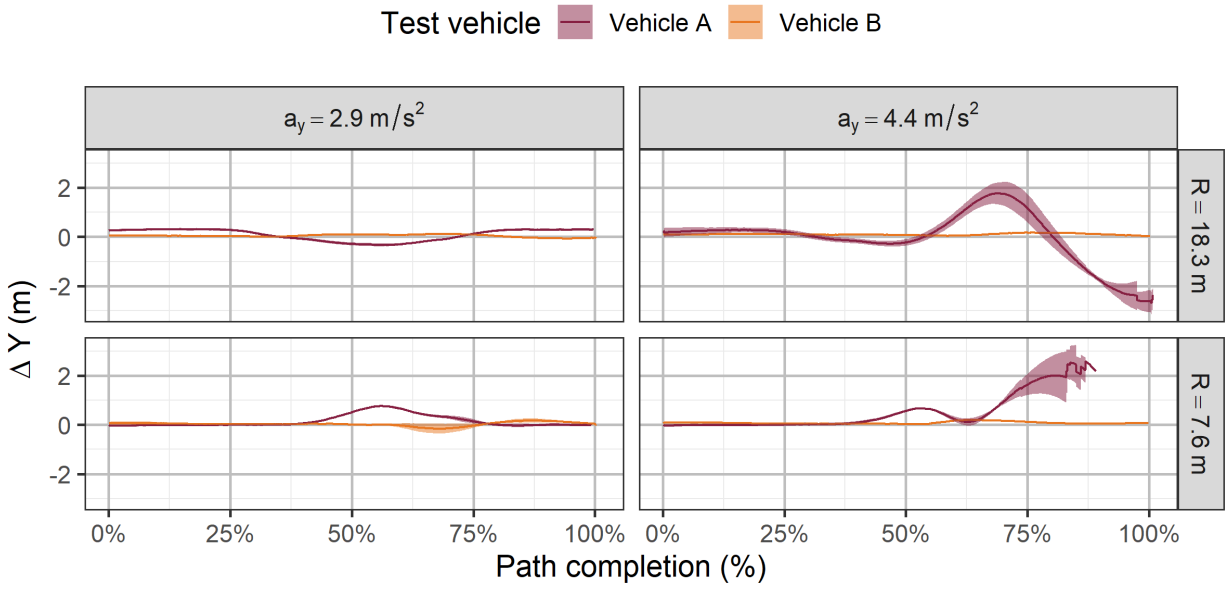

Figure 37. Ensemble average ΔY vs. TC$_{\%}$ for the constant speed turns across all v_{target} and a_y DVs (S3.0, non-disturbance, both vehicles)

Table 19. Average of ΔY_{RMS} and ΔY_{absmax} across all constant speed intersection turn tests for each DV (S3.0, non-disturbance, both vehicles)

Test Vehicle	a_y (m/s^2)	r (m)	ΔY_{RMS} (m)	ΔY_{absmax} (m)
A	2.9	7.6	0.28	0.76
B	2.9	7.6	0.08	0.17
A	2.9	18.3	0.25	0.33
B	2.9	18.3	0.07	0.12
A	4.4	7.6	0.94	2.59
B	4.4	7.6	0.09	0.20
A	4.4	18.3	1.04	2.69
B	4.4	18.3	0.10	0.17

Once the method determined that a lateral control limit existed between 3.0 and 4.4 m/s^2, Vehicle A was additionally tested at two intermediate lateral acceleration limits: 3.4 m/s^2 and 3.9 m/s^2. The trajectory and ΔY_{offset} versus path completion plots of the 3.4, 3.9, and 4.4 m/s^2 DVs are given in Figure 38 and Figure 39, respectively. Increasing the lateral acceleration along a constant radius required the vehicle to negotiate the turn at a higher speed, thus requiring a larger yaw rate from the control system. After plotting the yaw error, lateral acceleration response, and yaw rate response of the ADS in Figure 40, it was determined that Vehicle A's lateral motion controller was limited to approximately 3.5 m/s^2, which translated to a yaw rate limit of 24 deg/s.

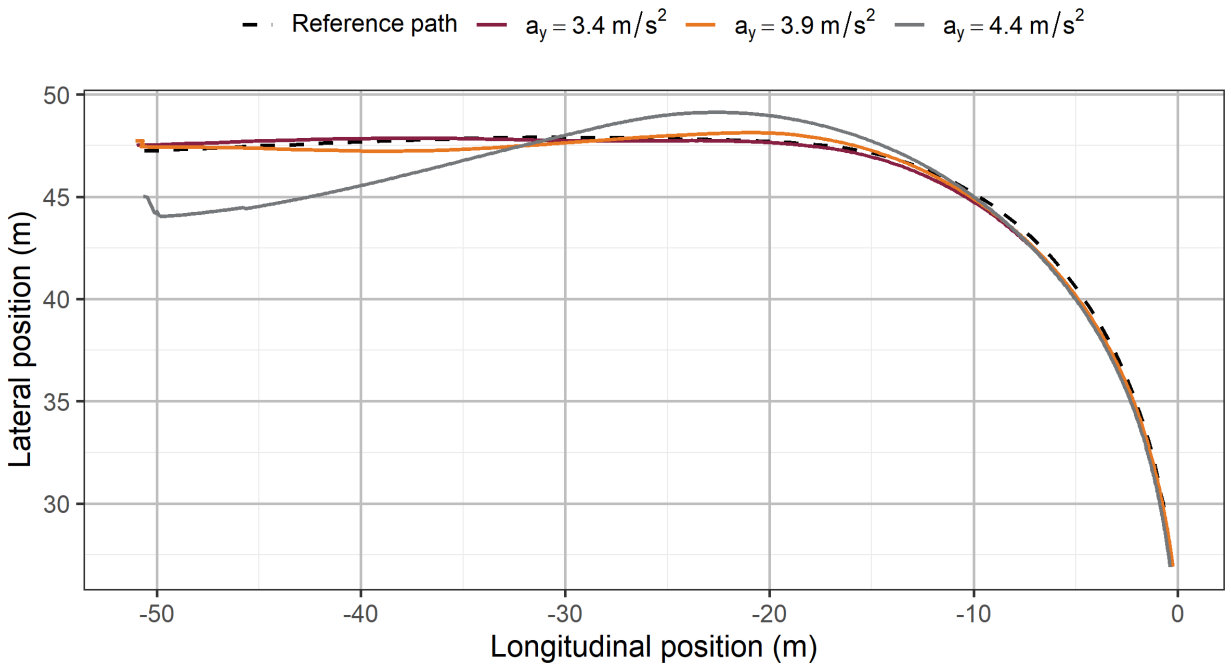

Figure 38. Trajectory plots for the R = 18.3 m constant speed turns at a_y = 3.4, 3.9, and 4.4 m/s^2 (S3.0, non-disturbance, Vehicle A). The dashed line represents the reference path

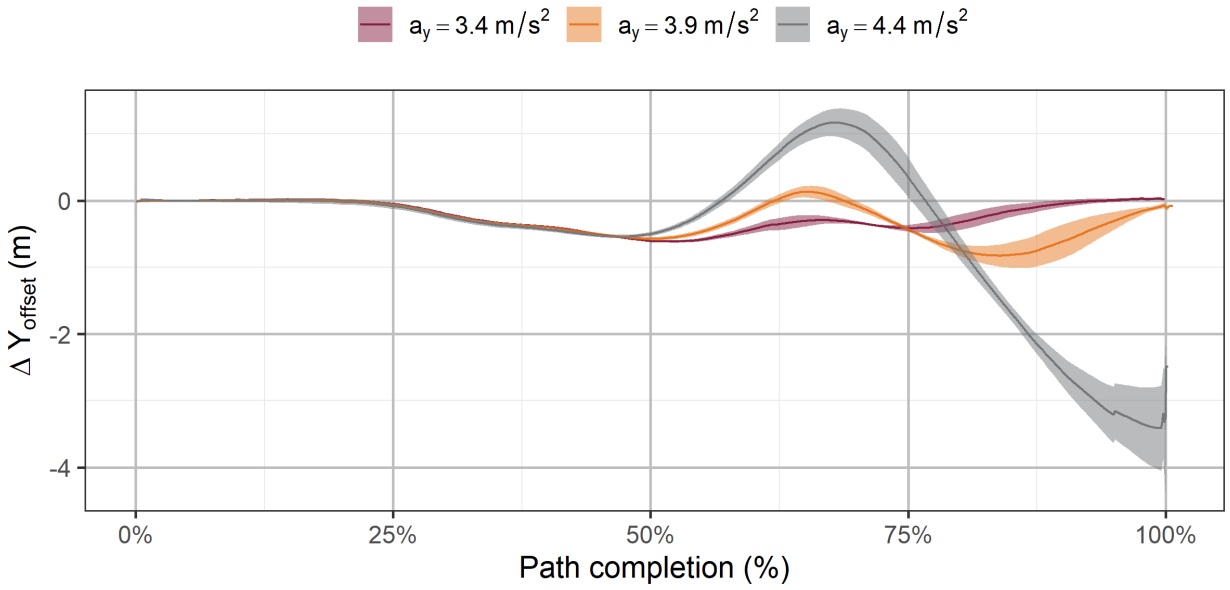

Figure 39. Ensemble average ΔY_{offset} vs. $TC_{\%}$ for the R = 18.3 m constant speed turns at a_y = 3.4, 3.9, and 4.4 m/s^2 (S3.0, non-disturbance, Vehicle A)

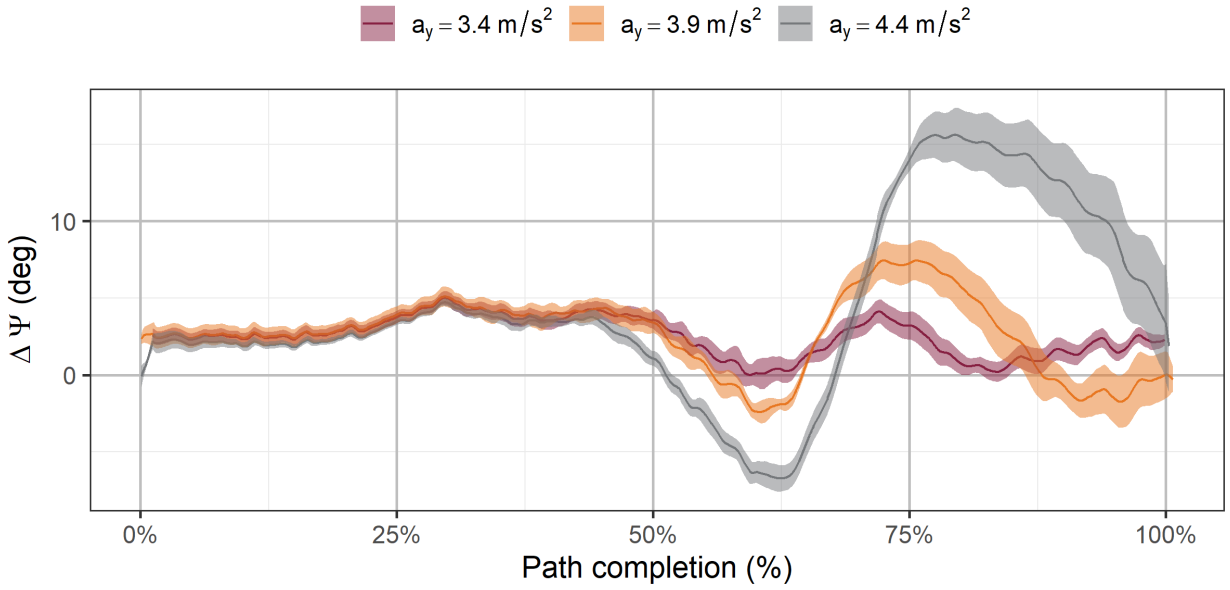

Figure 40. Ensemble average $\Delta\Psi$ vs. $TC_{\%}$ for the R = 18.3 m turns at a_y = 3.4, 3.9, and 4.4 m/s^2 (S3.0, non-disturbance, Vehicle A)

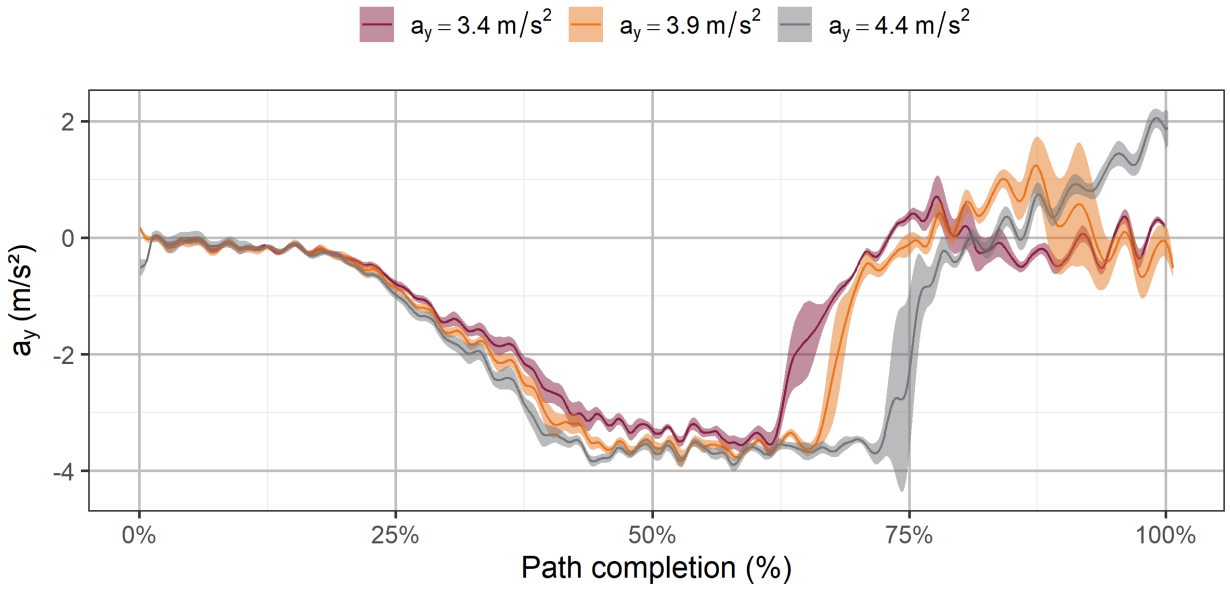

Figure 41. Ensemble average a_y vs. TC% for the R = 18.3 m turns at a_y = 3.4, 3.9, and 4.4 m/s² (S3.0, non-disturbance, Vehicle A)

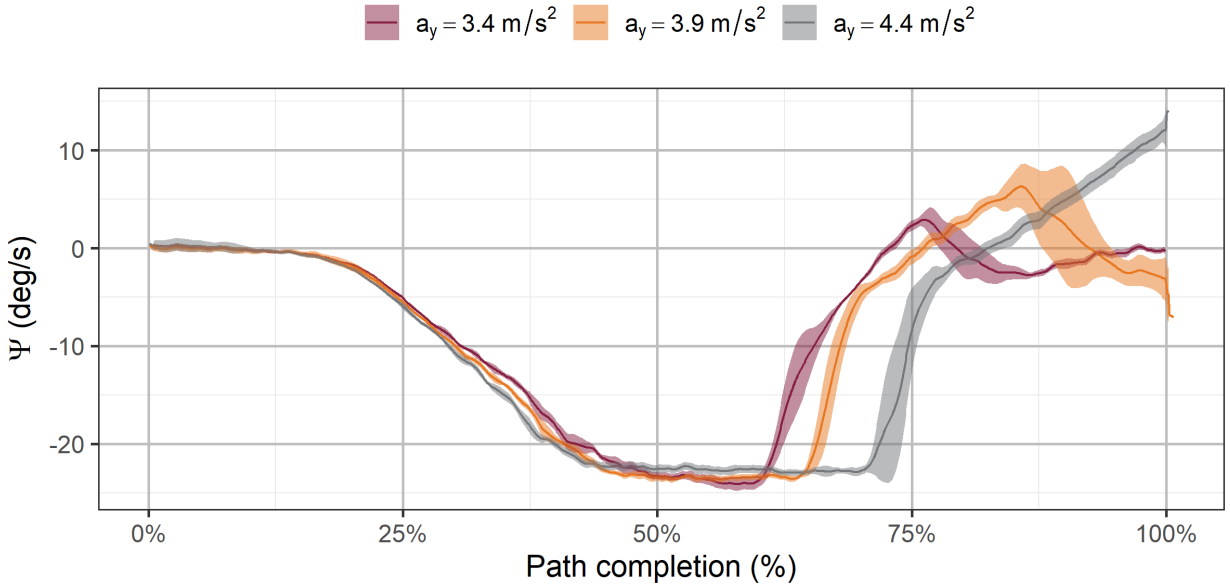

Figure 42. Ensemble average Ψ vs. TC% for the R = 18.3 m turns at a_y = 3.4, 3.9, and 4.4 m/s² (S3.0, non-disturbance, Vehicle A)

4.3.2 Scenario 3.1

Scenario 3.1 expands on Scenario 3.0 by characterizing the vehicle's longitudinal and lateral response during simultaneous cornering and accelerating. Figure 43 and Figure 44 show the trajectory of both test vehicles during the cornering maneuvers beginning from rest for lateral

acceleration DVs of 1.5 m/s^2 and 2.9 m/s^2, respectively. Lower lateral accelerations were allowed for this scenario because the maneuver begins from rest, and lateral acceleration is dependent on the vehicle's speed. Both vehicles followed the same lateral control trends as those seen during the 2.9 m/s^2 DV of Scenario 3.0 and the same longitudinal control trends as those seen during the straight-line maneuvers.

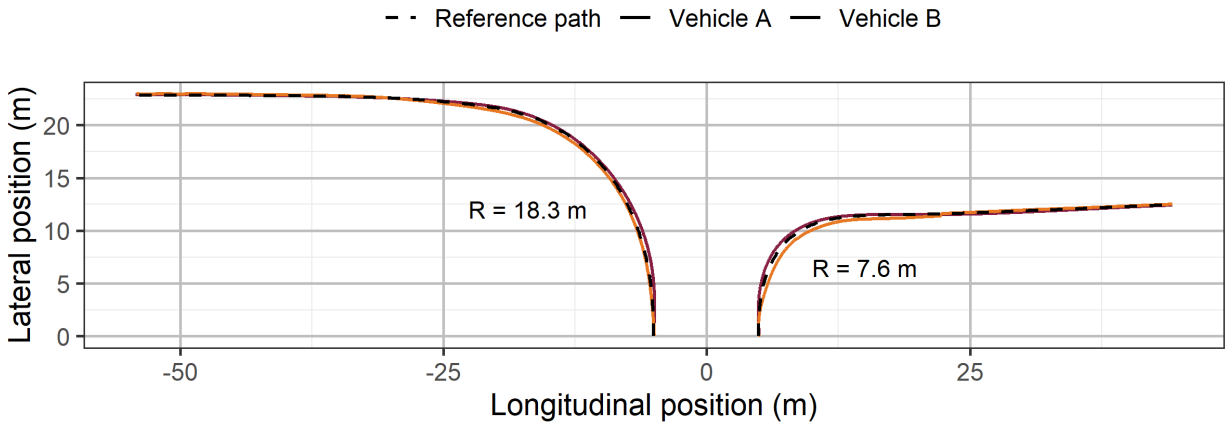

Figure 43. Trajectory plots for the *R* = 18.3 m (left) and *R* = 7.6 m (right) turns from rest at a_y = 1.5 m/s^2 (S3.1, non-disturbance, both vehicles). The dashed line represents the reference path

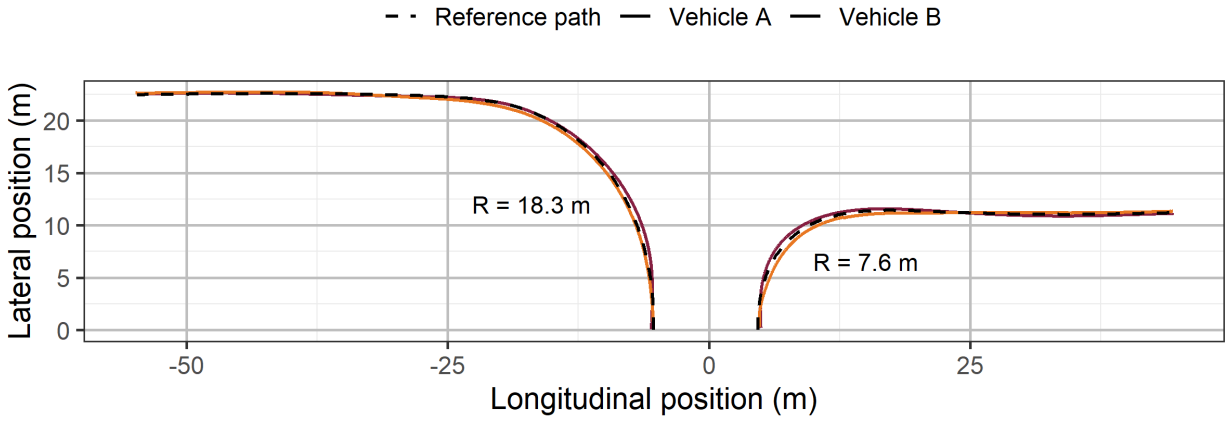

Figure 44. Trajectory plots for the *R* = 18.3 m (left) and *R* = 7.6 m (right) turns from rest at a_y = 1.5 m/s^2 (S3.1, non-disturbance, both vehicles). The dashed line represents the reference path

Similar to the longitudinal acceleration phase of Scenario 1.0, the control system of both vehicles lagged during the initial throttle tip-in before catching up. Figure 45 and Figure 46 plot the Δa_x and Δv traces for the 7.6 m radius and 2.9 m/s^2 DV. However, Vehicle A caught up to the target speed while Vehicle B failed to continue accelerating after the initial tip-in, causing it to undershoot the target velocity by approximately 2 m/s. It should be noted that, although it was

known that Vehicle B was not designed to maintain longitudinal accelerations beyond 1.5 m/s^2, the method was still able to highlight this behavior.

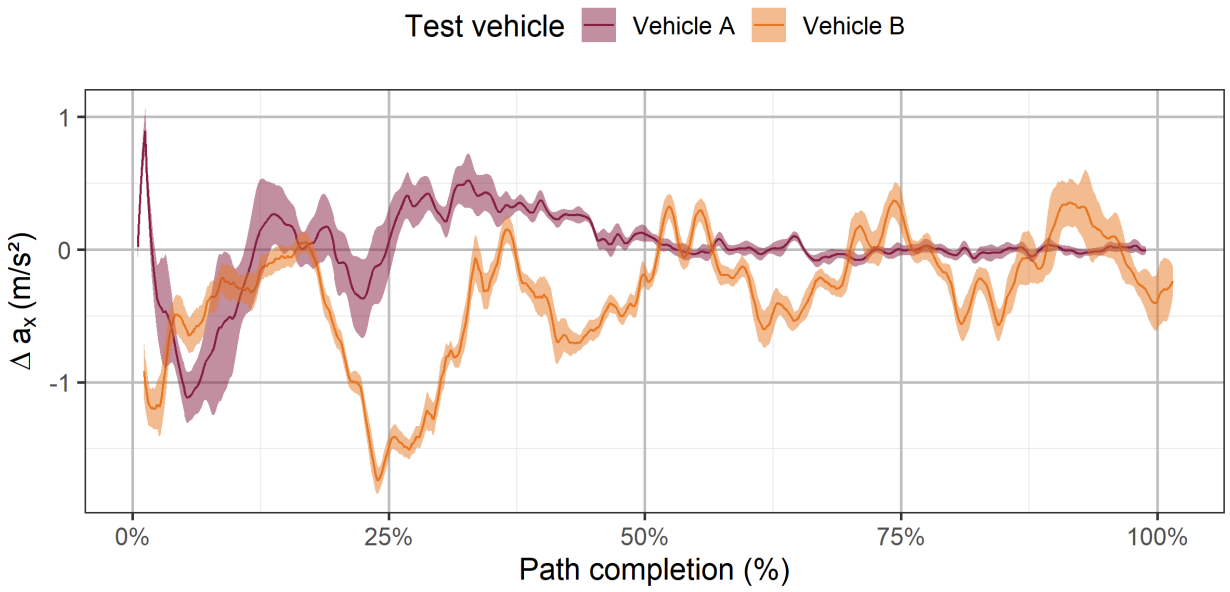

Figure 45. Ensemble average Δa_x vs. TC$_{\%}$ for the R = 7.6 m turns at a_y = 2.9 m/s^2 (S3.1, non-disturbance, both vehicles)

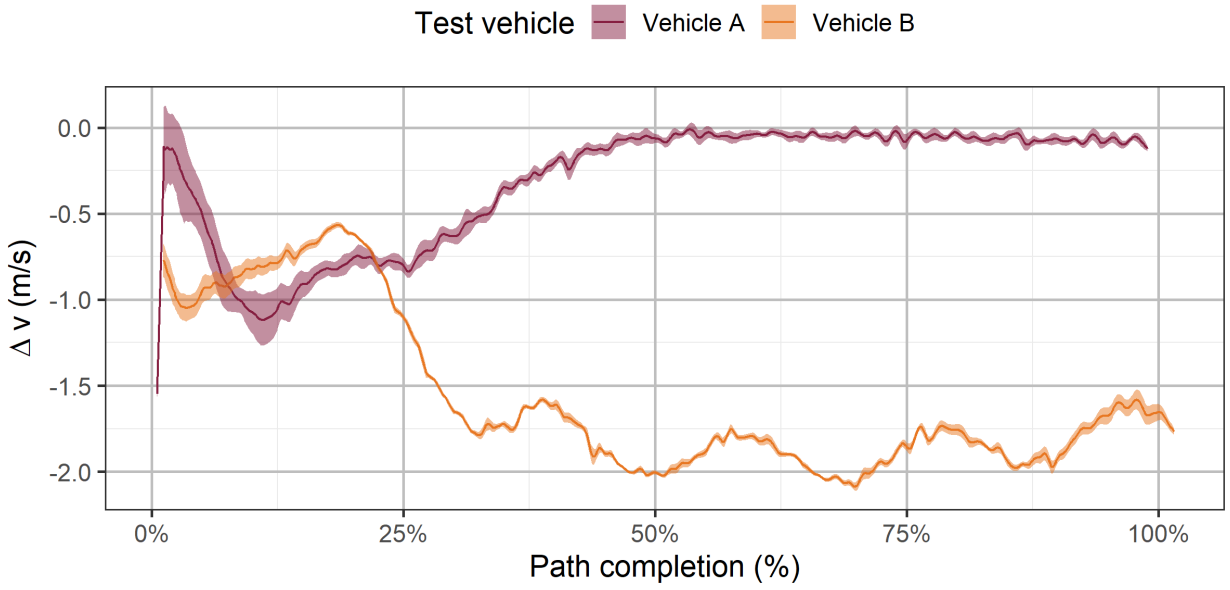

Figure 46. Ensemble average Δv vs. TC$_{\%}$ for the R = 7.6 m turns at a_y = 2.9 m/s^2 (S3.1, non-disturbance, both vehicles)

4.3.3 Scenario 3.2

Scenario 3.2 expands on Scenario 3.0 by characterizing the vehicle's longitudinal and lateral response during simultaneous cornering and braking. Like the previous cornering maneuvers, Vehicle A initiated the turn slightly early and cut the corner of the reference trajectory, while Vehicle B began turning late and had to turn slightly harder during the maneuver to correct itself. Figure 47 shows the trajectory of both test vehicles during the transient cornering maneuvers that involve braking from an entrance speed of 11.2 m/s and accelerating at the apex of the turn.

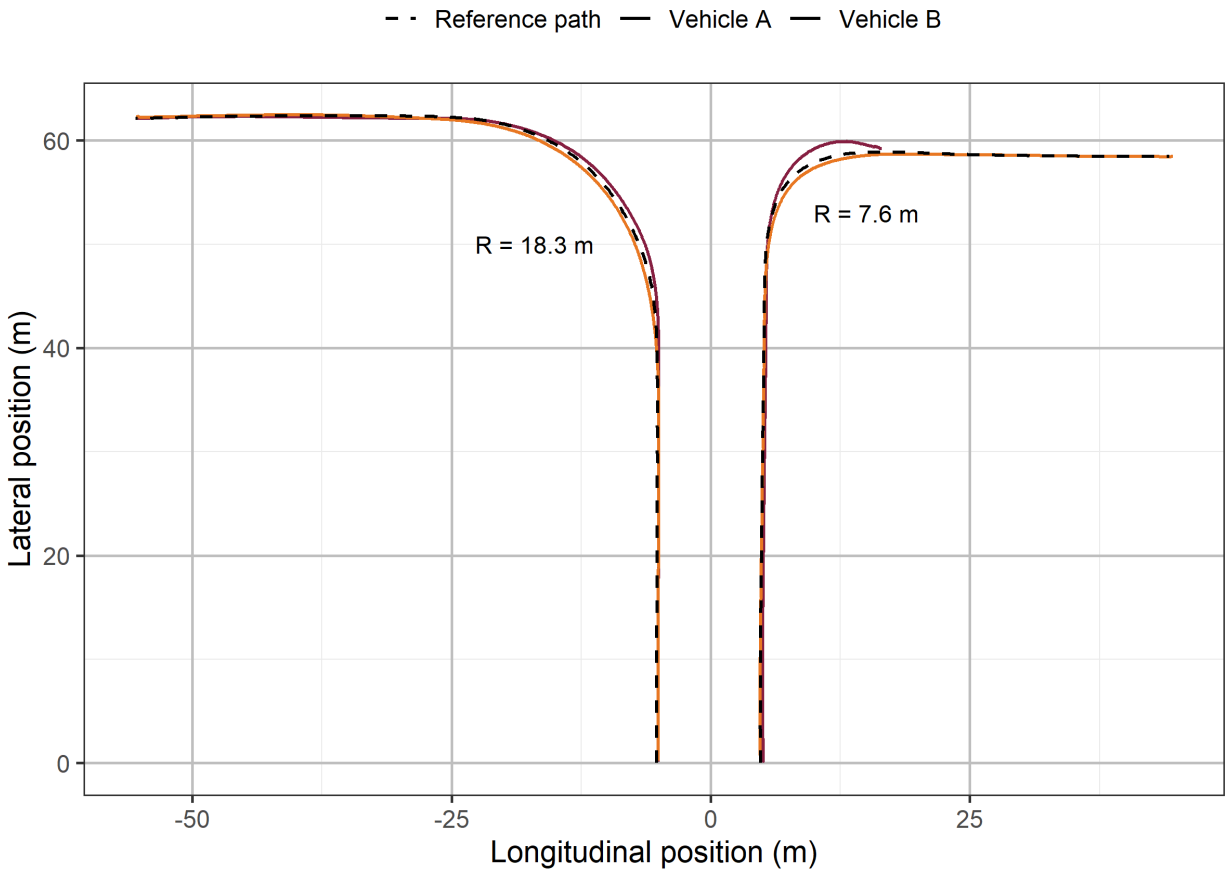

Figure 47. Trajectory plots for the *R* = 18.3 m (left) and *R* = 7.6 m (right) transient turns beginning at v_{start} = 11.2 m/s (S3.2, non-disturbance, both vehicles). The dashed line represents the reference path

Figure 48 describes the Δv traces of both vehicles, demonstrating that Vehicle A was able to follow the speed profile of the reference path within ±1 m/s while Vehicle B overshot the reference speed profile by up to 6 m/s once braking was initiated. This occurred because the

braking requests fell outside the design constraints of Vehicle B, causing the longitudinal controller to undershoot the target longitudinal acceleration by approximately 1 m/s^2 (Figure 49). Despite this limitation, Vehicle B was still able to complete the larger radius turn, but Figure 50 illustrates how the smaller turn could not be completed due to the large yaw acceleration required to negotiate a tight turn at high speeds, evident in the large increase in heading error. Like Scenario 3.1, the method was able to highlight the known limitations in Vehicle B's longitudinal response.

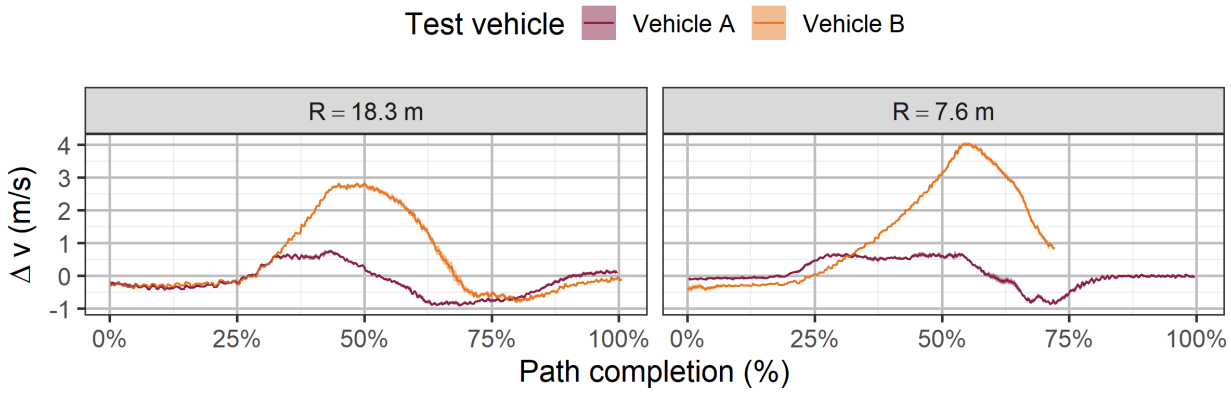

Figure 48. Ensemble average Δv vs. TC$_{\%}$ for the R = 18.3 m (left) and R = 7.6 m (right) transient turns beginning at v_{start} = 11.2 m/s (S3.2, non-disturbance, both vehicles)

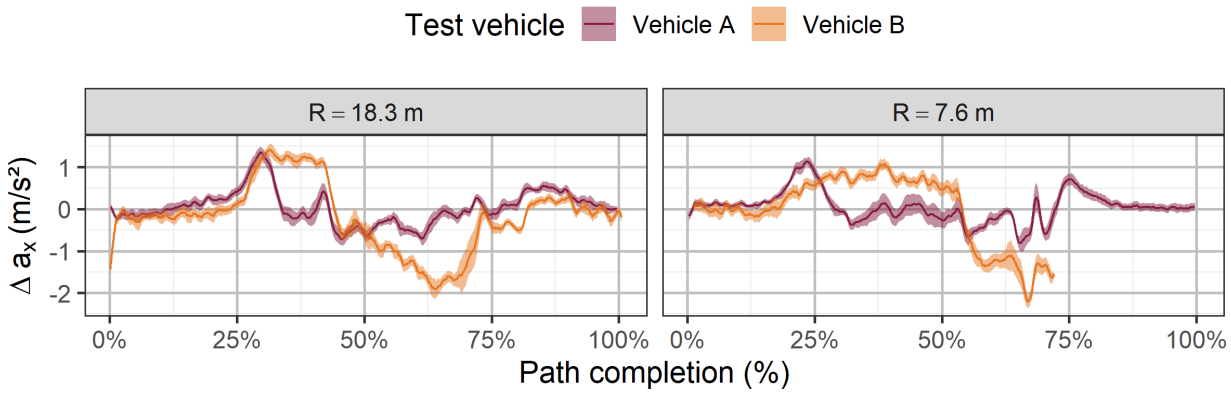

Figure 49. Ensemble average Δa_x vs. TC$_{\%}$ for the R = 18.3 m (left) and R = 7.6 m (right) transient turns beginning at v_{start} = 11.2 m/s (S3.2, non-disturbance, both vehicles)

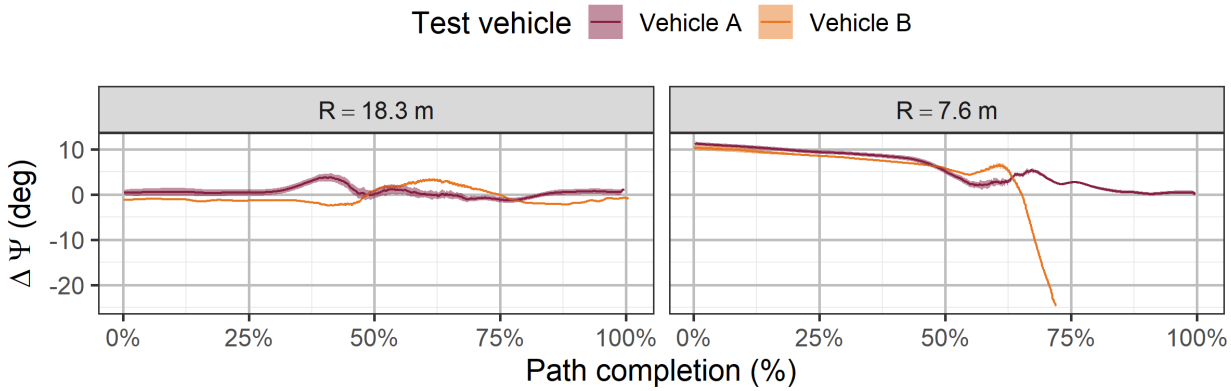

Figure 50. Ensemble average ΔΨ vs. $TC_{\%}$ for the *R* = 18.3 m (left) and *R* = 7.6 m (right) transient turns beginning at v_{start} = 11.2 m/s (S3.2, non-disturbance, both vehicles)

4.4 Traffic Circle Maneuvers

4.4.1 Scenario 4.0

This scenario tested the vehicle's response to a steady-state yaw for both left and right turn directions. Figure 51 shows the trajectory of the circle maneuver that began from rest, accelerated to a target speed, and held this speed constant. Like the intersection maneuvers, Vehicle A initially cut into the turn, creating a lateral offset of approximately 0.25 m before holding this lateral offset approximately constant. Likewise, Vehicle B began steering late, driving the vehicle up to 0.3 meters outside of the turn before steering back into the turn and correcting itself. Figure 52 and Figure 53 reaffirm these observations by plotting the ΔY_{offset} and ΔΨ behavior of both vehicles. Both vehicles exhibited the same respective behavior for the left and right turns, suggesting that the path deviations were due to the underlying control algorithm and not localization input errors.

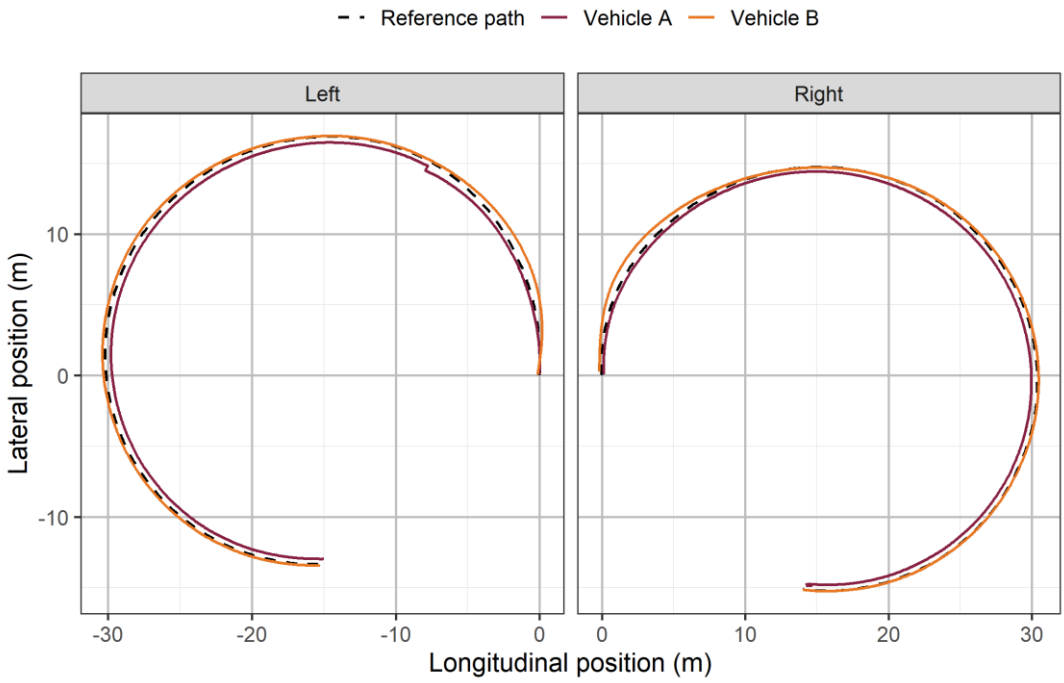

Figure 51. Trajectory plots for the traffic circle DVs in both turn directions (S4.0, non-disturbance, both vehicles). The dashed line represents the reference path

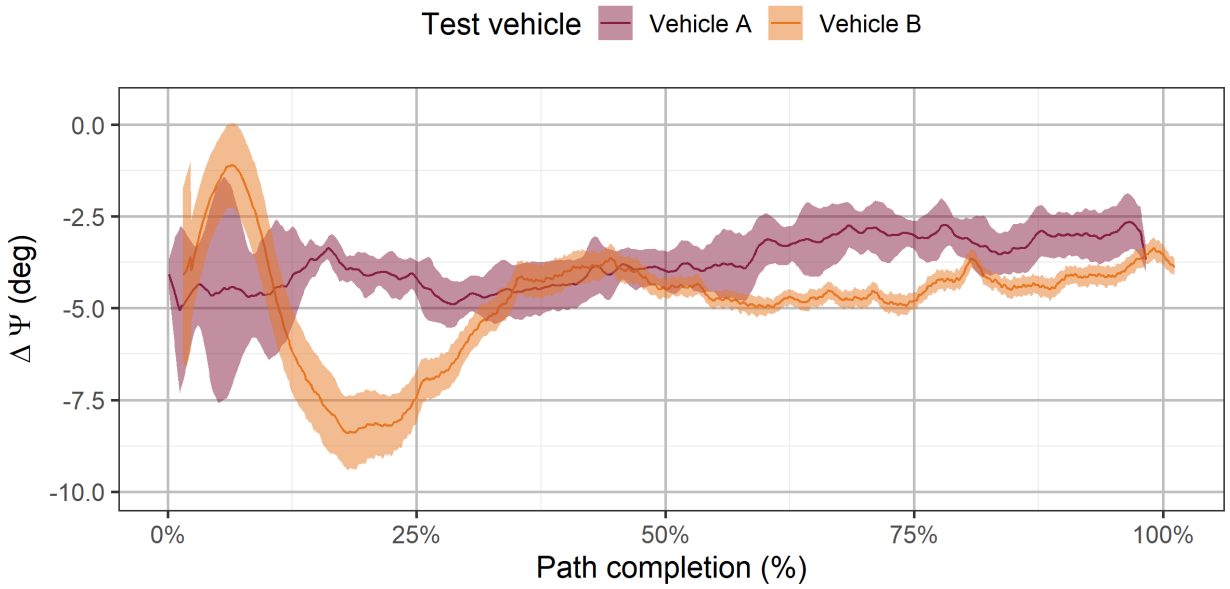

Figure 52. Ensemble average ΔΨ vs. $TC_{\%}$ for the right turn traffic circle DV (S4.0, non-disturbance, both vehicles)

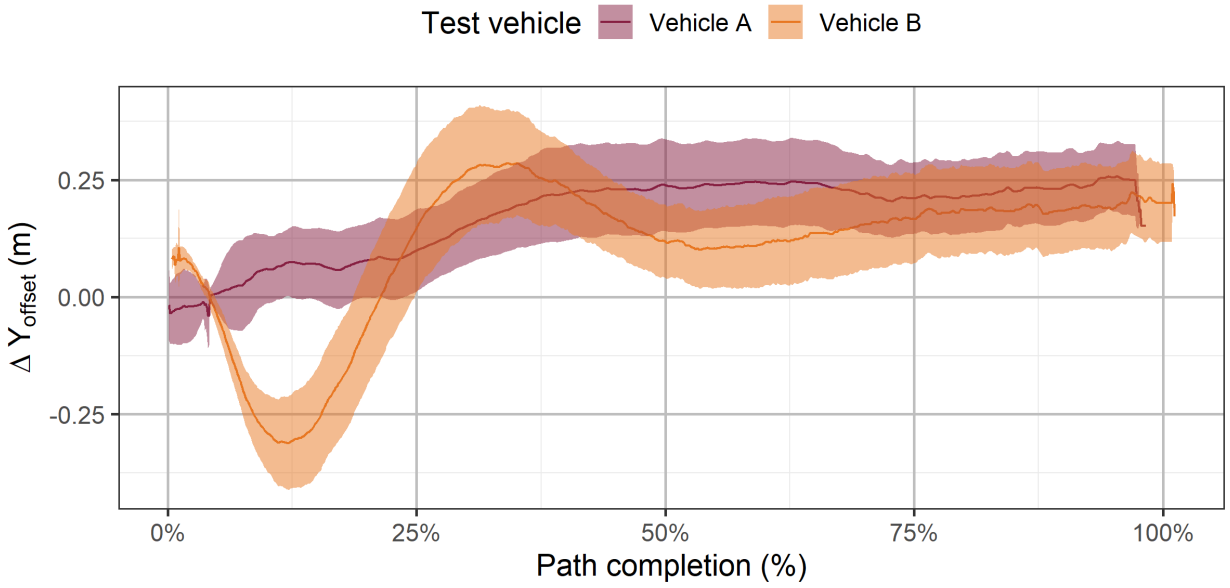

Figure 53. Ensemble average ΔY_{offset} vs. $TC_{\%}$ for the right turn traffic circle DV (S4.0, non-disturbance, both vehicles)

Figure 54 describes the longitudinal control behavior for the right turn DV. Like the previous longitudinal epochs, both vehicles lagged in the throttle tip-in during the initial acceleration portion before slightly overshooting the target longitudinal acceleration to catch up.

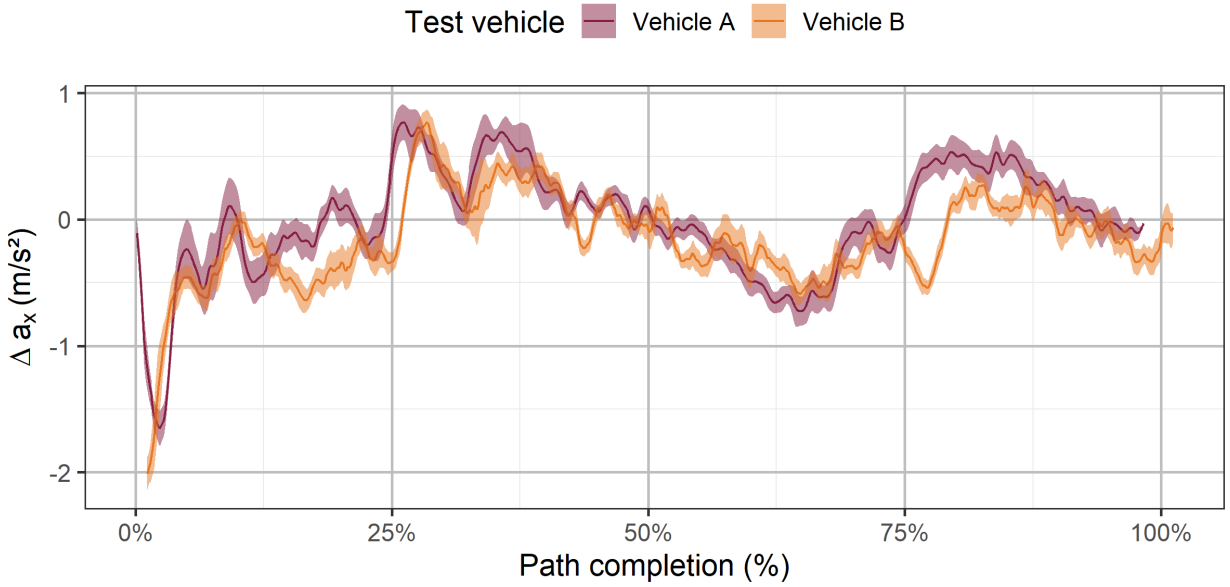

Figure 54. Ensemble average Δa_x vs. $TC_{\%}$ for the right turn traffic circle DV (S4.0, non-disturbance, both vehicles)

4.4.2 Scenario 4.1

Figure 55 shows the trajectory of the circle maneuver that began from rest, accelerated to a target speed, and conducted a lane change while holding its speed constant. This scenario tested the vehicle's response to a lane change and thus a change in the lateral acceleration while simultaneously cornering for both left and right turns. Both vehicles followed a similar lag in the throttle tip-in as the other longitudinal acceleration scenarios, as seen in Figure 56.

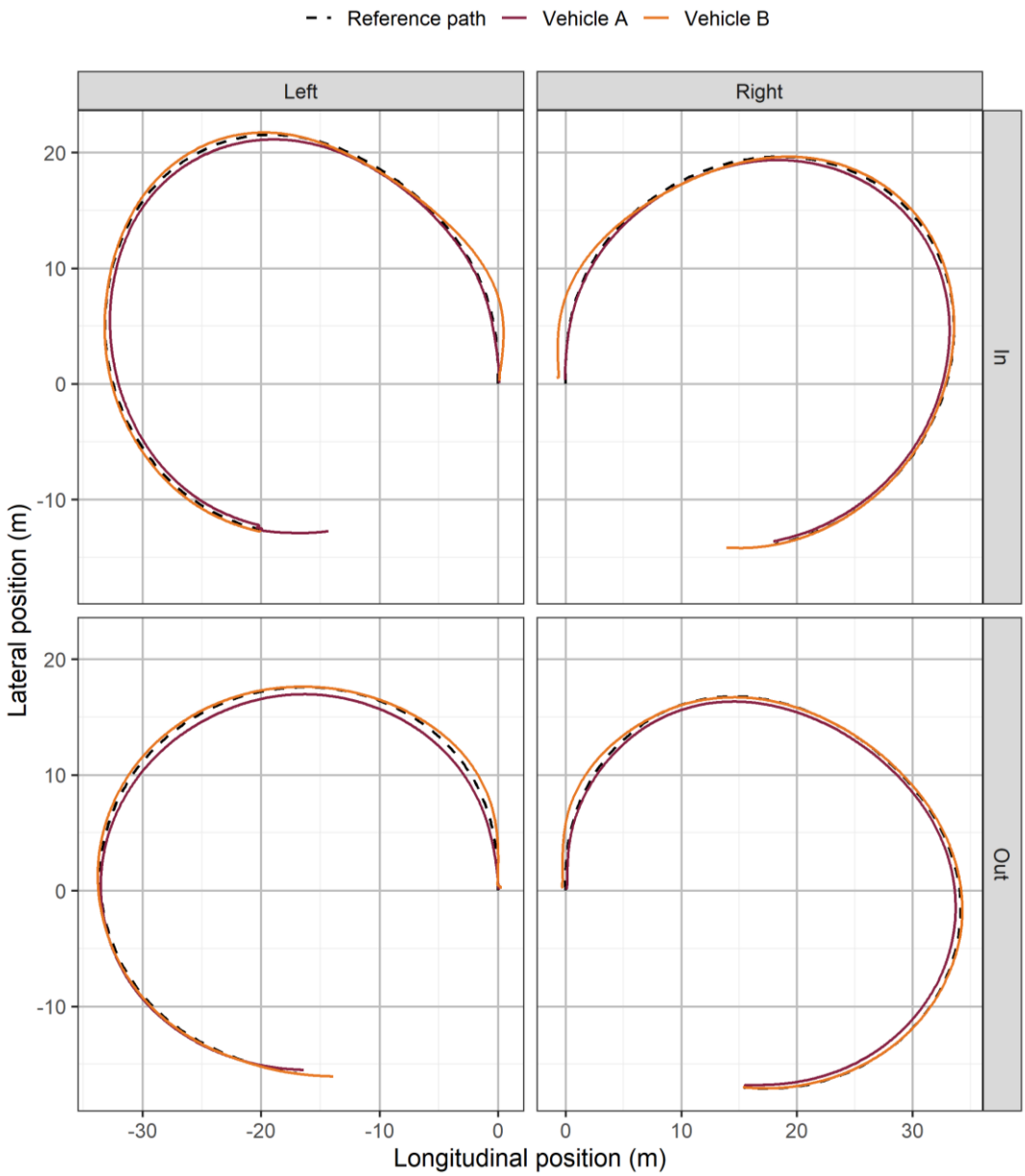

Figure 55. Trajectory plots for the traffic circle lane change DVs in both turn (left/right) and lane change (in/out) directions (S4.1, non-disturbance, both vehicles). The dashed line represents the reference path

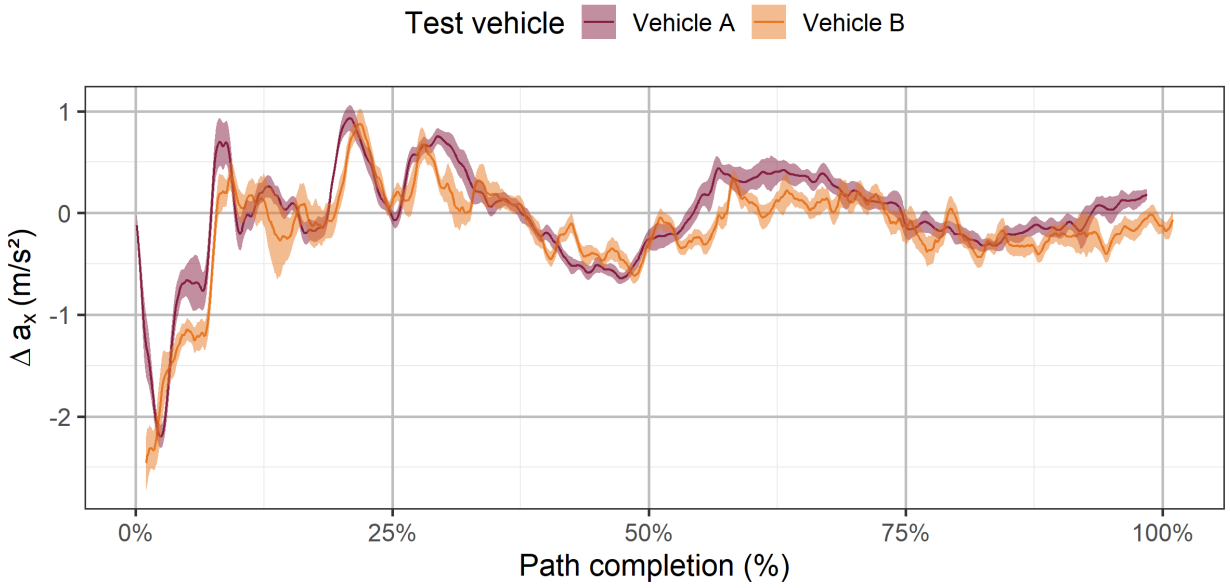

Figure 56. Ensemble average Δa_x vs. $TC_{\%}$ for the right turn, lane change out traffic circle DV (S4.1, non-disturbance, both vehicles)

The response of Vehicle B remained mostly consistent with Scenario 4.0 despite the lane change; the only difference was that Vehicle B had a larger initial lateral offset before the steering correction. Figure 57 shows the maximum lateral offset of each DV $\pm 2\sigma$. When comparing the turning direction, Vehicle B incurred larger lateral error for left turns, indicating there may be a bias in the lateral motion controller. When comparing the lateral offset due to lane change direction, the inner lane change exhibited a larger lateral offset; this possibly occurred because an inner lane change at a constant speed increases the lateral acceleration experienced by the vehicle.

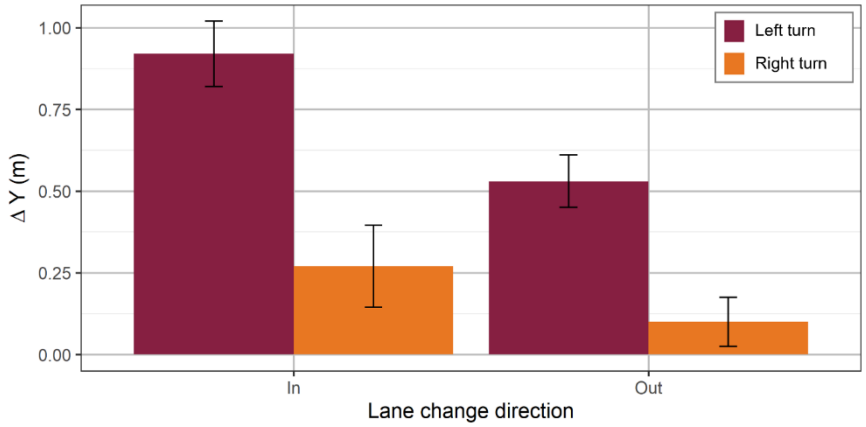

Figure 57. Comparison of the average ΔY for each turn and lane change direction (S4.1, non-disturbance, Vehicle B)

In the other scenarios that test cornering, Vehicle A consistently cut into the turn relative to the reference path throughout the cornering maneuver, but for the left turn and outer lane change DV, the vehicle laterally drifted outside the reference path by up to 0.75 meters before a final correction at the end of the maneuver. Figure 58 illustrates this trend for the left turn lane changes by showing the differing ΔY behavior between lane change directions despite similar ΔΨ traces.

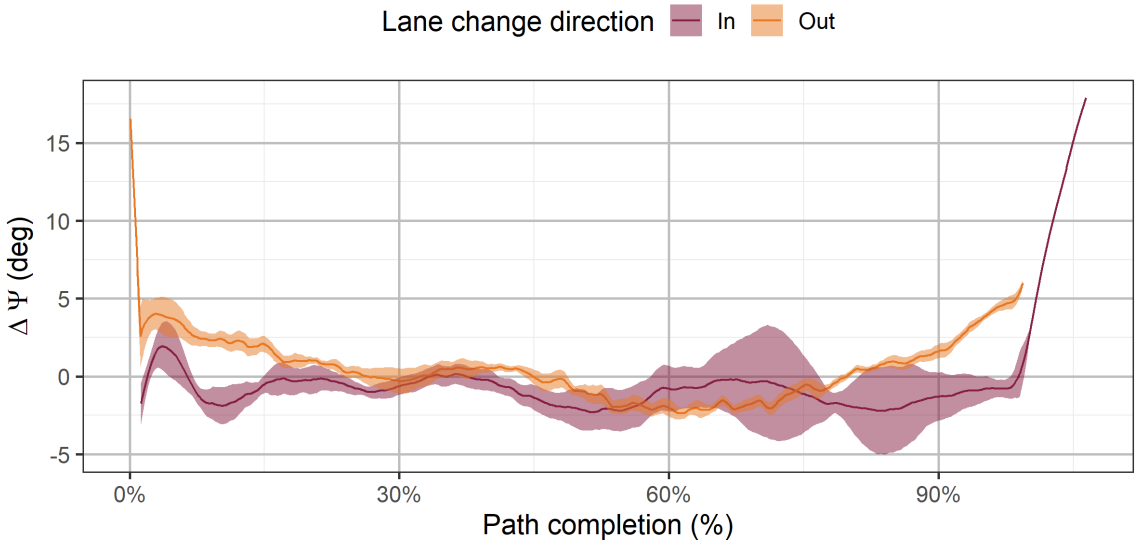

Figure 58. Ensemble average ΔΨ vs. TC$_{\%}$ response due to the lane change direction for the left turn traffic circle DV (S4.1, non-disturbance, Vehicle A)

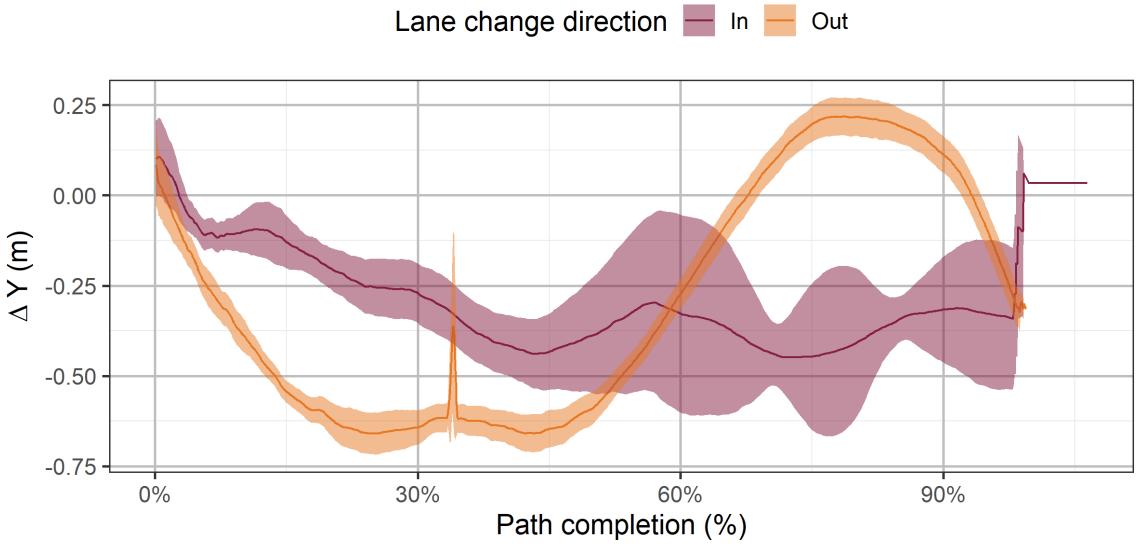

Figure 59. Ensemble average ΔY vs. TC$_{\%}$ response due to the lane change direction for the left turn traffic circle DV (S4.1, non-disturbance, Vehicle A)

4.5 Slalom Maneuver

4.5.1 Scenario 5.0

The slalom maneuver provided information on each system's response during transient lateral behavior. Figure 60 shows the trajectories for both vehicles, and Table 20 provides a summary of the primary metric statistics for the slalom maneuver. The previously explored trends continued to hold during the slalom maneuver; Vehicle A continued to cut the corner and effectively increase the radius of curvature, and Vehicle B continued to lag on the initial turn in and then overshoot. Investigating the RMS and absolute maximum ΔY for each target speed level indicated that higher speeds increased the magnitude of the path deviation for both test vehicles. Also, both vehicles produced nearly identical RMS and absolute maximum ΔY values. Regarding the speed error relative to the reference path, Vehicle B exhibited a large increase in RMS absolute maximum Δv for the 17.9 m/s DV, but these values remained approximately constant for Vehicle A.

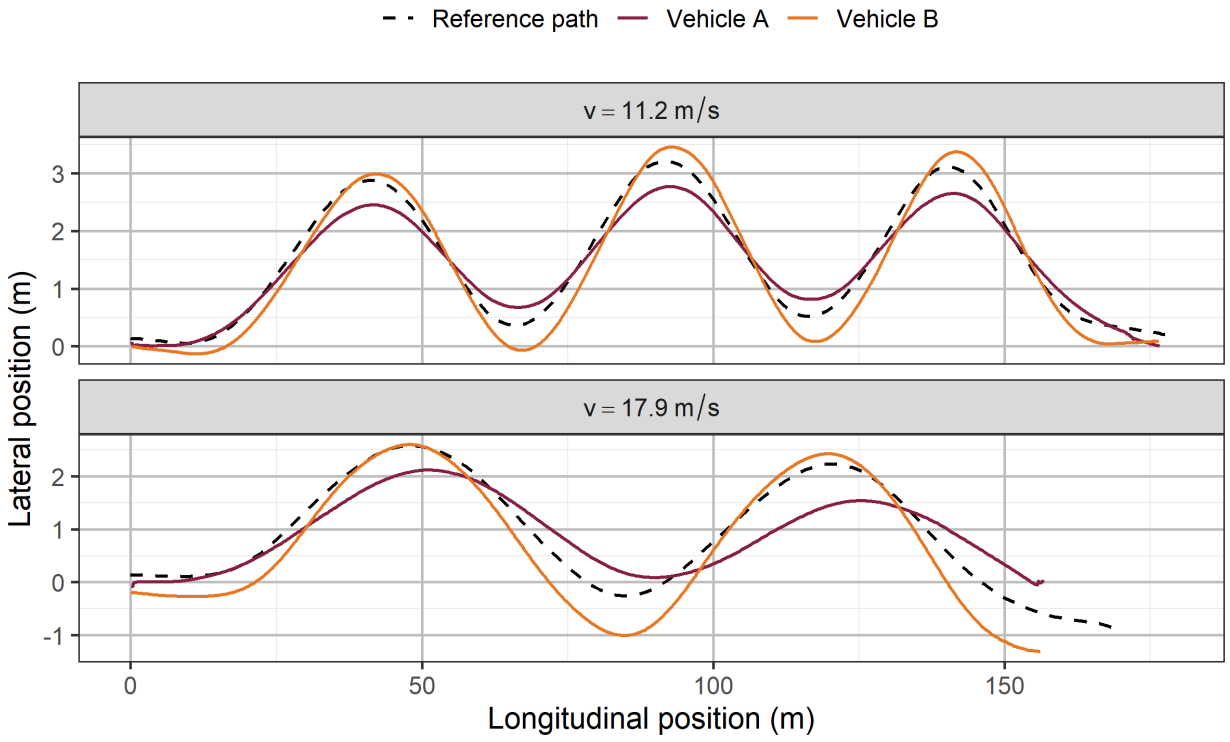

Figure 60. Trajectory plots for the v_{target} = 11.2 m/s (top) and 17.9 m/s (bottom) slalom at a_y = 2.9 m/s^2 (S5.0, non-disturbance, both vehicles). The dashed line represents the reference path

Table 20. Average of ΔY_{RMS}, ΔY_{absmax}, Δv_{avg}, and Δv_{absmax} across across all tests for both slalom DVs (S5.0, non-disturbance, both vehicles)

Test Vehicle	v_{target} (m/s)	ΔY_{RMS} (m)	ΔY_{absmax} (m)	Δv_{RMS} (m/s)	Δv_{absmax} (m/s)
A	11.2	0.25	0.48	0.24	0.84
B	11.2	0.27	0.50	0.27	0.70
A	17.9	0.45	0.85	0.36	0.79
B	17.9	0.44	0.84	0.33	0.69

Investigating the ΔY_{offset} traces in Figure 61 shows that at the 11.2 m/s DV, both vehicles stayed within 0.5 meters during the maneuver. However, the standard deviation of the response for Vehicle A grew throughout the maneuver, while Vehicle B remained consistent, implying that continued lateral motion decreased the accuracy of Vehicle A's response. The inverted sign and slight phase shift in the data occurred due to the contrasting behavior in the control algorithms. Regarding the signs, Vehicle A was to the left of the reference path when Vehicle B was to the right of the reference path and vice-versa. Regarding the phase shift, Vehicle A slightly led the reference path while Vehicle B lagged. In summary, the slalom maneuver was effective in highlighting the decreasing accuracy of Vehicle A due to repeated lateral motion.

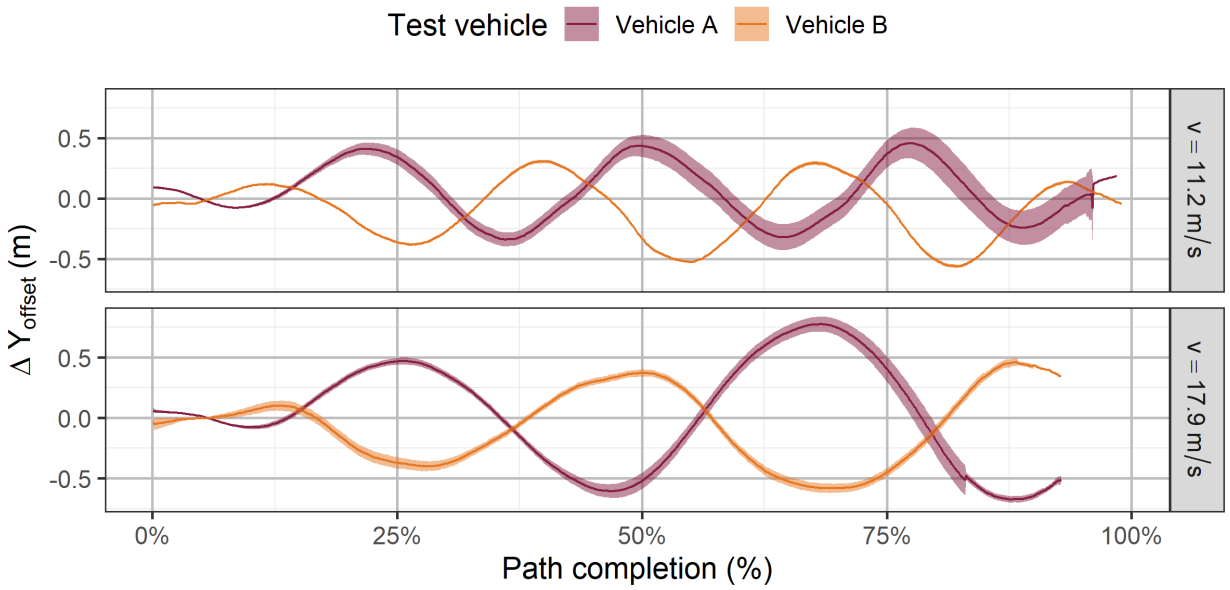

Figure 61. Ensemble average ΔY_{offset} vs. $TC_{\%}$ for the v_{target} = 11.2 m/s (top) and 17.9 m/s (bottom) slalom at a_y = 2.9 m/s^2 (S5.0, non-disturbance, both vehicles)

4.6 Disturbances

Various alterations to both the vehicle setup and roadway were introduced to assess the response of an ADS to outside disturbances during maneuver operation. Overall, only the road grade affected the response of both vehicles.

4.6.1 Tire Pressure

Lowering the tire pressures for the left-hand side and then the right-hand side from 35 psi to 20 psi showed no significant difference between the lateral and longitudinal control performance; this behavior was present for both test vehicles and all driving scenarios. For the Scenario 1.0 maneuver, Figure 62 indicates that the trials with reduced left-side tire pressure had a larger spread in ΔY data per test trial. Regarding the longitudinal behavior, Figure 63 demonstrates the minimal effect of reduced tire pressure on Δv. However, there was a slight reduction in stop point error and speed during the braking event, as shown in Figure 64. This reduction in stop error was possibly due to the increased tire drag of the lower pressure tires.

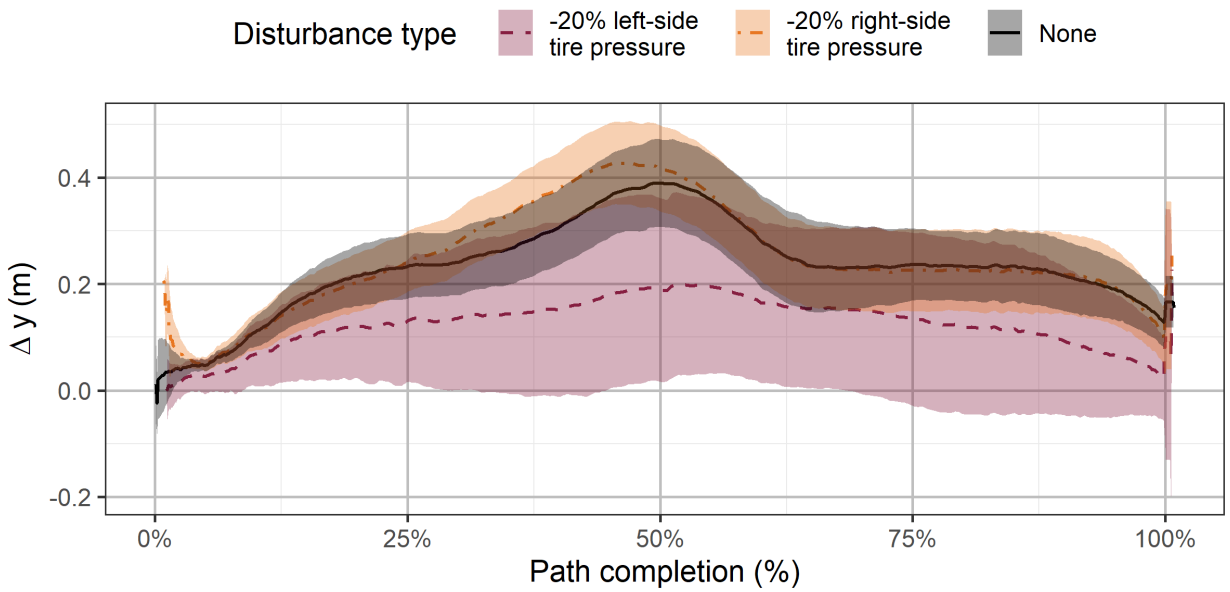

Figure 62. Ensemble average ΔY vs. TC% for the v_{target} = 17.9 m/s, a_x^+ = 2.5 m/s^2, a_x^- = 3.9 m/s^2 start-to-stop DV (S1.0, tire pressure disturbance, Vehicle A)

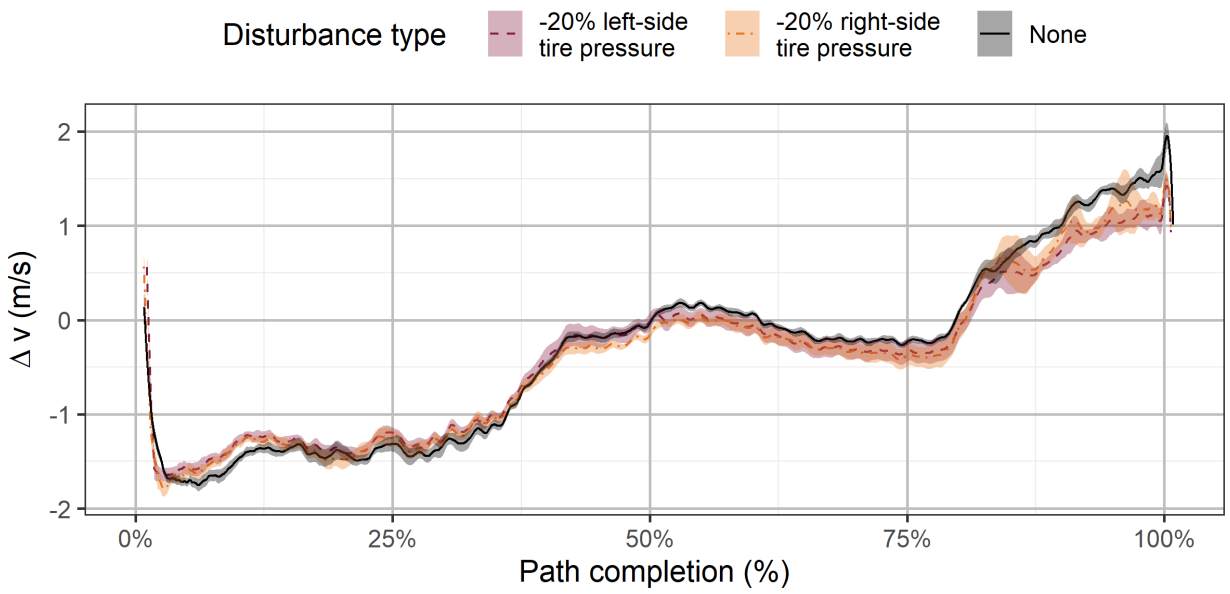

Figure 63. Ensemble average Δv vs. $TC_{\%}$ for the v_{target} = 17.9 m/s, a_x^+ = 2.5 m/s^2, a_x^- = 3.9 m/s^2 start-to-stop DV (S1.0, tire pressure disturbance, Vehicle A)

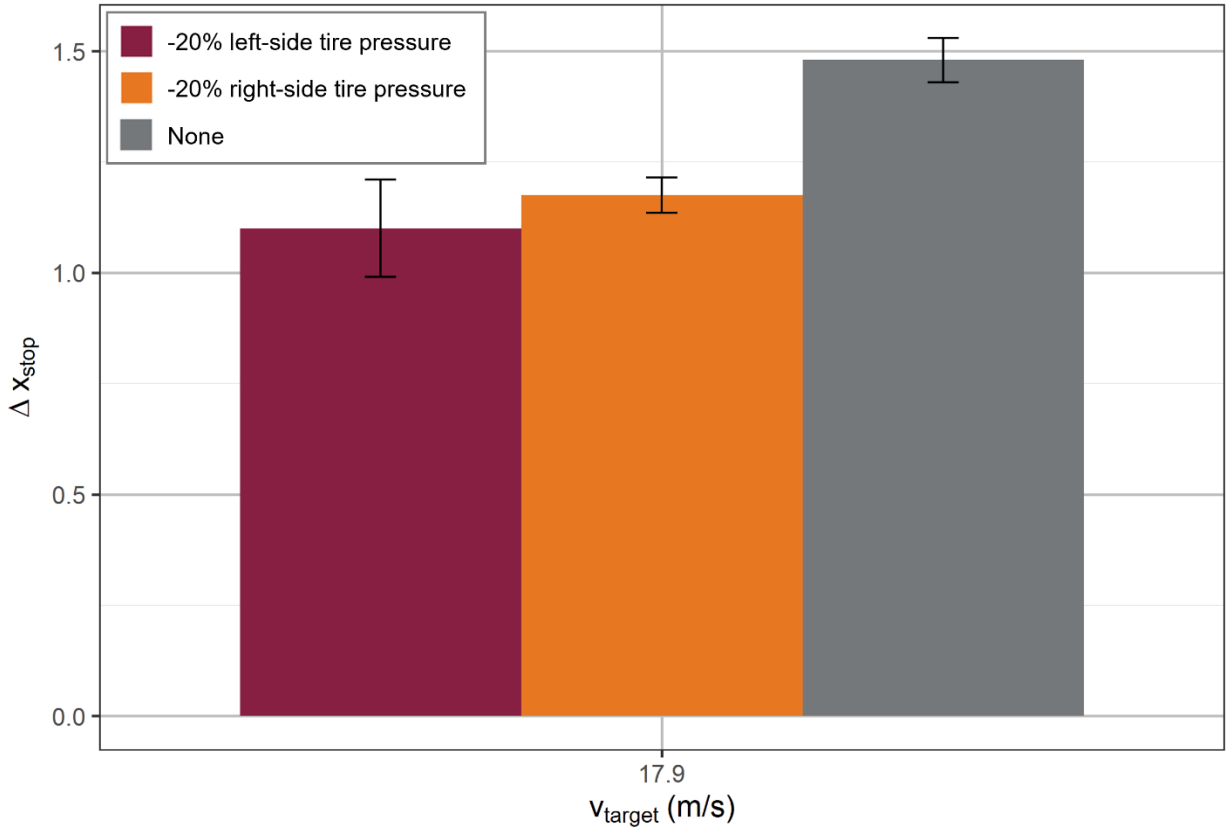

Figure 64. Comparison of the average Δx_{stop} across the tire pressure disturbances. DV: v_{target} = 17.9 m/s, a_x^+ = 2.5 m/s^2, a_x^- = 3.9 m/s^2 (S1.0, tire pressure disturbance, Vehicle A)

4.6.2 Grade

The 8% road grade disturbance was tested across the straight-line and slalom scenarios to capture the possible effects grade on both lateral and longitudinal control. Figure 65 investigates the longitudinal control by showing the Δv trace of Vehicle A for both the baseline and road grade tests. Despite the orientation of the road grade, all DVs demonstrated increased speed error (and thus stop point error) as braking magnitude increased. Also, all road grade tests exhibited similar throttle and braking actuation lag; the only difference was a relatively constant velocity offset that was most noticeable during the points of the test where the system was not transitioning between phases. In fact, the 8% downhill grade caused the test vehicle to overshoot the target velocity by 0.63 m/s on average (±0.11), while the 8% uphill grade caused the vehicle to undershoot the target velocity by 0.61 m/s on average (±0.09). Most notably, the ADS was able to match the reference speed profile during the constant speed phase of the uphill road grade tests, but before the braking phase began, the system reduced its speed by up to 0.74 m/s, indicating that its v_{target} setpoint may have been offset by a small value.

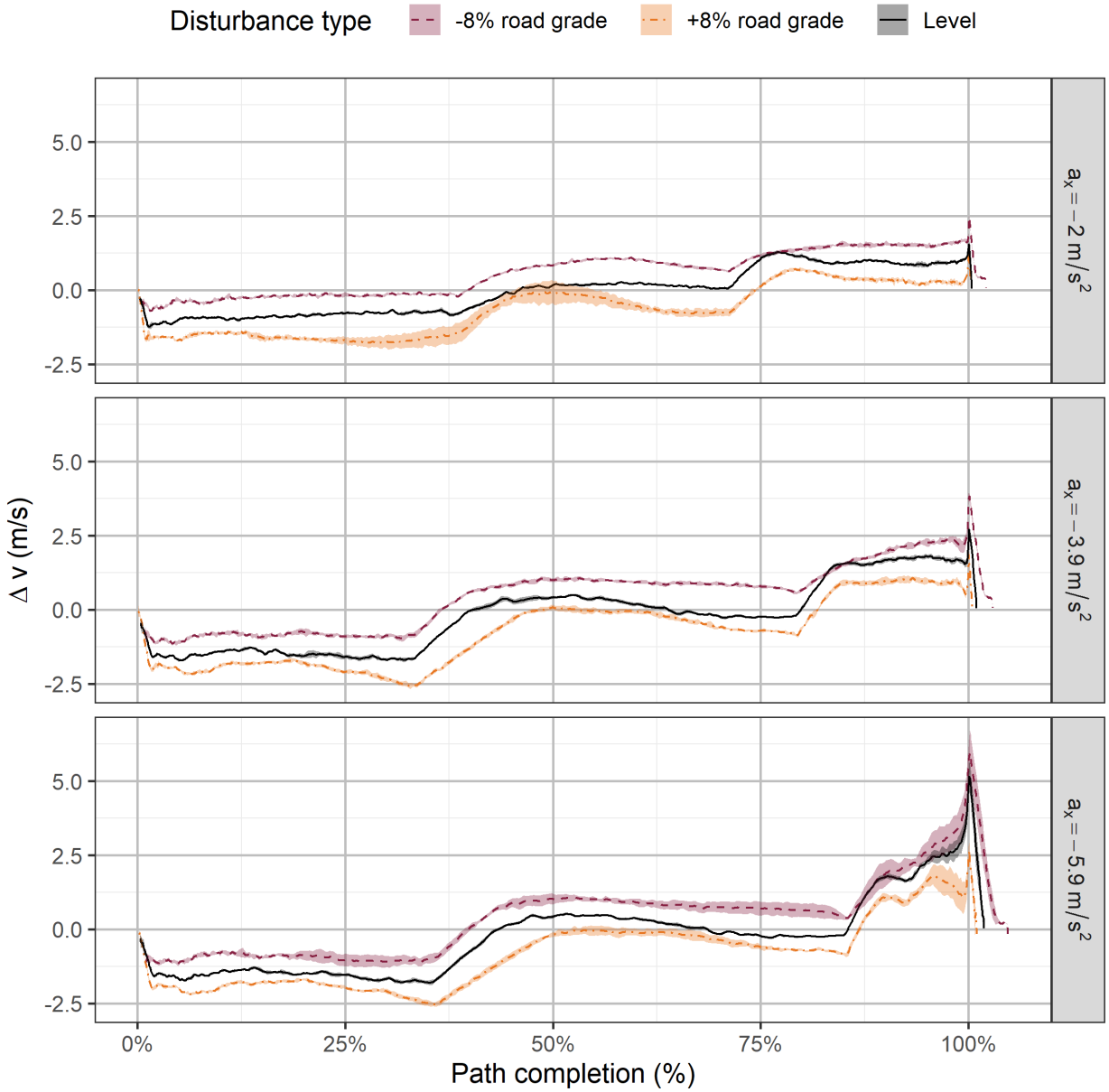

Figure 65. Ensemble average Δ*v* vs. TC$_{\%}$ for the v_{target} = 17.9 m/s DV across all braking and road grade DVs (S1.0, road grade disturbance, Vehicle A)

Figure 66 shows the effect of road grade on the stop error for the straight-line scenarios with a target speed of 17.9 m/s. For the uphill grade, the stop error reduced to no greater than 1.5 meters because the vehicle was travelling at a lower speed. For the downhill grade, the stop error drastically increased to at least 5 meters, and the accuracy of the stop error decreased because of the increased travel speed in addition to the lag in brake actuation, as seen in the sharp spike in the downhill grade data from Figure 65.

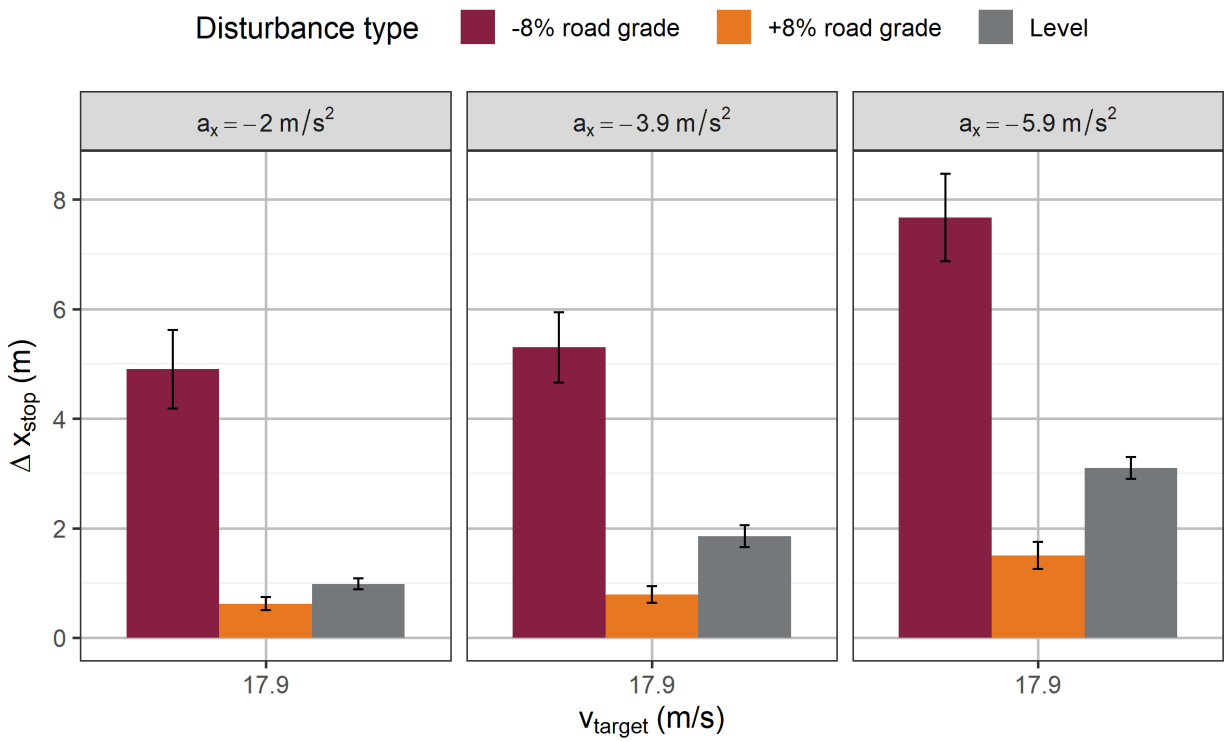

Figure 66. Comparison of the average Δx_{stop} across the road grade disturbances. DVs: v_{target} = 17.9 m/s, a_x^- = 2.0, 3.9, 5.9 m/s^2 (S1.0, road grade disturbance, Vehicle A)

The slalom scenario presented similar trends in speed deviations for both test vehicles. Table 21 summarizes the statistics of the primary control metrics, and Figure 67 and Figure 68 give the trajectory and ΔY plots, respectively, for Vehicle A. The uphill disturbance showed similar overall behavior as the non-disturbance slalom at both tested speeds. However, the downhill slalom conducted at 11.2 m/s entered an unstable condition that resulted in a maximum ΔY of over 4 meters and a maximum ΔΨ of about 25 deg. At 17.9 m/s, the vehicle showed increased lateral deviation due to the higher speed induced by the downhill grade but never entered a fully unstable oscillation, possibly because the test track could only fit two slalom periods at 17.9 m/s instead of three. Aside from the unstable yaw behavior, the error in the primary metrics increased as the slalom speed increased.

Table 21. Average of ΔY_{RMS}, ΔY_{absmax}, $\Delta \Psi_{RMS}$, $\Delta \Psi_{absmax}$, Δv_{avg}, and Δv_{absmax} across all slalom tests for each DV (S5.0, road grade disturbance, Vehicle A)

v_{target}	Grade	ΔY_{RMS} (m)	ΔY_{absmax} (m)	$\Delta \Psi_{RMS}$ (deg)	$\Delta \Psi_{absmax}$ (deg)	Δv_{avg} (m/s)	Δv_{absmax} (m/s)
11.2	Level	0.25	0.48	1.8	3.6	-0.2	0.8
11.2	-8%	1.49	4.05	7.8	25.3	0.6	1.7
11.2	+8%	0.32	0.54	2.6	8.5	-0.7	-1.0
17.9	Level	0.45	0.85	2.2	4.2	-0.2	0.8
17.9	-8%	0.73	1.46	3.5	8.4	0.8	1.9
17.9	+8%	0.57	1.11	2.7	5.7	-0.5	-1.3

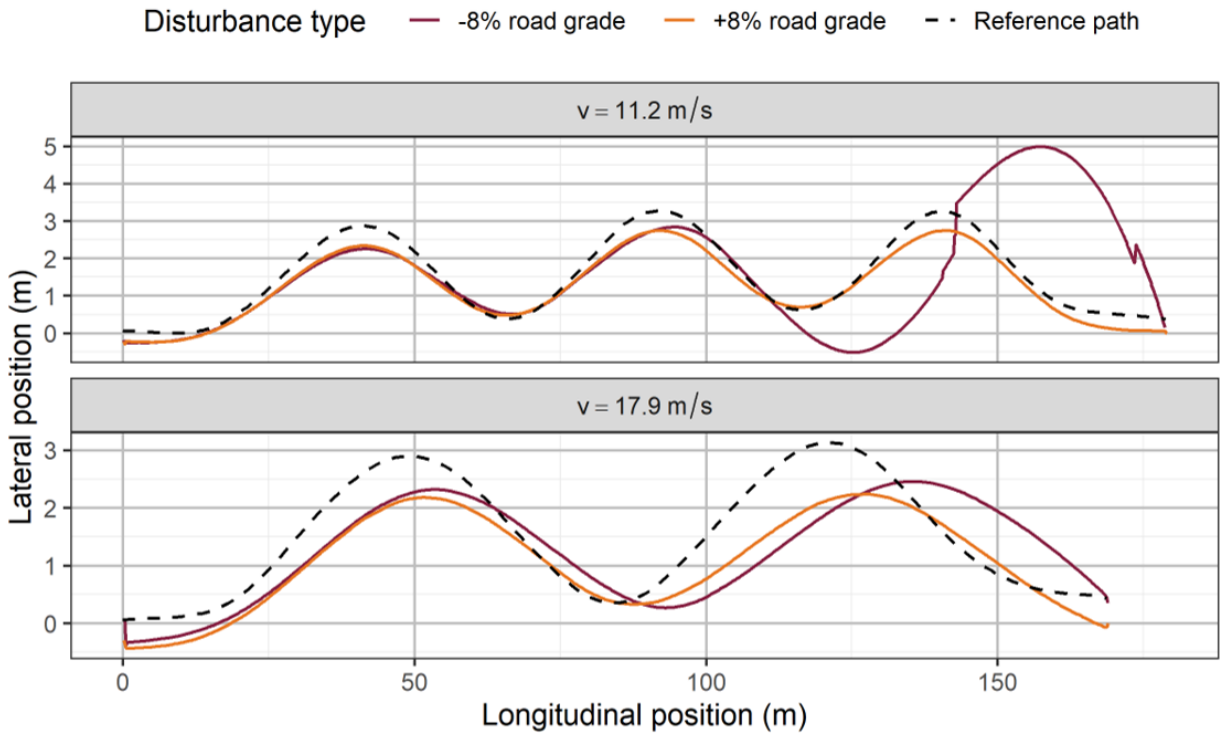

Figure 67. Trajectory plots for the v_{target} = 11.2 m/s (top) and 17.9 m/s (bottom) road grade slalom at a_y = 2.9 m/s^2 (S5.0, road grade disturbance, Vehicle A). The dashed line represents the reference path

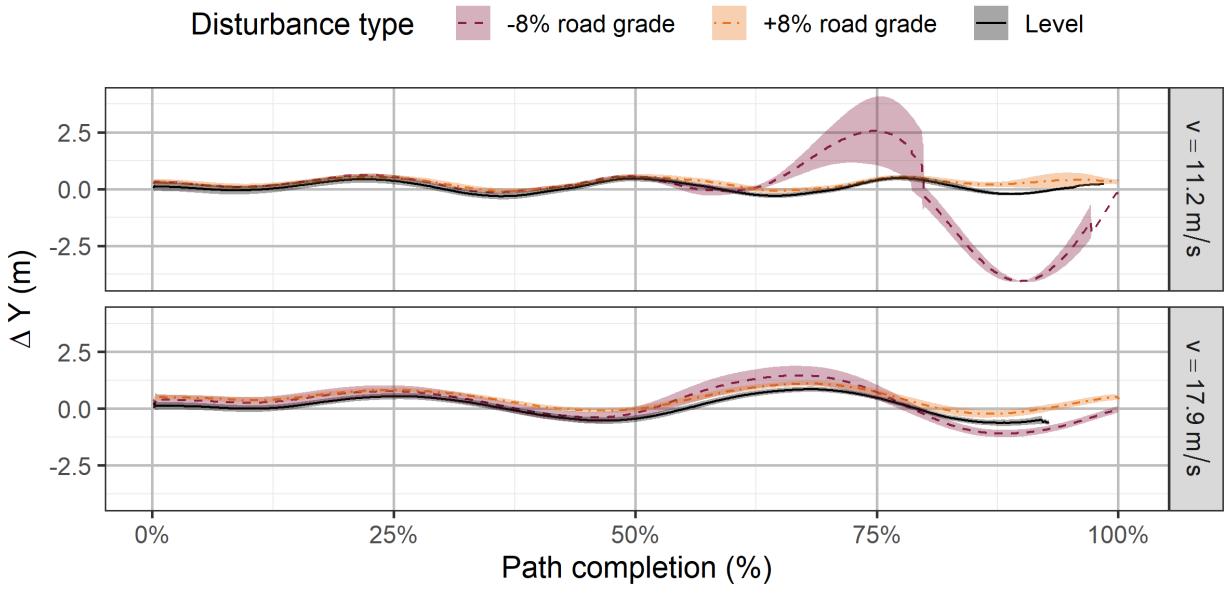

Figure 68. Ensemble average ΔY vs. $TC_{\%}$ for the v_{target} = 11.2 m/s (top) and 17.9 m/s (bottom) slalom at a_y = 2.9 m/s^2 (S5.0, road grade disturbance, Vehicle A)

The grade disturbances also affected Vehicle B, causing it to travel 1 m/s above and 1.1 m/s below the reference velocity profile for the downhill and uphill grades, respectively. At both design speeds, Vehicle B followed the path more closely than Vehicle A based on the aggregate statistics (Table 22) and trajectory plots (Figure 69), but the effect of the road grade on the primary metrics also increased for the higher slalom speed. In addition, Vehicle B also showed more precise ΔY behavior according to Figure 70, but it should be noted that the large uncertainty in the uphill slalom at 17.9 m/s is due to one outlier test trial that exhibited increased corner cutting.

Table 22. Average of ΔY_{RMS}, ΔY_{absmax}, $\Delta \Psi_{RMS}$, $\Delta \Psi_{absmax}$, Δv_{avg}, and Δv_{absmax} across all slalom tests for each DV (S5.0, road grade disturbance, Vehicle B)

v_{target}	Grade	ΔY_{RMS} (m)	ΔY_{absmax} (m)	$\Delta \Psi_{RMS}$ (deg)	$\Delta \Psi_{absmax}$ (deg)	Δv_{avg} (m/s)	Δv_{absmax} (m/s)
11.2	Level	0.27	0.50	2.7	5.0	-0.2	0.7
11.2	-8%	0.24	0.52	1.3	2.7	0.9	1.8
11.2	+8%	0.36	0.65	1.3	2.9	-1.0	-1.3
17.9	Level	0.44	0.84	2.6	4.8	-0.4	2.1
17.9	-8%	0.43	0.78	2.3	4.3	1.1	1.9
17.9	+8%	0.42	0.80	1.7	3.1	-1.2	-1.8

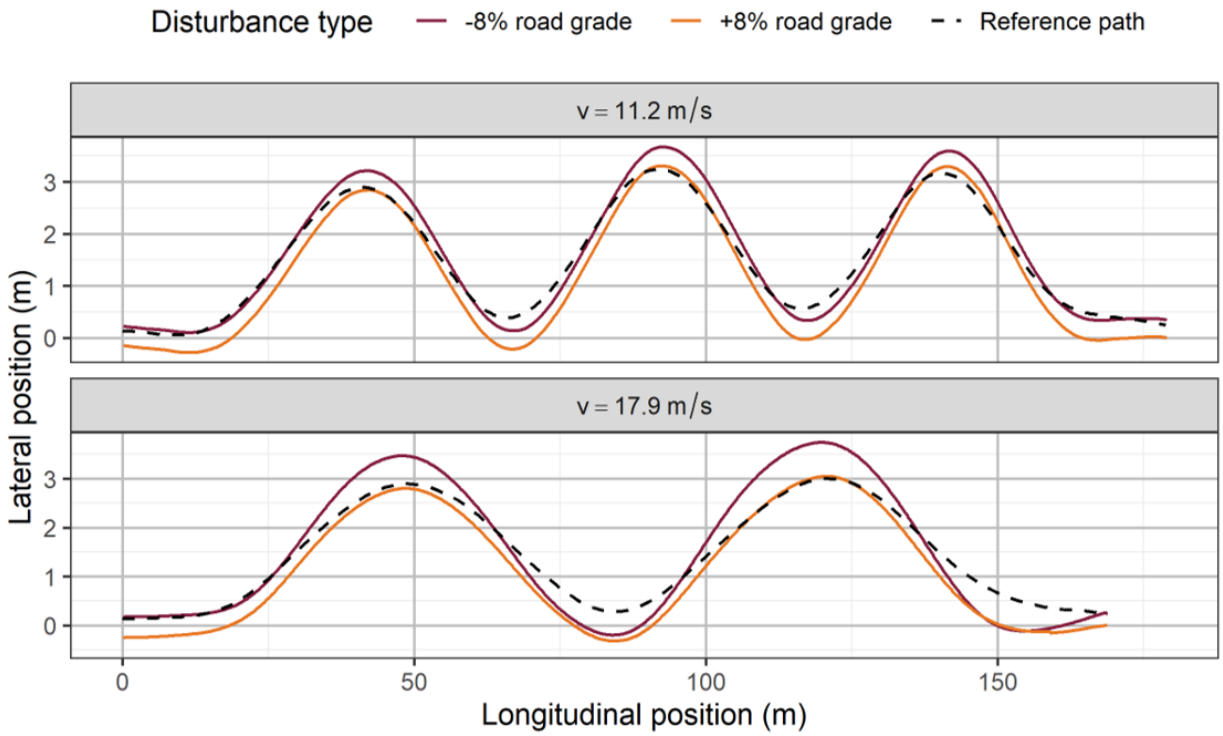

Figure 69. Trajectory plots for the v_{target} = 11.2 m/s (top) and 17.9 m/s (bottom) road grade slalom at a_y = 2.9 m/s^2 (S5.0, road grade disturbance, Vehicle B). The dashed line represents the reference path

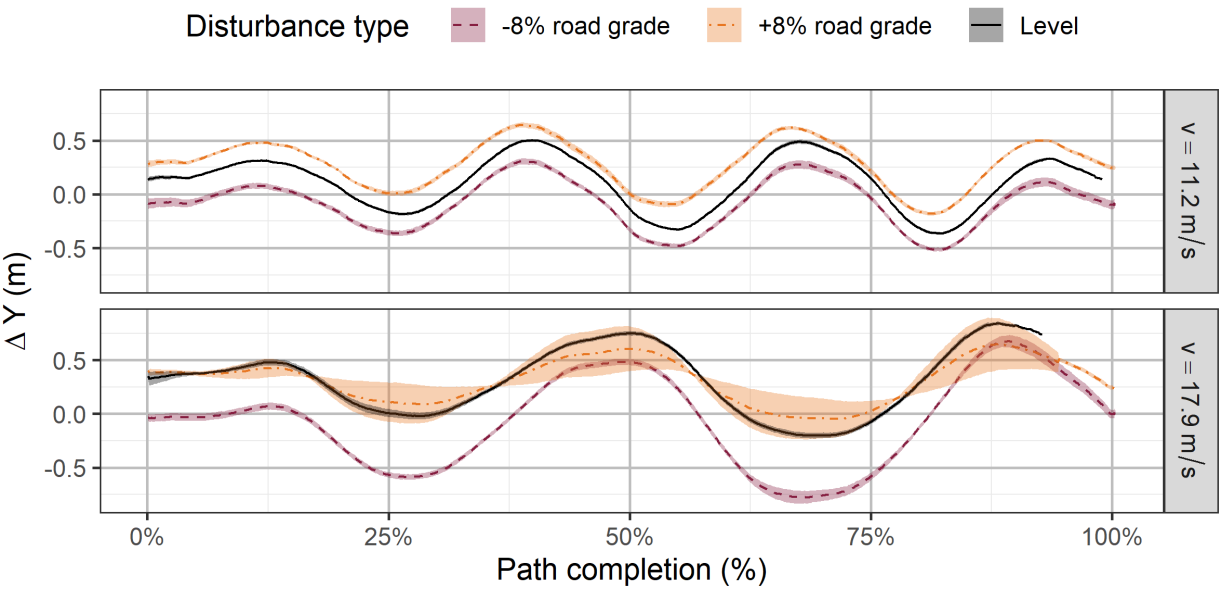

Figure 70. Ensemble average ΔY vs. TC$_{\%}$ for the v_{target} = 11.2 m/s (top) and 17.9 m/s (bottom) slalom at a_y = 2.9 m/s^2 (S5.0, road grade disturbance, Vehicle B)

Although the response of Vehicle B was more precise aside from the one outlier test trial, minor localization errors due to converting to a local coordinate system introduced positional

biases that shifted entire testing groups laterally, reducing the accuracy of the response. Figure 71 confirmed this observation when plotting ΔY_{offset}, which collapsed the paths onto each other and removed the lateral bias.

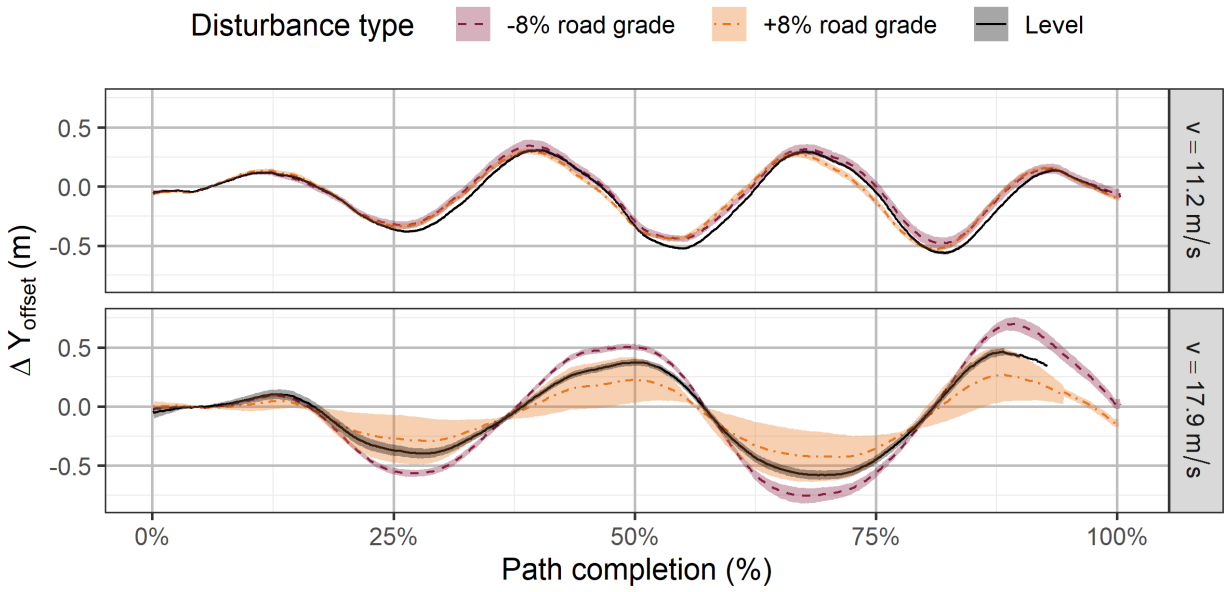

Figure 71. Ensemble average ΔY_{offset} vs. $TC_{\%}$ for the v_{target} = 11.2 m/s (top) and 17.9 m/s (bottom) slalom at a_y = 2.9 m/s^2 (S5.0, road grade disturbance, Vehicle B)

4.6.3 Bumps

Like the tire pressure disturbances, the bumps did not have a pronounced effect on the path-following performance for either of the test vehicles. This was possibly because both vehicles were midsized sedans with independent suspensions. Table 23 displays the RMS ΔY and mean Δv for both the baseline cornering scenarios (Scenario 3.0 and 4.0) and bump disturbances for Vehicle A. According to the tables, there was no significant nor practical difference in performance for Vehicle A. This was confirmed in Figure 72 and Figure 73, which shows no major differences in yaw rate error while containing a noticeable impulse.

Table 23. Average of ΔY_{avg}, ΔY_{RMS}, and Δv_{avg} across all tests for the constant speed turns (R = 18.3 m, a_y = 4.4 m/s^2) and right-turn traffic circle DVs (S3.0 vs. S4.0, bump disturbance, Vehicle A)

Scenario	Bump Placement	ΔY_{avg} (m)	ΔY_{RMS} (m)	Δv_{avg} (m/s)
3.0	None	-0.12	1.02	-0.37
3.0	End	-0.09	0.98	-0.36
3.0	Middle	-0.04	1.04	-0.33
4.0	None	0.35	0.36	-0.39
4.0	Double	0.34	0.35	-0.39

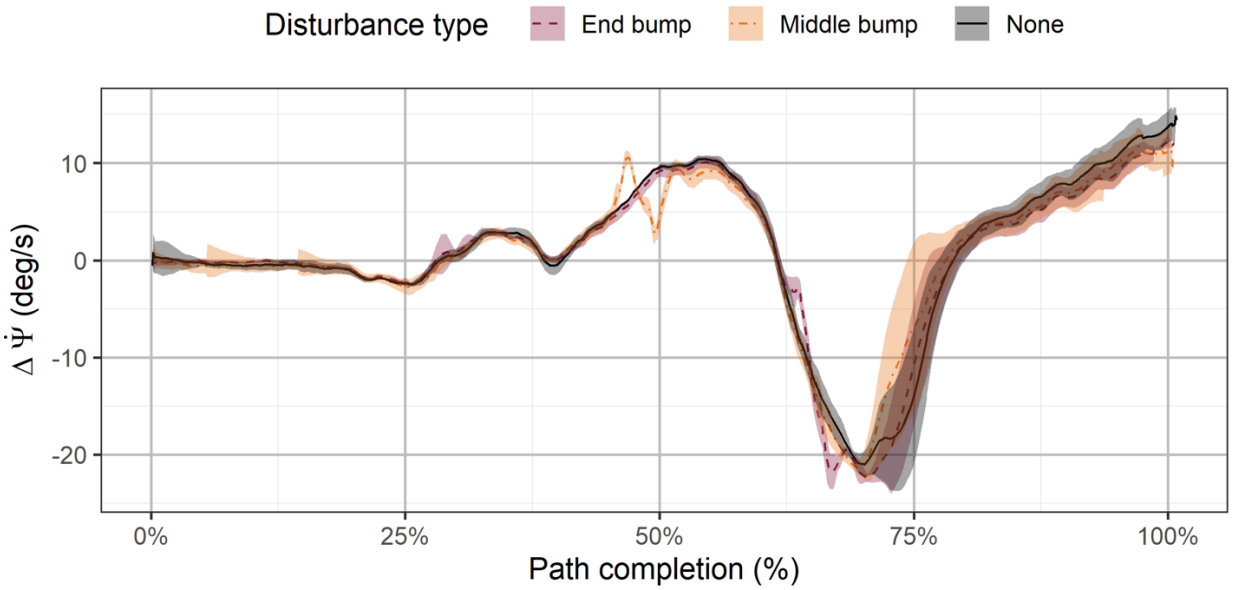

Figure 72. Ensemble average ΔΨ̇ vs. TC% for the constant speed turns (R = 18.3 m, a_y = 4.4 m/s^2) (S3. 0, bump disturbance, Vehicle A)

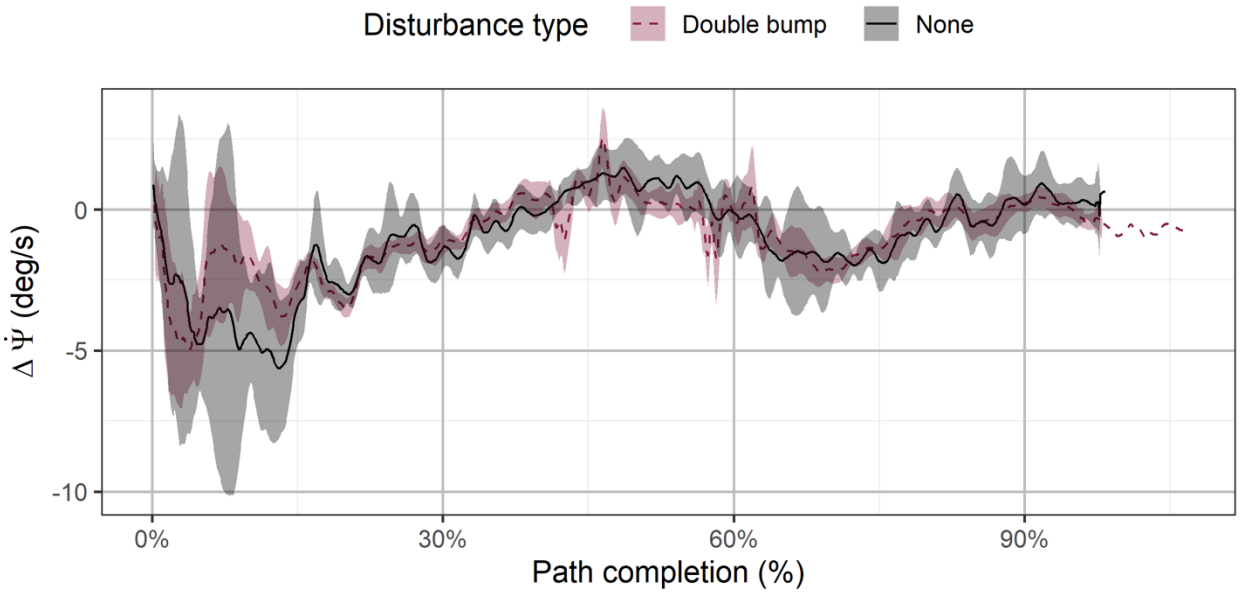

Figure 73. Ensemble average ΔΨ̇ vs. TC% for right-turn traffic circle maneuvers with bumps (S4.0, bump disturbance, Vehicle A)

However, Table 23 displays the RMS ΔY and mean Δv for Vehicle B, and the RMS ΔY of Scenario 3.0 contained the largest differences from the non-disturbance results. Plotting the ΔY trace in Figure 74 indicated that the lateral offset behavior differed before encountering the bump. These test trials were conducted on different days due to weather issues, so it is plausible

that continuing testing on a different day induced drifts in the inputs from IMU or DGPS. Regardless, Figure 75 demonstrates that the road bumps still did not influence the yaw rate behavior after encountering the bump because both disturbances align closely with each other.

Table 24. Average of ΔY_{avg}, ΔY_{RMS}, and Δv_{avg} across all tests for the constant speed turns (R = 18.3 m, a_y = 4.4 m/s^2) and right-turn traffic circle DVs (S3.0 vs. S4.0, bump disturbance, Vehicle B)

Scenario	Bump Placement	ΔY_{avg} (m)	ΔY_{RMS} (m)	Δv_{avg} (m/s)
3.0	None	0.1	0.1	-0.29
3.0	End	0.15	0.27	-0.31
3.0	Middle	0.14	0.28	-0.29
4.0	None	-0.13	0.2	-0.42
4.0	Double	-0.12	0.18	-0.45

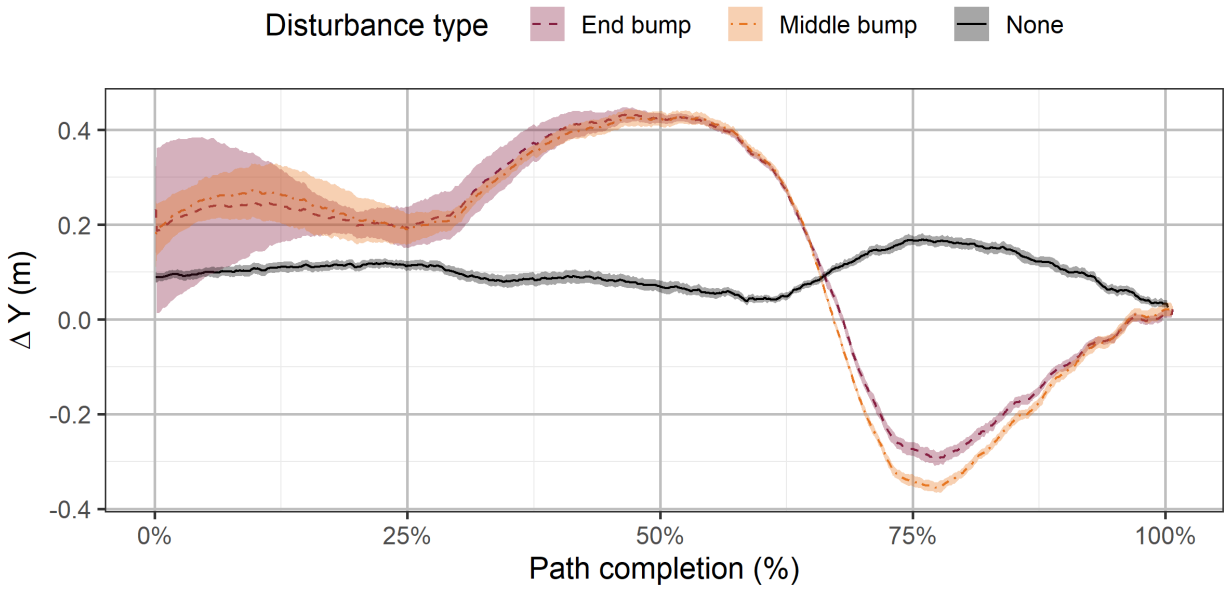

Figure 74. Ensemble average ΔY vs. TC$_{\%}$ for the R = 18.3 m constant speed turns at a_y = 4.4 m/s^2 (S3.0, bump disturbance, Vehicle B)

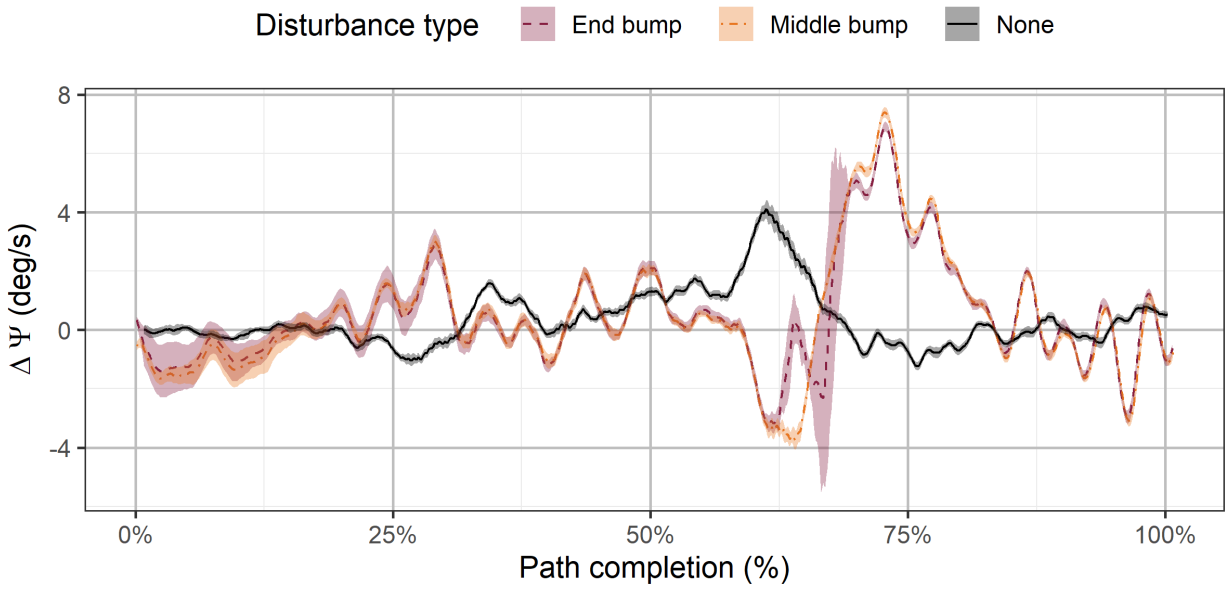

Figure 75. Ensemble average $\Delta\dot{\Psi}$ vs. $TC_{\%}$ for the R = 18.3 m constant speed turns at a_y = 4.4 m/s^2 (S3.0, bump disturbance, Vehicle B)

4.7 Synthetic Reference Path Effects

Because the method proposed in this project generated reference paths using two methods, the responses of the human DBE and synthetically derived reference paths via manually calculated waypoints were first compared to assess for possible differences that both methods may have introduced. Regarding longitudinal behavior, Figure 76 compares the two groups by assessing the average Δv and x_{stop} behavior for two Scenario 1.0 DVs: v_{target} = 11.2 and 17.9 m/s with acceleration targets of a_x^+ = 2.5 m/s^2 and a_x^- = 3.9 m/s^2. The acceleration and constant speed portions showed minimal differences in the average speed offset between groups. However, braking did show a consistent 0.5 m/s increase in the average speed offset for the synthetic path, and this trend held for the other braking magnitudes.

The slight speed overshoot during braking affected the stop errors of the synthetic reference paths (Figure 77). Because the synthetic paths exhibited the same throttle and brake actuation lag as the DBE paths, increased longitudinal acceleration error and jerk occurred during the transitional phases in the maneuver. Additionally, there was more oscillatory longitudinal acceleration during the braking phase. Figure 78 compares the longitudinal acceleration error of the two reference path groups and highlights the increased jerk for the synthetic tests.

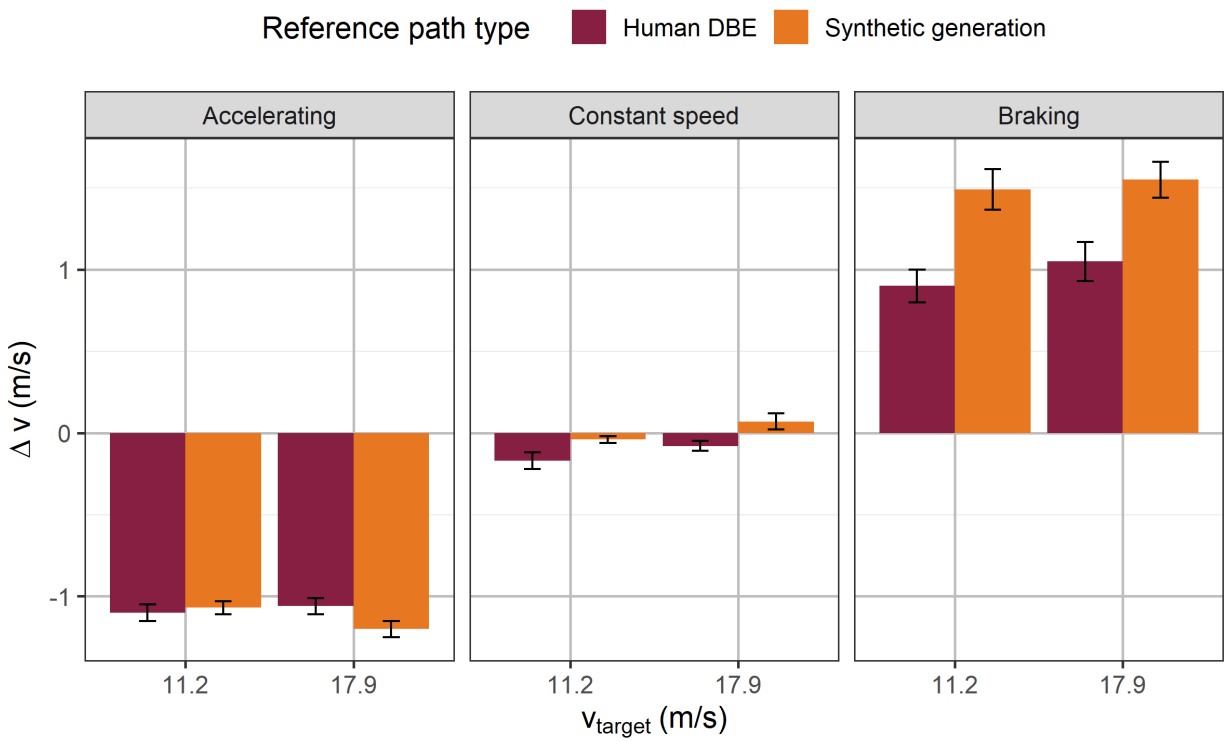

Figure 76. Comparison of the average Δv across the human DBE and synthetic reference paths. DVs: v_{target}= 11.2 and 17.9 m/s, a_x^- = 5.9 m/s^2 (S1.0, reference path comparison, Vehicle A)

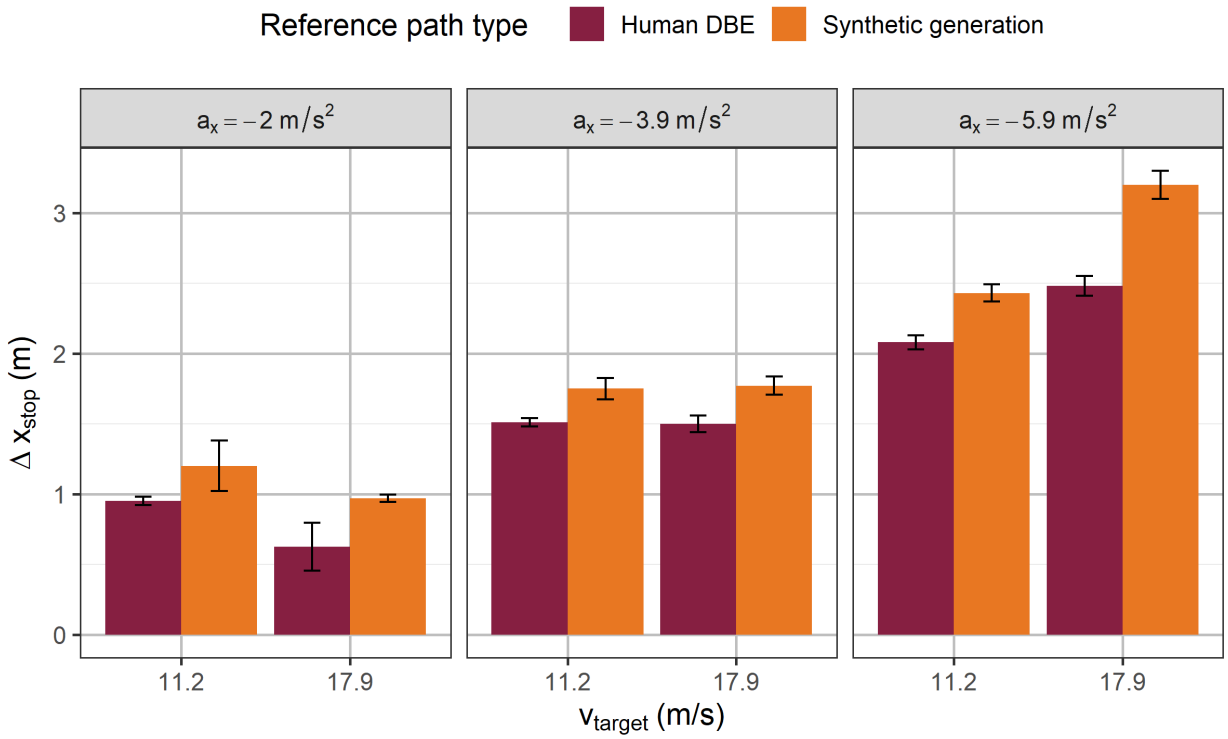

Figure 77. Comparison of the average Δx_{stop} across the human DBE and synthetic reference paths. DVs: v_{target}= 11.2 and 17.9 m/s, a_x^- = 2.0, 3.9, 5.9 m/s^2 (S1.0, reference path comparison, Vehicle A)

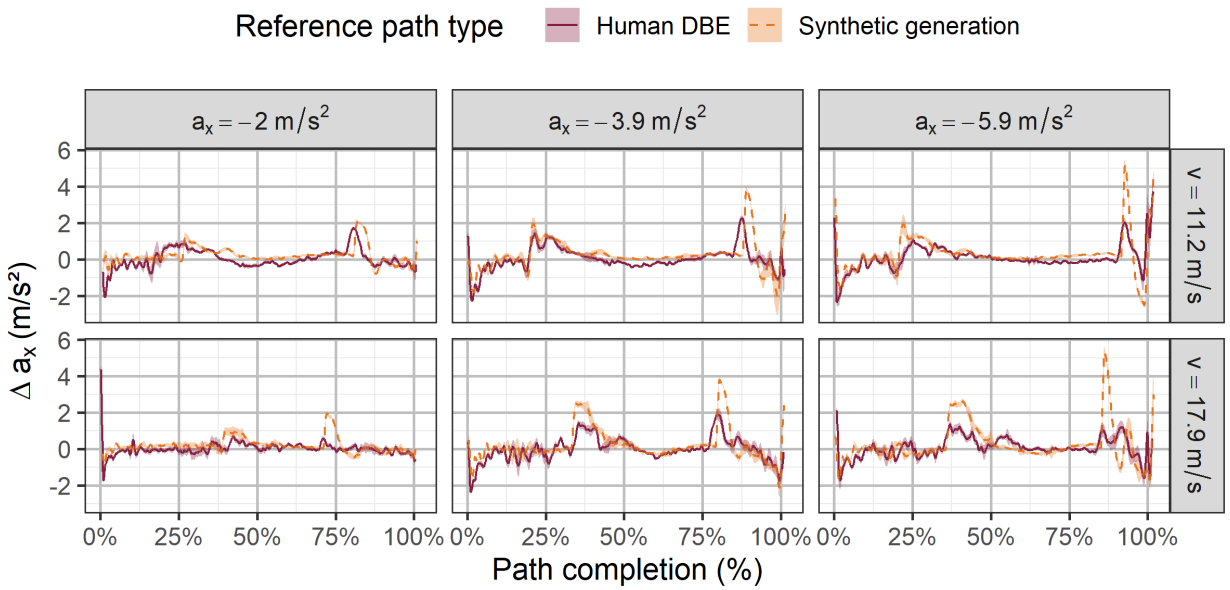

Figure 78. Ensemble average Δa_x vs. TC% for the v_{target} = 11.2 and 17.9 m/s, a_x^- = 3.9 m/s^2 start-to-stop DV (S1.0, refence path comparison, Vehicle A) |

In addition to Scenario 1.0, Scenario 4.0 was used to assess if the synthetic reference paths influenced the lateral offset or yaw offset behavior. Table 25 gives the primary metrics summary statistics, and Figure 79 shows the ΔY traces of both reference paths. Although the two reference path generation methods showed no major differences, the synthetic path was less accurate with a ΔY standard deviation of 0.31 meters, while the DBE reference path had a ΔY standard deviation of 0.12 meters.

Table 25. Average of ΔY_{RMS}, ΔY_{absmax}, $\Delta \Psi_{RMS}$, $\Delta \Psi_{absmax}$, and Δv_{avg} across all traffic circle tests for each DV (S4.0, reference path comparison, Vehicle A)

Turn Direction	Reference Path Type	ΔY_{RMS} (m)	ΔY_{absmax} (m)	$\Delta \Psi_{RMS}$ (deg)	$\Delta \Psi_{absmax}$ (deg)	Δv_{avg} (m/s)
Left	DBE	0.38	0.68	1.2	5.5	-0.4
Left	Synthetic	0.32	0.57	2.0	3.1	-0.4
Right	DBE	0.35	0.42	3.8	5.9	-0.4
Right	Synthetic	0.42	0.54	1.9	6.0	-0.4

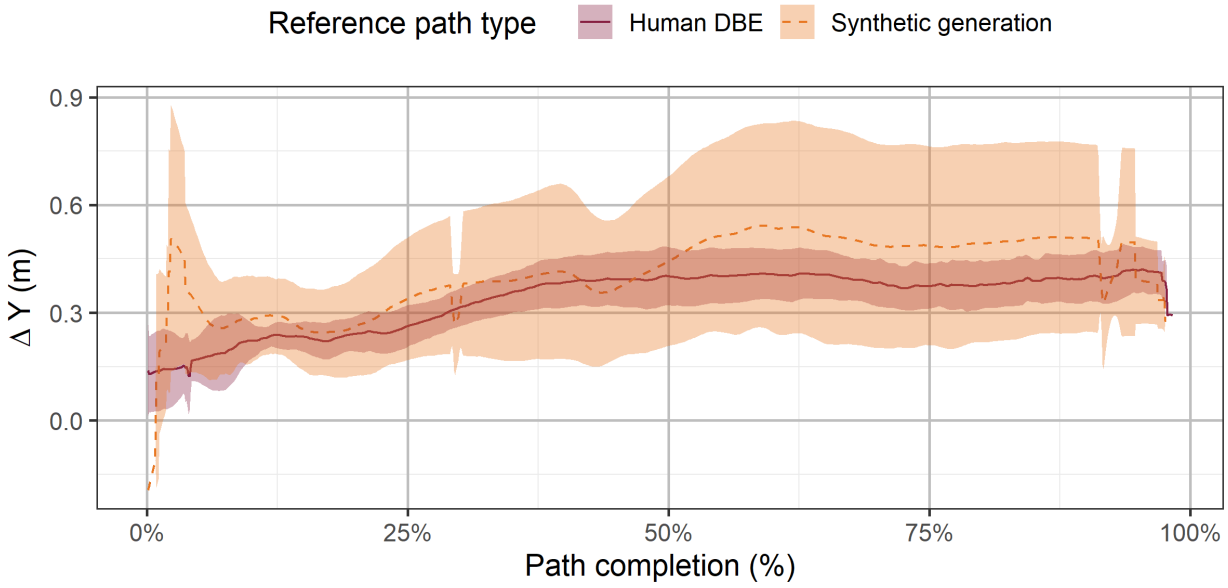

Figure 79. Ensemble average ΔY vs. TC% for the right-turn traffic circle maneuvers (S4.0, reference path comparison, Vehicle A)

In addition to manually calculated waypoints, another method of creating a synthetic reference path was using the CarMaker simulation software. To validate this method, a set of waypoints was generated for the slalom maneuver using CarMaker, and both the DBE and CarMaker reference paths are plotted in Figure 80. The CarMaker reference path showed a larger lateral deviation, resulting in an increased lateral acceleration request from the control system.

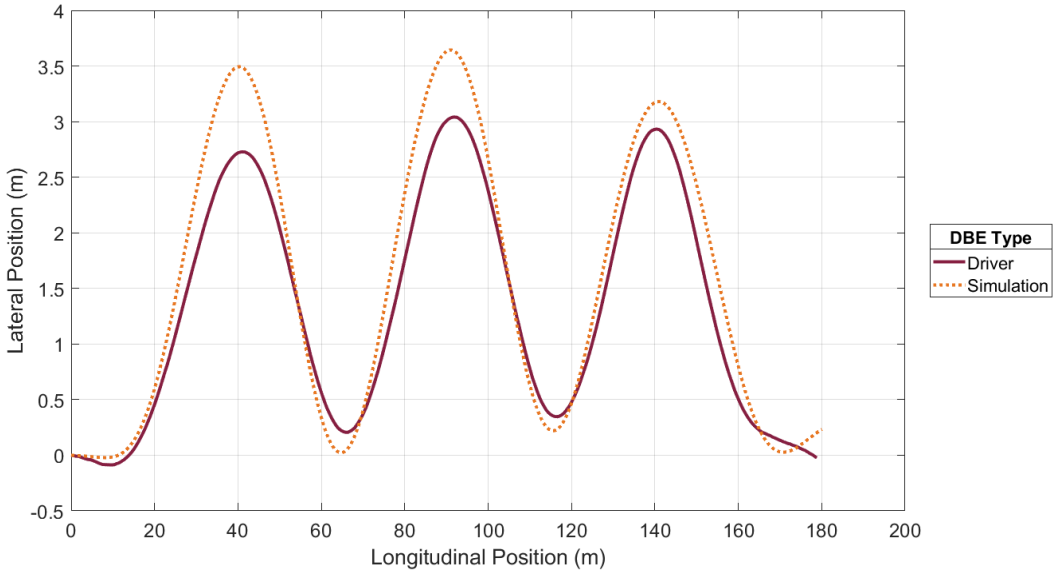

Figure 80. Trajectory plots for the v_{target} = 11.2 m/s slalom at a_y = 2.9 m/s^2 (S5.0, reference path comparison, Vehicle A)

When the CarMaker path was fed into Vehicle A, the ADS exhibited similar corner smoothing behavior as the DBE reference path. More notably, the vehicle was unable to fully complete the maneuver at the intended design speed of 11.2 m/s (25 mph) due to the increased lateral acceleration request. This instability was similar to the response exhibited during the downhill road grade testing, where a 0.65 m/s increase in speed resulted in the inability to complete the maneuver. Because of this, a slightly slower slalom at 8.9 m/s (20 mph) was implemented to compare the DBE and CarMaker paths. Figure 81 shows the ΔY response for the human DBE and the two slalom speeds.

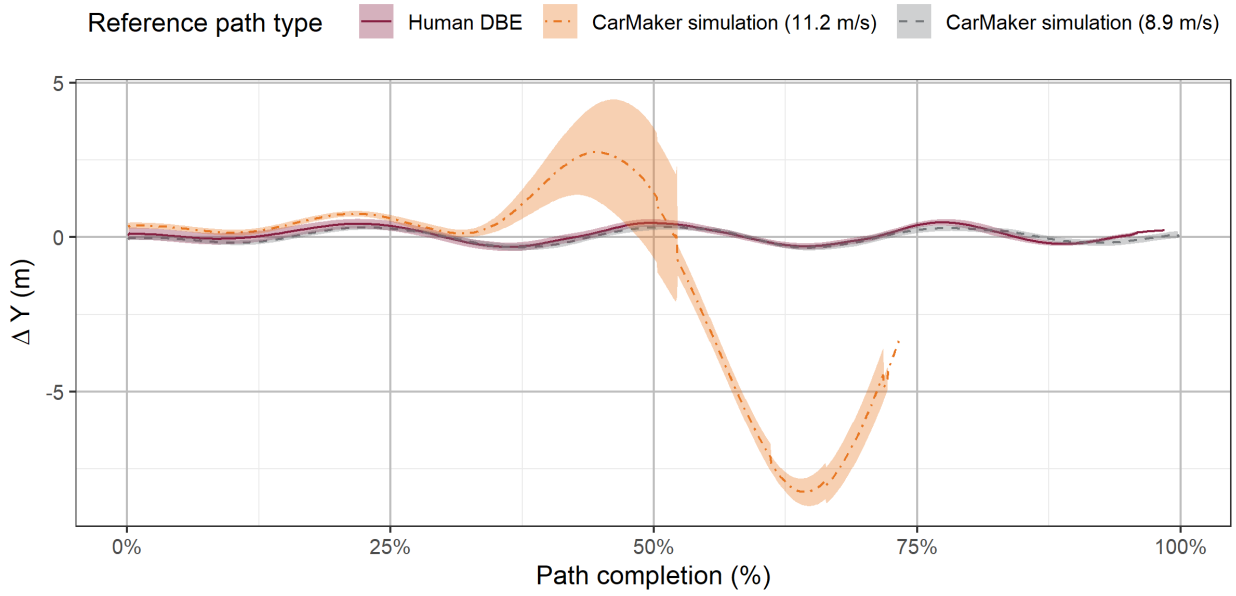

Figure 81. Ensemble average ΔY vs. $TC_{\%}$ for the v_{target} = 11.2 m/s slalom at a_y = 2.9 m/s^2 (S5.0, reference path comparison, Vehicle A)

4.8 Initial Condition Analysis

An initial condition analysis was completed to determine the effects of beginning the ADS playback slightly off-path at test initiation. During normal operation of an ADS, it is unlikely that the system would encounter sudden lateral offsets because the planning subsystem would constantly track and update the vehicle's current position. However, because the developed test method involved injecting the waypoints into the motion control system, initial lateral offsets from the ground truth path could affect the behavior of the ADS and thus the experimental results. Figure 82 provides the initial condition analysis for both test vehicles. The vehicles were intentionally staged off-path for the Scenario 1.0 maneuver, and the distance

percentage needed to return to "nominal behavior" was recorded. Because these tests were applied to straight-line maneuvers, "nominal behavior" was defined as a ΔY less than 0.4 meters and a yaw rate less than 1 deg/s.

Vehicle B was robust to the initial offsets and always completed the Scenario 1.0 maneuver. Conversely, Vehicle A maintained its right-side bias and failed to complete the maneuver if the initial offset exceeded approximately 0.75 meters to the right or 0.25 meters to the left of the reference path. During the data collection stage, the test vehicles were staged within approximately 0.5 meters as best as possible to avoid initial condition errors from occurring beyond the first 10% of each maneuver. However, there were still a small number of instances where the vehicle's initial conditions would lead to unsuccessful path completion.

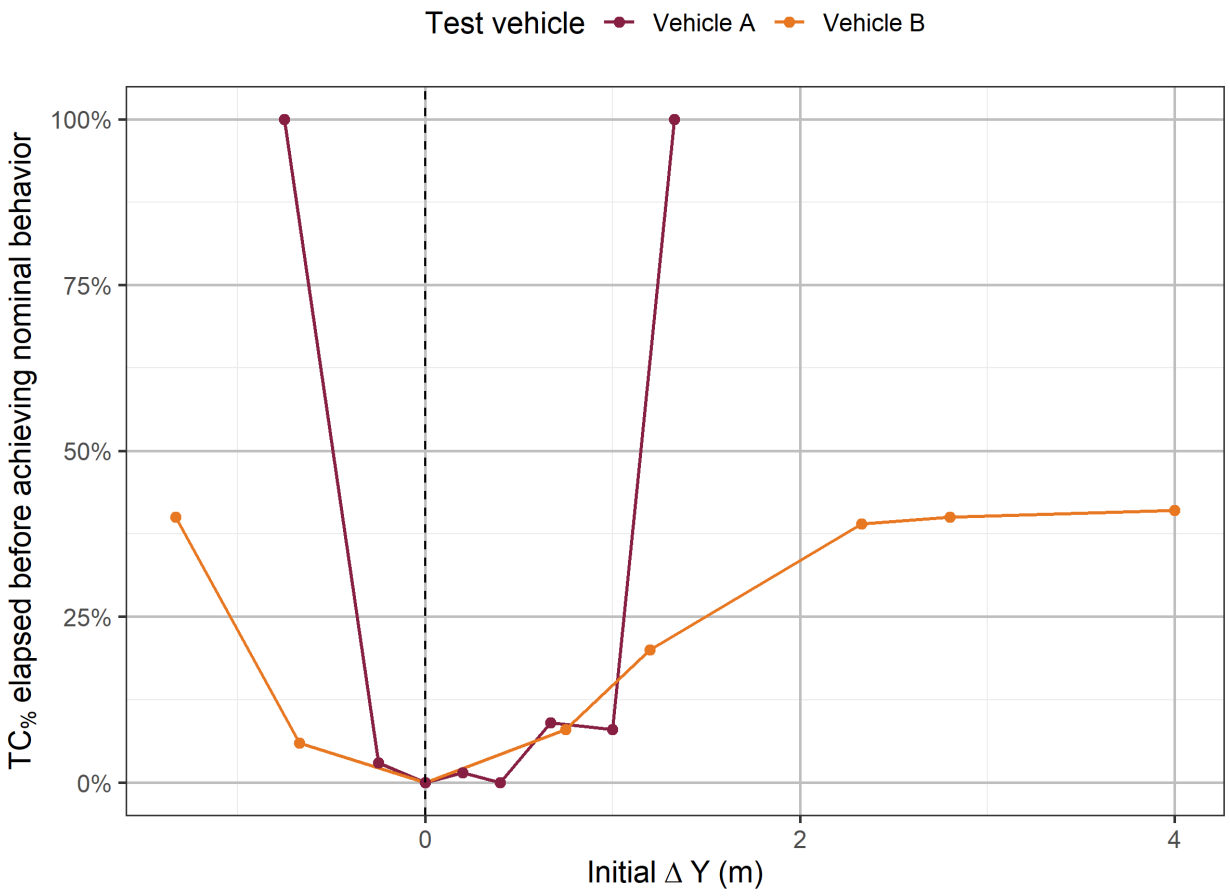

Figure 82. Relationship between initial ΔY and the distance needed regain the path and nominal behavior for the start-to-top maneuver. DV: v_{target} = 11.2 m/s, a_x^- = 3.9 m/s^2 (S1.0, both vehicles)

5 CONCLUSION

Automated driving systems, or vehicles capable of achieve L3+ autonomy, are a cutting-edge engineering challenge that are projected to greatly benefit society in many ways, including crash prevention, traffic alleviation, cost savings, and more. However, their successful development, public acceptance, and large-scale deployment hinges on their ability to successfully navigate complex and dynamic environments. Currently, no standardized method of evaluating automated driving systems exists, yet they must still be comprehensively tested and evaluated prior to their deployment on public roadways. This thesis aims to contribute toward ADS evaluation efforts by (1) develop an objective, repeatable, and practicable methodology for solely characterizing the motion control subsystem of an ADS and (2) demonstrating the characterization method using two dissimilar test vehicles.

The test method involved the implementation of five driving scenarios encompassing straight-line, lane change, intersection, traffic circle, and slalom maneuvers. These scenarios were used to cover the basic on-road operations that an ADS may encounter and exercise the longitudinal and lateral motion control systems. Furthermore, external disturbances in the form of vehicle and roadway condition changes were implemented into the scenarios to explore any changes to the behavior of the ADS in response to the external stimuli.

Once test scenarios were defined, the maneuvers for each scenario were implemented by establishing a reference trajectory and injecting it into the control system. The reference trajectory was formulated with two overarching methods: a human-based DBE and a synthetic reference trajectory. The DBE method was primarily utilized for this project, but methods for implementing synthetically derived trajectories via (1) mathematical derivation or (2) simulation software were also validated to improve the repeatability and practicability of the experimental method.

The next step involved deriving objective metrics that could be used to quantify the vehicle's performance, namely the vehicle's ability to follow the ground truth trajectory. The metrics were grouped into two categories: primary and secondary metrics. The primary metrics directly described the vehicle's path following behavior, and this included the lateral offset (ΔY), heading error ($\Delta\Psi$), speed error (Δv), stop error, and test completion percentage. Along with the

primary metrics, secondary metrics were derived to provide more insight into why the ADS performed as observed.

On-road testing of the proposed method was then completed across two exemplar control systems. The defined metrics were used to characterize the motion control of each ADS and compare how the two test vehicles differed during the maneuver execution relative to the reference path. The characterization method determined that the control system of Vehicle A (1) lagged in throttle and brake actuation, (2) consistently turned earlier and with a larger curvature, and (3) could not maintain the reference path when the lateral acceleration exceed 3.5 m/s^2. On the other hand, the characterization method showed that the control system of Vehicle B (1) consistently exhibited a small lag before turning and (2) tended to overshoot lane changes at higher lateral accelerations.

In addition to the baseline scenarios, several disturbances were introduced to evaluate the robustness of the ADS towards external stimuli. Both left-side and right-side tire pressure reductions did not show any meaningful impact on lateral deviations but showed a small improvement in stopping errors due to the increased tire drag. Bumps, though evident as induced noise in the yaw rate data, showed no impact to the path following capability, likely due to the underlying vehicle architecture (e.g., independent suspensions) and the fact that both vehicles were within their linear lateral operating range. Road grade showed expected behaviors of speed overshoot when going downhill and speed undershoot when going uphill. Although the downhill grades only increased the mean speed of the vehicles by up to 0.6 m/s, this increase resulted in unstable behavior for Vehicle A during the slalom maneuver due to larger lateral accelerations and increased stopping distances due to the vehicles coasting at the end of each maneuver before rest and overshooting the braking phases more.

Once the ADS response to the disturbance tests was quantified, the synthetically generated reference trajectories were validated. Finally, an initial condition analysis was conducted to determine the effect of staging the vehicles slightly to the left or right of the beginning of the reference path, and the method highlighted that Vehicle B's control system was more robust to initial lateral offsets while Vehicle A's control system failed to regain the reference path if it was laterally staged up to 0.75 meters off path.

5.1 Limitations and Future Work

There were a few limitations in this study that should be addressed. Because the purpose of this study was to solely characterize the maneuver subsystem, any functions involving the perception and planning subsystems were not in the scope of this project. For example, analyzing how the vehicle generates the path was out of scope because the perception and planning subsystems work together to generate the waypoints. Instead, a reference path was provided to the system as if it were being received from the trajectory planning. Additionally, the system's response to objects or a changing environment was not covered because the perception and planning portions would address this situation and pass adjustments to the motion control as an updated trajectory. Also, this project only tested the vehicle control systems in its linear operation range and under dry, bituminous road conditions, although low road friction conditions could impact the overall performance of a motion control system when present. Lastly, an anti-aliasing filter was not implemented upstream of the GPS and IMU data sampling, so it is possible that the sampling frequency did not satisfy the Nyquist-Shannon theorem. To mitigate potential aliasing, a lowpass filter was used prior to down sampling the IMU data to match the sampling rate of the GPS data. However, this led to the full dataset including data that were not filtered and data that were filtered and interpolated to a lower frequency.

Future work building off this project could take a variety of routes. An expansion of the current project could implement more vehicle disturbances (e.g., depreciated wheel alignment or toe-in) or low road friction tests, (e.g., testing with worn tire tread or wet roads). Aside from an expansion project, a continuation of this work could involve developing and demonstrating characterization methods of either (1) a different subsystem—perception or path planning—in isolation or (2) a holistic characterization of the ADS.

REFERENCES

49 CFR § 571.126 Federal Motor Vehicle Safety Standards; Electronic Stability Control Systems p648-659 (2007). https://www.govinfo.gov/app/details/CFR-2011-title49-vol6/CFR-2011-title49-vol6-sec571-126

49 CFR § 571.135 Federal Motor Vehicle Safety Standards; Light Vehicle Brake Systems. p668-688 (2005). https://www.govinfo.gov/app/details/CFR-2011-title49-vol6/CFR-2011-title49-vol6-sec571-135

49 CFR § 571.138. Federal Motor Vehicle Safety Standards; Tire Pressure Monitoring Systems p688-693 (2005). https://www.govinfo.gov/app/details/CFR-2011-title49-vol6/CFR-2011-title49-vol6-sec571-138

American Association of State Highway and Transportation Officials. (2018). *A Policy on Geometric Design of Highways and Streets* (7th ed.).

Bando, M., Hasebe, K., Nakayama, A., Shibata, A., & Sugiyama, Y. (1995). Traffic Jams without Bottlenecks—Experimental Evidence for the Physical Mechanism of the Formation of a Jam. *Physical Review*, 51(2), 1035-1042. https://doi.org/10.1103/PhysRevE.51.1035

Behere, S., & Torngren, M. (2015, May 4-8). *A Functional Architecture for Autonomous Driving* [Paper presentation]. 2015 First International Workshop on Automotive Software Architecture (WASA), Montreal, Canada. https://doi.org/10.1145/2752489.2752491

Carter, N., Beier, S., & Cordero, R. (2019). Lateral and Tangential Accelerations of Left Turning Vehicles from Naturalistic Observations. *SAE Technical Papers*, 1-17.

Daily, M., Medasani, S.S., Behringer, R., & Trivedi, M.M. (2017). Self-Driving Cars. *Computer*, 50, 18-23.

Federal Highway Administration. (2022). *Manual on Uniform Traffic Control Devices (MUTCD)*. https://mutcd.fhwa.dot.gov/htm/2009/part3/fig3b_21_longdesc.htm

Happer, A. D., Peck, M. D., & Hughes, M. C. (2009). Analysis of Left-turning Vehicles at a 4-way Medium-sized Signalized Intersection. *SAE International Journal of Passenger Cars - Mechanical Systems*, *2*(1), 359-370.

Haus, S., Sherony, R., & Gabler, H. C. (2019). Estimated Benefit of Automated Emergency Braking Systems for Vehicle-pedestrian Crashes in the United States. *Traffic Injury Prevention*, *20*, 171-176.

Hirsch, M. (2016). *pymap3d: Python 3D coordinate conversions for geospace (v1.0)*. In SciVision. https://github.com/geospace-code/pymap3d

Hogema, J., Wentink, M., & Bertollini, G. (2012). *Effects of Yaw Motion on Driving Behaviour, Comfort, and Realism* [Paper presentation]. Driving Simulation Conference 2012, Paris, France.

Holland-Letz, D., Kässer, M., Kloss, B., & Müller, T. (2019). Start Me Up: Where Mobility Investments are Going. *McKinsey & Company*. Retrieved from https://www.mckinsey.com/industries/automotive-and-assembly/our-insights/start-me-up-where-mobility-investments-are-going

Huey, R., Harpster, J., & Lerner, N. (1995). *Field Measurement of Naturalistic Backing Behavior*. National Highway Traffic Safety Administration.

Hugemann, W., & Nickel, M. (2003). *Longitudinal and Lateral Accelerations in Normal Day Driving*. European Association for Accident Research and Analysis. https://www.unfallrekonstruktion.de/pdf/itai_2003_english.pdf

Institute of Transportation Engineers. (1999). *Traffic Engineering Handbook* (5th ed.).

International Organization for Standardization. (2018). Road Vehicles — Functional Safety.

International Organization for Standardization. (2022). Safety of the Intended Functionality.

Iowa Statewide Urban Design and Specifications. (2022). *SUDAS Design Manual* https://intrans.iastate.edu/app/uploads/sites/15/2020/03/8B-1.pdf

IPG Automotive GmbH. (2021). CarMaker User Manual. IPG Automotive GmbH.

Karnouskos, S. (2020). Self-driving Car Acceptance and the Role of Ethics. *IEEE Transactions on Engineering Management*, 67(2), 252–265. https://doi.org/10.1109/tem.2018.2877307

Kusano, K., & Gabler, H. C. (2011). Method for Estimating Time to Collision at Braking in Real-world, Lead Vehicle Stopped Rear-End Crashes for use in Pre-crash System Design. *SAE International Journal of Passenger Cars - Mechanical Systems*, *4*, 435-443.

Malvin, N. & Pudjaprasetya, Sri. (2020). Staggered Conservative Scheme for Simulating the Emergence of a Jamiton in a Phantom Traffic Jam. *International Journal of Intelligent Transportation Systems Research.* 19. 10.1007/s13177-020-00229-y.

Mathworks. (2020). *latlon2local*. https://www.mathworks.com/help/driving/ref/latlon2local.html

National Highway Traffic Safety Administration (2021). Traffic Safety Facts 2019: A Compilation of Motor Vehicle Crash Data. *National Center for Statistics and Analysis.*

National Highway Traffic Safety Administration. (2015). Critical Reasons for Crashes Investigated in the National Motor Vehicle Crash Causation Survey. (Traffic Safety Facts Research Note. Report No. DOT HS 812 115). *U.S. Department of Transportation.*

Pütz, A., Zlocki, A., Bock, J., & Eckstein, L. (2017*). System Validation of Highly Automated Vehicles with a Database of Relevant Traffic Scenarios* [Paper presentation]. 12th ITS European Congress, Strausbourg, France.

Rehrl, K., & Gröchenig, S. (2021). Evaluating Localization Accuracy of Automated Driving Systems. *Sensors*, 21(17), 5855. https://doi.org/10.3390/s21175855

SAE International. (2016). J2945 On-board System Requirements for V2V Safety Communications

SAE International. (2021). J3016 Taxonomy and Definitions for Terms Related to Driving Automation Systems for On-Road Motor Vehicles.

SAE International. (2022a). J3131 Definitions for Terms Related to Automated Driving Systems Reference Architecture.

SAE International. (2022b). J670 Vehicle Dynamics Terminology.

Sarmento, A., Garcia, B., Coriteac, L., & Navarenho, L. (2017). The Autonomous Vehicle Challenges for Emergent Market. *SAE Technical Paper Series.* https://doi.org/10.4271/2017-36-0436

Schrank, D., Albert, L., Eisele, B., & Lomax, T. (2021). 2021 Urban Mobility Report.

Statista DossierPlus (2019). Statista DossierPlus on the Market for Autonomous Vehicles.

Tavassoli, A., Cymbalist, N., Dunning, A., & Krauss, D. (2019). Learning from Human Naturalistic Driving Behavior at Stop Signs for Autonomous Vehicles. *SAE Technical Papers*, 1-5.

Tavassoli, A., King, D., Xiouris, C., & Krauss, D. (2021). Revealing Right-turn Behavior of Human Drivers as a Model for Autonomous Vehicles. *SAE Technical Papers,* 1-6.

Thorn, E., Kimmel, S. C., & Chaka, M. (2018). *A Framework for Automated Driving System Testable Cases and Scenarios* (Report No. DOT HS 812 623). National Highway Traffic Safety Administration. https://rosap.ntl.bts.gov/view/dot/38824

Urmson, C., & Whittaker, W. (2008). Self-driving Cars and the Urban Challenge. *IEEE Intelligent Systems*, 23(2), 66–68. https://doi.org/10.1109/mis.2008.34

VA Code 46.2-870. https://law.lis.virginia.gov/vacode/title46.2/chapter8/section46.2-870/

VA Code 46.2-873. https://law.lis.virginia.gov/vacode/title46.2/chapter8/section46.2-873/

Wang, J., Dixon, K., Li, H., & Ogle, J. (2004). Normal Acceleration Behavior of Passenger Vehicles Starting from Rest at All-way Stop-controlled Intersections. *Transportation Research Record, 1883*, 158-166.

Wang, J., Dixon, K., Li, H., & Ogle, J. (2005). Normal Deceleration Behavior of Passenger Vehicles at Stop Sign-controlled Intersections Evaluated with in-vehicle GPS Data. *Transportation Research Record, 1937*, 120-127.

Zhang, P., Zhu, B., Zhao, J. et al. Performance Evaluation Method for Automated Driving System in Logical Scenario. *Automotive Innovation*, 5, 299–310 (2022). https://doi.org/10.1007/s42154-022-00191-3

APPENDIX A: LITERATURE REVIEW SUMMARY

Table 26. Summary of sources used to develop representative target speed parameters (mph)

Value	Description	Source
15	VA minimum school zone speed limit	(VA Code)
25	VA statutory speed limit of business/residential areas	(VA Code)
55	VA statutory speed limit of interstate highways, divided limited access highways, and non-limited access highways with at least four lanes	(VA Code)

Table 27. Summary of sources used to develop representative longitudinal acceleration (g) parameters

Value	Description	Title	Author(s)
0.27 0.16	90th and 50th percentile acceleration of drivers beginning from rest	Longitudinal and Lateral Accelerations in Normal Day Driving	(Hugemann & Nickel, 2003)
0.16	Average acceleration of drivers leaving stop signs	Learning from Human Naturalistic Driver Behavior at Stop Signs for AVs	(Tavassoli et al., 2019)
0.13	Average driver's 0 to 60 kph acceleration	Traffic Engineering Handbook, 5th ed.	(ITE, 1999)
0.13	Average acceleration of drivers leaving stop-controlled intersections	Normal Acceleration Behavior of Passenger Vehicles Starting from Rest at All-Way Stop-Controlled Intersections	(Wang et al., 2004)
–0.8	Estimated maximum AEB braking magnitude under dry conditions	Estimated Benefit of Automated Emergency Braking Systems for Vehicle-Pedestrian Crashes in the United States	(Haus et al., 2019)
–0.58	Minimum average braking requirements for all U.S. light vehicles	FMVSS 135 – Light Vehicle Brake Systems	(49 CFR § 571.135, 2005)
–0.59 –0.44	Average braking of rear-end crashes involving a stopped lead vehicle for (a) TTC ≤ 1.5 s, and (b) 1.5 s < TTC < 2.5 s	Method for Estimating Time to Collision at Braking in Real-World, Lead Vehicle Stopped Rear-End Crashes for Use in Pre-Crash System Design	(Kusano & Gabler, 2011)
–0.39 –0.22	(a) 90th percentile braking for "unplanned" stops and (b) 50th percentile braking for "planned" stops	Longitudinal and Lateral Accelerations in Normal Day Driving	(Hugemann & Nickel, 2003)
–0.34	Braking threshold used to determine stopping distance	A Policy on Geometric Design of Highways and Streets, 7th ed. (Table 3-1)	(AASHTO, 2018)
–0.19	Average braking of drivers approaching stop signs	Learning from Human Naturalistic Driver Behavior at Stop Signs for AVs	(Tavassoli et al., 2019)
–0.13	Average braking of drivers approaching stop signs	Normal Deceleration Behavior of Passenger Vehicles at Stop Sign-Controlled Intersections Evaluated with In-Vehicle GPS Data	(Wang et al., 2005)

Table 28. Summary of sources used to develop representative lateral acceleration (g) parameters

Value	Description	Title	Author(s)
0.41 0.29	Average lateral acceleration magnitude experienced for 90-degree turns with radii of (a) 8.5 feet and (b) 20 feet	Effects of Yaw Motion on Driving Behavior, Comfort, and Realism	(Hogema et al., 2012)
0.38 0.32 0.27 0.23	Limiting values of lateral acceleration magnitudes for design speeds of (a) 10 mph, (b) 15 mph, (c) 20 mph, and (d) 25 mph on flat roads	A Policy on Geometric Design of Highways and Streets, 7th ed. (Table 3-7)	(AASHTO, 2018)
0.17	Average maximum lateral acceleration of drivers approaching non-protected left turns	Lateral and Tangential Accelerations of Left Turning Vehicles from Naturalistic Observations	(Carter et al., 2019)

Table 29. Summary of sources used to develop representative longitudinal acceleration (g) parameters within intersection environments

Value	Description	Title	Author(s)
0.12	Average maximum tangential acceleration of drivers approaching non-protected (yielding) left turns	Lateral and Tangential Accelerations of Left Turning Vehicles from Naturalistic Observations	(Carter et al., 2019)
0.10	Average tangential acceleration of drivers proceeding through left turns from rest	Analysis of Left-Turning Vehicles at a 4-Way Medium-Sized Signalized Intersection	(Happer et al., 2009)
0.15	Average tangential acceleration of drivers proceeding through right turns from rest	Revealing Right-Turn Behavior of Human Drivers as a Model for AVs	(Tavassoli et al., 2021)
–0.19	Average braking of drivers approaching stop signs	Learning from Human Naturalistic Driver Behavior at Stop Signs for AVs	(Tavassoli et al., 2019)
–0.17	Average braking of drivers approaching right turns	Revealing Right-Turn Behavior of Human Drivers as a Model for AVs	(Tavassoli et al., 2021)
–0.13	Average braking of drivers approaching stop signs	Normal Deceleration Behavior of Passenger Vehicles at Stop Sign-Controlled Intersections Evaluated with In-Vehicle GPS Data	(Wang et al., 2005)

APPENDIX B: DBE AND CONE SETUP INSTRUCTIONS

The following sections describe the cone setup and maneuver execution required to generate a DBE reference path. More specifically, each maneuver contains driver instructions, a scenario execution schematic, and tables with each row corresponding to a unique DV as well as cone measurements. Within each schematic, the maroon and orange squares represent cones, and the blue square signifies an optical gate cone for flagging active portions of test playbacks.

Straight Line Maneuvers

Figure 83 illustrates the cone setup, and Table 30 and Table 31 list the kinematic parameters and cone setup distances for Scenario 1.0: straight-line acceleration, dwell, and braking maneuver. The test procedure is as follows:

1. Begin at the start cone and accelerate at a constant magnitude (a_x^+) until reaching v_{target} at cone A. The midpoint cone is specified to help guide the driver
2. Hold v_{target} until cone B (at least 5 seconds)
3. Brake with constant magnitude (a_x^-) until reaching cone C. Ensure the optical gate sensor has ended the test active flag

A total of four speeds, two accelerations, and three braking magnitudes were used, and 12 combinations of these values were selected: speeds of 15, 25, 40, and 55 mph (24, 40, 64, 88 kph); acceleration magnitudes of 0.15 g and 0.25 g; braking magnitudes of 0.2 g, 0.4 g, and 0.6 g; and dwell time of at least 5 seconds during segment AB. To simplify the cone setup process, the AB cone distance was held constant and while the surrounding cones were adjusted. For example, segment AB was 293 feet for the 15-, 25-, and 40-mph tests and 403 feet for the 55-mph test.

Figure 83. Layout and execution of the start-to-stop maneuver

Table 30. List of DVs for Scenario 1.0 and the respective cone distances required to set up maneuver execution (English units)

v_{start} (mph)	v_{target} (mph)	a_x^+ (g)	a_x^- (g)	Start to half (ft)	Half to A (ft)	AB (ft)	BC (ft)	Total (ft)
0	15	0.15	-0.2	13	38	110	38	199
0	15	0.25	-0.4	8	23	110	19	160
0	15	0.25	-0.6	8	23	110	13	154
0	25	0.15	-0.2	35	104	183	104	426
0	25	0.25	-0.4	21	63	183	52	319
0	25	0.25	-0.6	21	63	183	35	302
0	40	0.15	-0.2	89	267	293	267	916
0	40	0.25	-0.4	53	160	293	134	640
0	40	0.25	-0.6	53	160	293	89	595
0	55	0.15	-0.2	169	506	403	506	1584
0	55	0.25	-0.4	101	303	403	253	1060
0	55	0.25	-0.6	101	303	403	169	976

Table 31. List of DVs for Scenario 1.0 and the respective cone distances required to set up maneuver execution (metric units)

v_{start} (kph)	v_{target} (kph)	a_x^+ (m/s^2)	a_x^- (m/s^2)	Start to half (m)	Half to A (m)	AB (m)	BC (m)	Total (m)
0	24	1.47	-1.96	4.0	11.6	33.5	11.6	60.7
0	24	2.45	-3.92	2.4	7.0	33.5	5.8	48.8
0	24	2.45	-5.89	2.4	7.0	33.5	4.0	46.9
0	40	1.47	-1.96	10.7	31.7	55.8	31.7	129.8
0	40	2.45	-3.92	6.4	19.2	55.8	15.8	97.2
0	40	2.45	-5.89	6.4	19.2	55.8	10.7	92.0
0	64	1.47	-1.96	27.1	81.4	89.3	81.4	279.2
0	64	2.45	-3.92	16.2	48.8	89.3	40.8	195.1
0	64	2.45	-5.89	16.2	48.8	89.3	27.1	181.3
0	88	1.47	-1.96	51.5	154.2	122.8	154.2	482.8
0	88	2.45	-3.92	30.8	92.3	122.8	77.1	323.1
0	88	2.45	-5.89	30.8	92.3	122.8	51.5	297.5

Figure 84 illustrates the execution, and Table 32 and Table 33 list the kinematic parameters and timing required to execute Scenario 1.1: the longitudinal sinusoid maneuvers. The test procedure is as follows:

1. Begin the test at the target speed, v_{target}, and hold this speed through the first optical gate
2. Brake with constant magnitude (a_x^-) until reaching the lowered speed, v_{lower}
3. Accelerate with constant magnitude (a_x^+) until reaching the original target speed
4. Repeat steps 2 and 3
5. When finished, drive past the second optical gate to end the test active flag

One target speed and two lowered speed conditions were used. One acceleration magnitude and three braking magnitudes were specified: a target speed 25 mph (40 kph); an

acceleration magnitude of 0.2 g; and braking magnitudes of 0.2 g, 0.4 g, and 0.6 g. It should be noted that the 0.6 g braking magnitude was removed for the 25-mph to 15-mph tests because it was not feasible by a driver or control system because it is essentially a quick jab at the brakes.

This scenario was approached by tracking the acceleration and braking events by time rather than by distance (cone setup) because errors in acceleration and braking distance would propagate along the sinusoid. The time required for each longitudinal acceleration epoch was calculated, and a metronome tempo that most closely yielded a whole number of beats to simplify the timing was selected. Using the first listed design variation as an example, the driver would set the metronome to 126 BPM. After reaching v_{target}, the driver would take 12 clicks to reach rest, then immediately take 16 clicks to reach v_{target} before repeating the whole process.

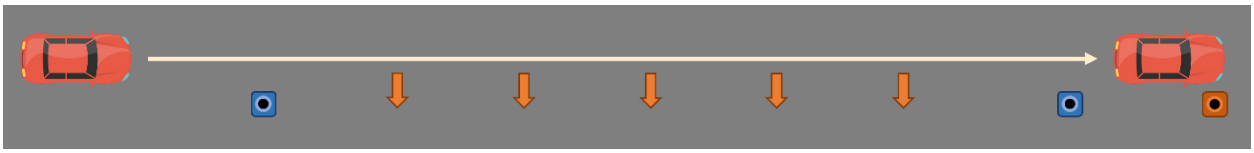

Figure 84. Layout and execution of the longitudinal sinusoid maneuver

Table 32. List of DVs for Scenario 1.1 and the respective brake and throttle timing required to execute the maneuver (English units)

v_{target} (mph)	a_x^- (g)	v_{lower} (mph)	a_x^+ (g)	t_1 (s)	t_2 (s)	Braking click	Accel click	Distance per sinusoid (ft)	BPM
25	-0.2	0	0.2	5.71	5.71	12.0	12.0	210	126
25	-0.4	0	0.2	2.85	5.71	6.0	12.0	157	
25	-0.6	0	0.2	1.90	5.71	4.0	12.0	140	
25	-0.2	15	0.2	2.28	2.28	6.0	6.0	134	160
25	-0.4	15	0.2	1.14	2.28	3.0	6.0	101	

Table 33. List of DVs for Scenario 1.1 and the respective brake and throttle timing required to execute the maneuver (metric units)

v_{target} (kph)	a_x^- (m/s^2)	v_{lower} (kph)	a_x^+ (m/s^2)	t_1 (s)	t_2 (s)	Braking click	Accel click	Distance per sinusoid (m)	BPM
40	-1.96	0	1.96	5.71	5.71	12.0	12.0	63.9	126
40	-3.92	0	1.96	2.85	5.71	6.0	12.0	48.0	
40	-5.89	0	1.96	1.90	5.71	4.0	12.0	42.6	
40	-1.96	24	1.96	2.28	2.28	6.0	6.0	40.9	160
40	-3.92	24	1.96	1.14	2.28	3.0	6.0	30.7	

Lane Change Maneuver

Figure 85 illustrates the cone setup, and Table 34 and Table 35 list the kinematic parameters and cone setup distances for Scenario 2.0, the lane change with braking maneuver. Lateral acceleration peaked around 0.3 g during the lane change maneuver, and the lane width was 12 ft (3.66 m). The test procedure is as follows:

1. Begin the test at the target speed, v_{target}, and hold this speed through the first optical gate
2. Hold v_{target} and continue driving straight until cone A
3. Begin the lane change at cone A and complete it when reaching cone B; maintain v_{target}
4. Hold v_{target} and continue driving straight until cone C
5. Begin the lane change at cone C and complete it when reaching cone D; maintain v_{target}
6. At cone D, start braking with magnitude a_x^- and come to a stop at cone E
7. Drive past the second optical gate to end the test active flag

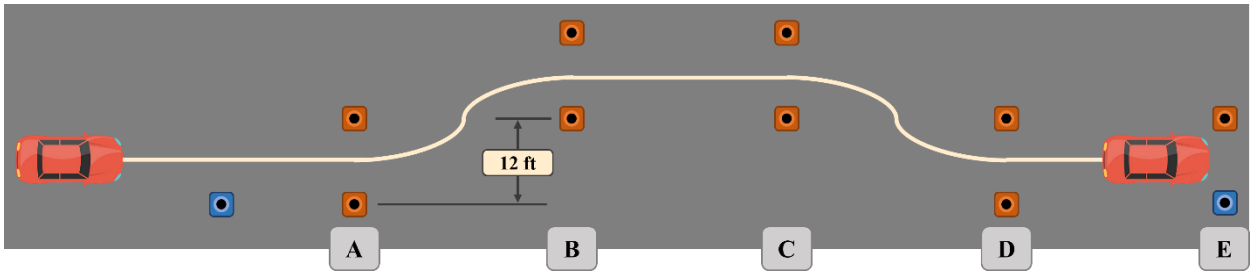

Figure 85. Layout and execution of the double lane change with braking maneuver

Table 34. List of DVs for Scenario 2.0 and the respective cone distances required to set up maneuver execution (English units)

v_{target} (kph)	a_x^- (g)	a_y (g)	Start to A (ft)	AB (ft)	BC (ft)	CD (ft)	DE (ft)	Total (ft)
25	-0.40	0.30	50	82	82	82	52	432
40	-0.40	0.30	50	115	115	115	134	742

Table 35. List of DVs for Scenario 2.0 and the respective cone distances required to set up maneuver execution (metric units)

v_{target} (kph)	a_x^- (m/s^2)	a_y (m/s^2)	Start to A (m)	AB (m)	BC (m)	CD (m)	DE (m)	Total (m)
40	-3.92	2.94	15.2	25.0	25.0	25.0	15.8	131.7
64	-3.92	2.94	15.2	35.1	35.1	35.1	40.8	226.2

Intersection Maneuvers

Figure 86 illustrates the cone setup, and Table 36 and Table 37 list the kinematic parameters for Scenario 3.0, the constant speed turning maneuvers. The test procedure is as follows:

1. Begin the test at the target speed, v_{target}, and hold this speed through the first optical gate
2. Turn while maintaining v_{target}
3. Hold v_{target} until reaching the second optical gate

Two turn radii and lateral acceleration limits that are representative of typical driving conditions were selected, and these variables were used to determine the target speed: turning radii of 25 and 60 feet (7.6 and 18.3 meters) and lateral acceleration limits of 0.3 g and 0.45 g. Speeds were calculated using the equation below,

$$R_{\text{min}} = \frac{v^2}{15(0.01e_{\text{max}} + f_{\text{max}})}$$

where $a_y(g) = f_{\text{max}}$ and e_{max} is the superelevation (AASHTO, 2018).

The cone setup procedure is outlined below. Radii were created using a tape measure and measured from the middle of the lane. The left and right turn gates are offset by 30 feet, and the 100-foot dwell sections were incorporated to ensure the vehicle reaches a steady state before and after the turn maneuver. A 50-foot buffer section was included to ensure that automation mode is triggered by then.

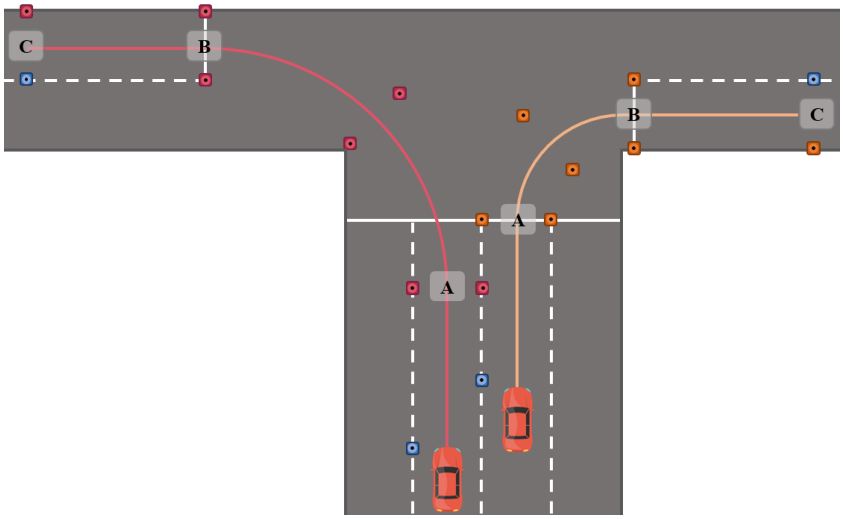

Figure 86. Layout and execution of the constant speed intersection turn maneuver

Table 36. List of DVs for Scenario 3.0 (English units)

r (ft)	$a_{y,\max}$ (g)	v_{target} (mph)
25	0.3	11
60	0.3	16
25	0.45	13
60	0.45	20

Table 37. List of DVs for Scenario 3.0 (metric units)

r (m)	$a_{y,\max}$ (m/s^2)	v_{target} (kph)
7.6	2.94	17
18.3	2.94	26
7.6	4.41	21
18.3	4.41	32

Figure 87 illustrates the cone setup, and Table 38 and Table 39 list the kinematic parameters for Scenario 3.1, the turning maneuvers that begin from rest. The setup remains the same as Scenario 3.0; the only difference is that the driver starts from rest at the beginning of the turn. Because the turns occur from rest, lower lateral acceleration limits are utilized. Radius measurements are relative to the middle of the lane. The test procedure is as follows:

1. Begin from rest at the first optical gate
2. Accelerate through the turn such that v_{target} is reached at the end of the turn
3. Hold v_{target} until reaching the second optical gate to end the test active flag

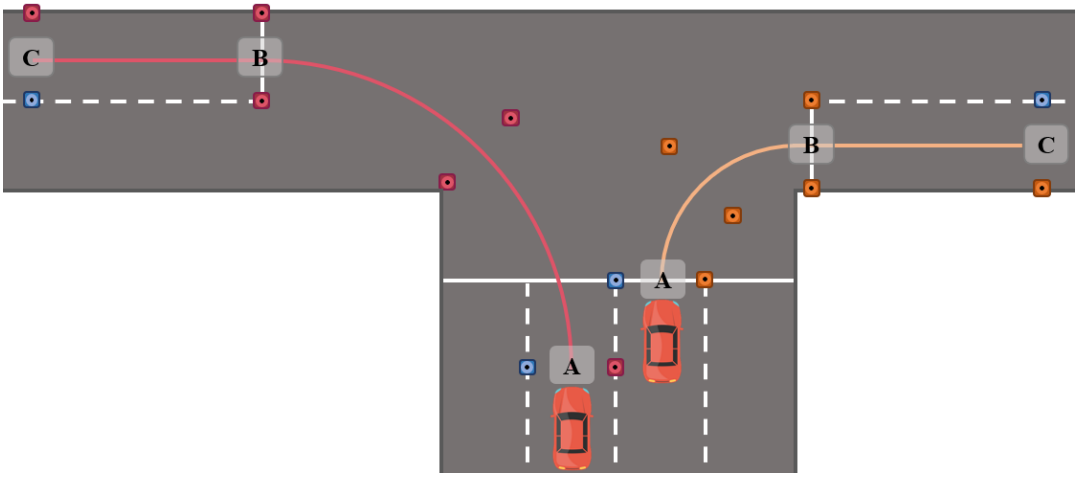

Figure 87. Layout and execution of the intersection turn from rest maneuver

Table 38. List of DVs for Scenario 3.1 (English units)

r (ft)	$a_{y,\max}$ (g)	v_{target} (mph)
25	0.15	8
60	0.15	12
25	0.3	11
60	0.3	16

Table 39. List of DVs for Scenario 3.1 (metric units)

r (m)	$a_{y,\max}$ (m/s^2)	v_{target} (kph)
7.6	1.47	12
18.3	1.47	19
7.6	2.94	17
18.3	2.94	26

Figure 88 illustrates the cone setup, and Table 40 and Table 41 list the kinematic parameters for Scenario 3.2, the turning maneuvers that contain braking from a higher speed into the turn before accelerating at the middle/end of the turn. This setup modifies Scenario 3.0 by incorporating a braking zone x_{straight} that reduces the vehicle's speed at a rate of 0.2 g at the beginning of the turn. The test procedure is as follows:

1. Begin the test at the start speed, v_{start}, and hold this speed through the first optical gate
2. Brake after passing the first optical gate with a constant magnitude until reaching $v_{\min}$ at the midpoint of the turn
3. After reaching the midpoint of the turn, begin accelerating until reaching v_{exit} at the end of the turn
4. Hold v_{exit} until reaching the second optical gate to end the test active flag

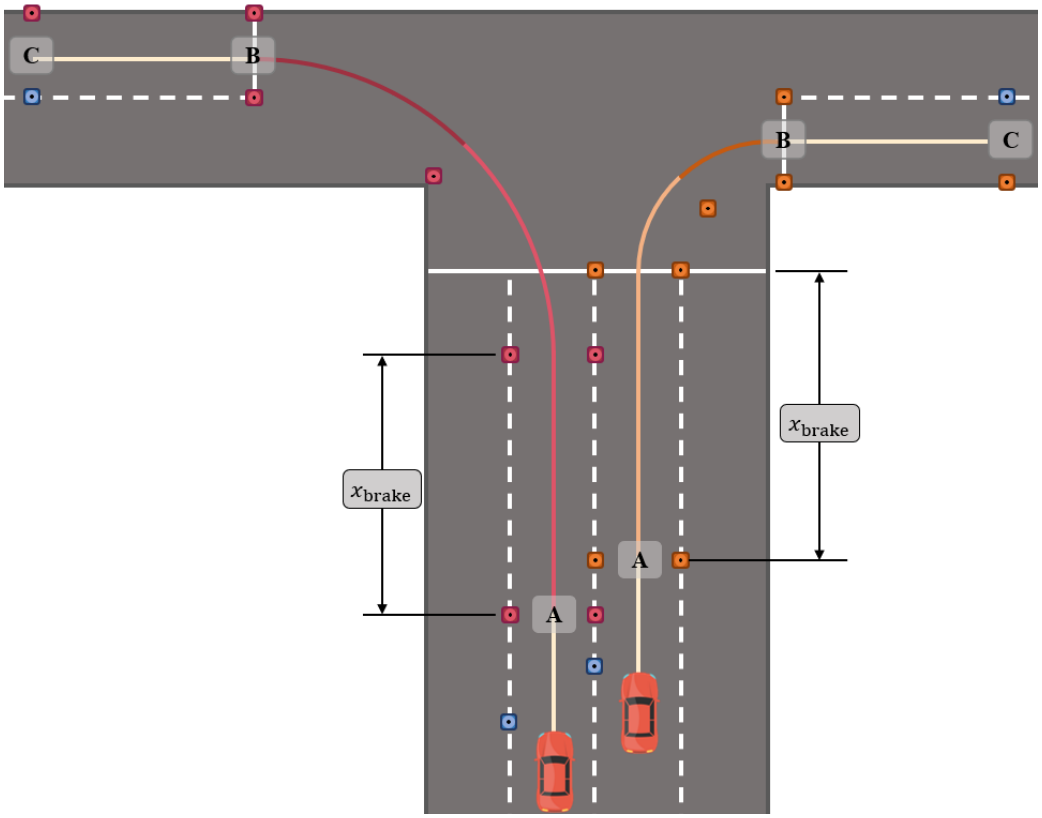

Figure 88. Layout and execution of the transient intersection turn maneuver

Table 40. List of DVs for Scenario 3.2 the respective cone distances required to set up the maneuver (English units)

R (ft)	$a_{y,\max}$ (g)	v_{start} (mph)	a_x^- (g)	$v_{\min}$ (mph)	x_{straight} (ft)	a_x^+ (g)	v_{exit} (mph)
25	0.3	25	-0.2	8	73.9	0.1	11
60	0.3	25	-0.2	12	33.0	0.08	16
25	0.3	40	-0.2	8	236.4	0.1	11
60	0.3	40	-0.2	12	195.5	0.08	16

Table 41. List of DVs for Scenario 3.2 the respective cone distances required to set up the maneuver (metric units)

R (m)	$a_{y,\max}$ (m/s^2)	v_{start} (kph)	a_x^- (m/s^2)	$v_{\min}$ (kph)	x_{straight} (m)	a_x^+ (m/s^2)	v_{exit} (kph)
7.6	2.94	40	-1.96	13	22.5	0.98	18
18.3	2.94	40	-1.96	19	10.1	0.78	26
7.6	2.94	64	-1.96	13	72.0	0.98	18
18.3	2.94	64	-1.96	19	59.6	0.78	26

Traffic Circle Maneuvers

Figure 89 illustrates the cone setup, and Table 42 and Table 43 list the kinematic parameters for Scenario 4.0, the maneuver that involves accelerating from rest before holding a constant speed circle. This setup can be utilized for both left- and right-hand circle maneuvers by facing the car in the opposite direction at the start cone and moving the optical gate sensors to the other side of the vehicle. The test procedure is as follows:

1. Begin the test from rest at the first optical gate
2. Accelerate such that v_{target} is reached at cone A, which is 90 degrees counterclockwise from the START cone
3. Hold v_{target} until cone C, which is 180 degrees counterclockwise from the START cone
4. Brake to rest before reaching the START cone
5. Ensure the optical gate sensor has ended the test active flag before beginning the next run

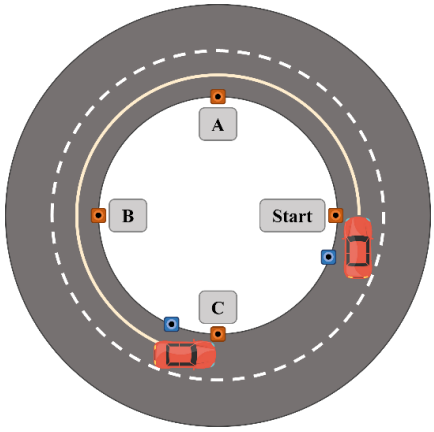

Figure 89. Layout and execution of the acceleration and constant speed traffic circle maneuver

Table 42. List of DVs for Scenario 4.0 (English units)

r (ft)	$a_{y,\max}$ (g)	v_{target} (mph)	Turn direction
50	0.3	15	Left
50	0.3	15	Right

Table 43. List of DVs for Scenario 4.0 (metric units)

r (m)	$a_{y,\max}$ (m/s^2)	v_{target} (m/s)	Turn direction
15.2	2.94	6.7	Left
15.2	2.94	6.7	Right

Figure 90 illustrates the cone setup, and Table 44 and Table 45 list the kinematic parameters for Scenario 4.1, the maneuver that involves accelerating from rest, conducting a lane change, and holding a constant speed circle. The cones from Scenario 4.0 were shifted one lane width (12 ft) radially. For the lane change out, the radius increases from 50 ft to 62 ft. For lane change in, the radius shrinks from 62 ft to 50 ft. The test procedure is as follows:

1. Begin the test from rest at the first optical gate
2. Accelerate such that v_{target} is reached at cone A, which is 90 degrees counterclockwise from the START cone
3. While holding v_{target}, change lanes between cones A and B, which are 90 degrees apart
4. Hold v_{target} until cone C, which is 90 degrees counterclockwise from cone B
5. Brake to rest before reaching the START cone
6. Ensure the optical gate sensor has ended the test active flag before beginning the next run

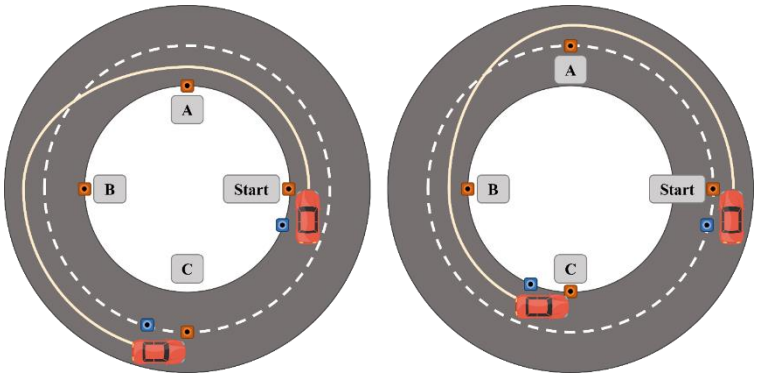

Figure 90. Layout and execution of the constant speed traffic circle lane change maneuver

Table 44. List of DVs for Scenario 4.1 (English units)

r (ft)	$a_{y,\max}$ (g)	v_{target} (mph)	Turn direction	Lane change
50	0.3	15	Left	In
50	0.3	15	Left	Out
50	0.3	15	Right	In
50	0.3	15	Right	Out

Table 45. List of DVs for Scenario 4.1 (metric units)

r (m)	$a_{y,\max}$ (m/s^2)	v_{target} (m/s)	Turn direction	Lane change
15.2	2.94	6.7	Left	In
15.2	2.94	6.7	Left	Out
15.2	2.94	6.7	Right	In
15.2	2.94	6.7	Right	Out

Slalom Maneuver

Figure 91 illustrates the cone setup, and Table 46 and Table 47 list the kinematic parameters and cone placements for Scenario 5.0, the slalom maneuver. Lateral acceleration peaked around 0.3 g during the slalom, and the lane width was 12 ft (3.66 m). When setting up the maneuver, cones were evenly spaced throughout the slalom maneuver portion. When executing the test, a minimum of two periods was required, but three slalom periods are desired if space is available. The test procedure is as follows:

1. Begin the test at the target speed, v_{target}, and hold this speed through the first optical gate
2. At cone 1A, begin the slalom; smoothly transition from left to right while holding v_{target}
3. At the end of the slalom periods (cone C), continue traveling at v_{target} and drive past the second optical gate to end the test active flag

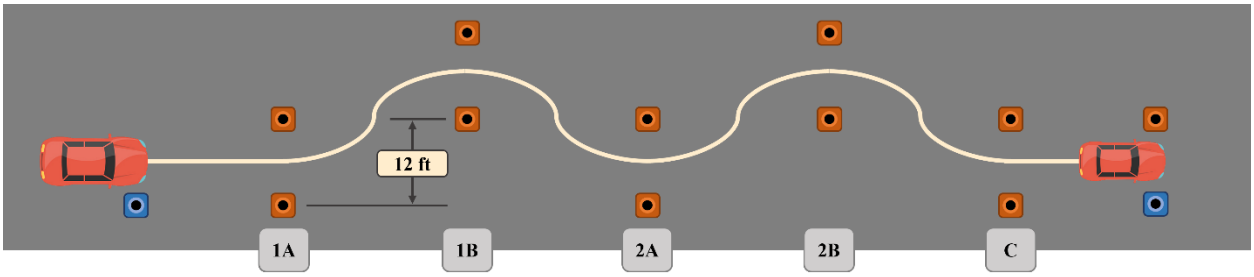

Figure 91. Layout and execution of the constant speed lateral sinusoid maneuver

Table 46. List of DVs for Scenario 5.0 and the respective cone distances required to set up maneuver execution (English units)

v_{target} (mph)	a_y (g)	Start to A (ft)	Half period (ft)	Full period (ft)	C to End (ft)	Total, 2 periods (ft)	Total, 3 periods (ft)
25	0.30	50	82	164	50	428	592
40	0.30	50	115	230	50	560	790

Table 47. List of DVs for Scenario 5.0 and the respective cone distances required to set up maneuver execution (metric units)

v_{target} (kph)	a_y (m/s^2)	Start to A (m)	Half period (m)	Full period (m)	C to End (m)	Total, 2 periods (m)	Total, 3 periods (m)
40	2.94	15.2	25.0	50.0	15.2	130.4	180.4
64	2.94	15.2	35.1	70.1	15.2	170.7	240.8

APPENDIX C: CALCULATION OF METRICS

Lateral Offset

The following steps were used to calculate the ΔY between the test trial and reference path. This method was validated with the Vehicle B's internal ΔY calculation during a slalom maneuver. Results of this method are given in Figure 94 and show agreement with the Vehicle B calculations within approximately one centimeter.

1. Find the three points on the reference path nearest to the current trial point (Figure 92)
2. Build a second-order curve fit through the three nearest neighbor points (Figure 93)
3. Find the minimum distance vector between the current point of interest and the second-order curve by finding the roots of the derivative of the distance function
4. Verify the root is the minimum distance and that the vector between the point of interest and the distance vector is below 90 degrees
5. Take the cross product of the heading and distance vectors to determine if path deviation is left or right

The final equation is given below:

$$\mathbf{\Delta Y} = \mathbf{sgn}(\vec{e} \times \vec{d})\|\vec{d}\|,$$

where $\vec{e}$ represents the heading unit vector, and $\vec{d}$ represents the distance vector.

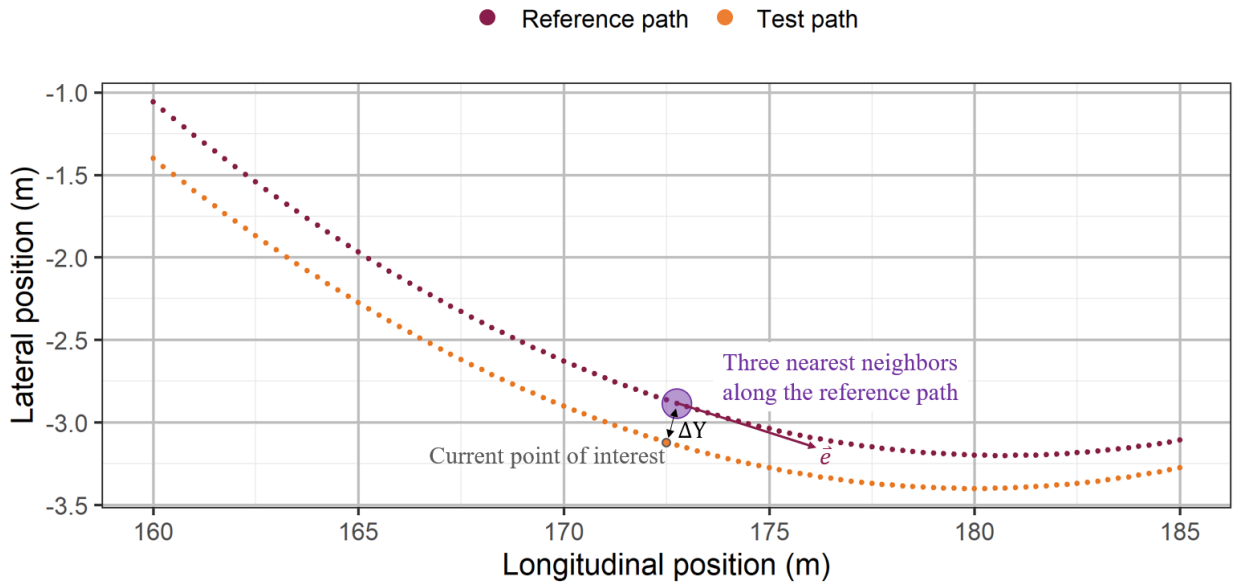

Figure 92. Example calculation of lateral offset relative to the reference path using the methods described above

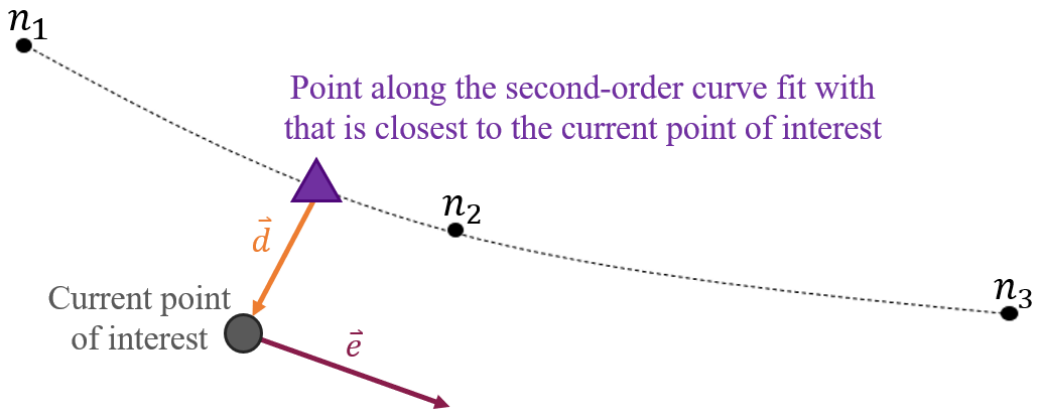

Figure 93. Example of the second-order curve fitted through the closest three points along the reference trajectory

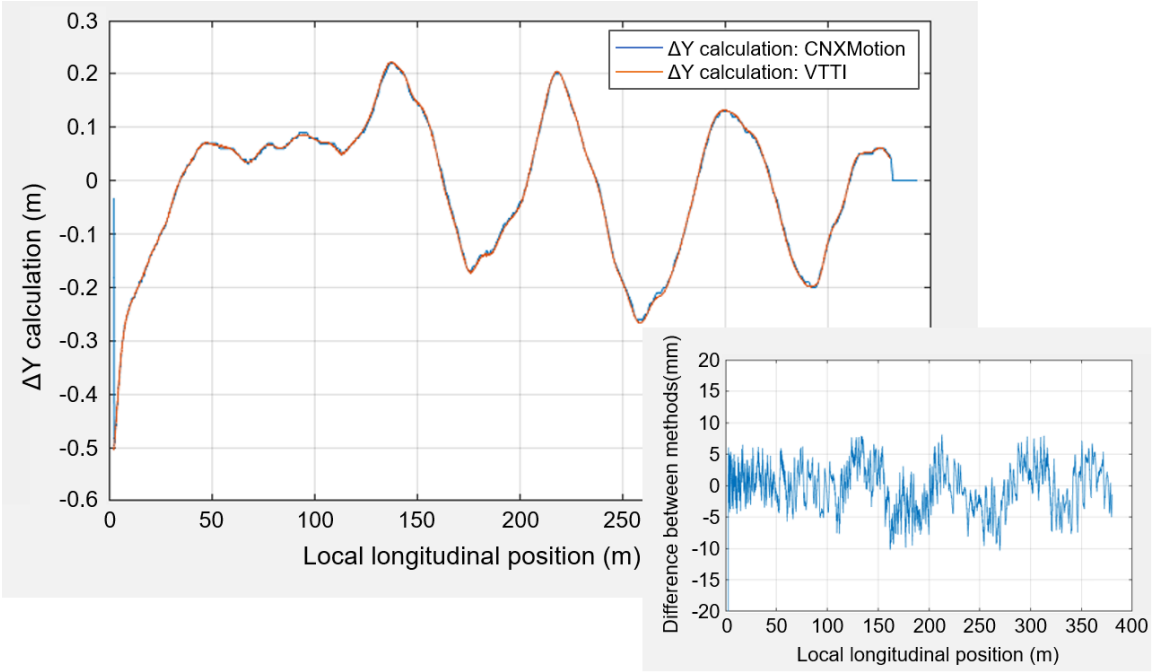

Figure 94. Verification of Vehicle A's ΔY calculation method against Vehicle B's internal calculations. Differences between the methods were within one centimeter

Adjusted Lateral Offset

In addition to ΔY, ΔY_{offset} was created with the intent of mitigating any bias errors in ΔY that may arise due to localization input errors (e.g., heading error). The ΔY_{offset} at each point i in the trial is calculated with the following equation:

$$\Delta Y_{\text{offset},i} = \Delta Y_i - \|\Delta Y_{5\%}\|,$$

where $\|\Delta Y_{5\%}\|$ is the mean ΔY value over the first 5% of distance for the trial.

Δ Variables

For all other Δ variables, the difference is calculated between the current trial point and the reference path's closest point using the following formula:

$$\Delta\Theta_i = \Theta_i - \Theta_{\text{ref}},$$

where Θ represents a kinematic parameter (e.g., yaw rate, lateral acceleration).

Heading

To prevent excessive drift in the heading during stationary portions of maneuvers, the heading was latched and unlatched using the standard set in SAE J2945 for vehicle-to-vehicle (V2V) communications (SAE International, 2016). Below 1.11 m/s, the heading was latched to the previous value and would not unlatch until 1.39 m/s. For maneuvers that start from rest, the heading at the first unlatch point was back propagated to the start of the maneuver.

Local Lag

Local lag defines the distance or time lag of the response speed profile based on the beginning of the current acceleration/braking event. Calculating lag distance/time locally prevented errors from a previous event from affecting the current actions (e.g., an accumulated lag due to acceleration undershoot did not affect the lag during a braking event). When the vehicle is not accelerating or decelerating, the lag time has no meaning and was set to zero.

1. Longitudinal events were categorized as acceleration or braking when the filtered longitudinal acceleration magnitude exceeded 1 m/s^2 until it dropped below 0.2 m/s^2
2. For each point in the test trial, if current point is in a longitudinal event, find the point along the reference path with the closest speed in the current longitudinal event
3. Determine local time and local distance difference between trial and point along the reference path with the closest speed

Figure 95 gives an example of the lag metrics. In the example deceleration event, brake initiation was delayed 0.3 s and then the deceleration rate increased, so the two examples have the same stop point. The lag time increases initially during the initial lag period before reducing as the system catches up.

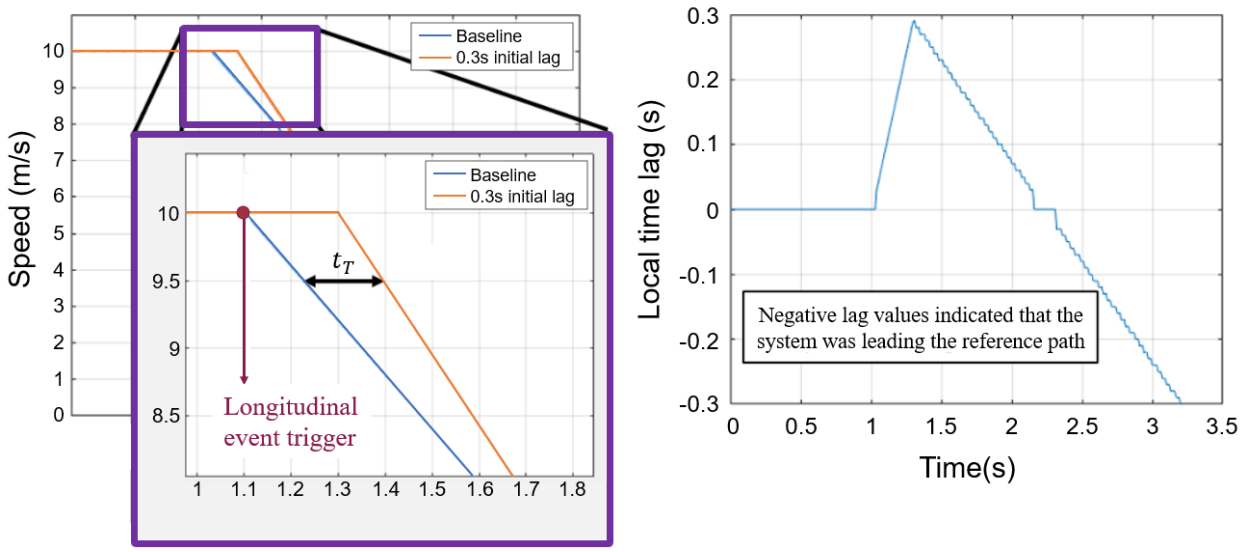

Figure 95. Example calculation of local time lag relative to the reference speed using the methods described above

Coordinates Systems

Local coordinate systems were used throughout the analysis to determine distances and for plotting. To convert the GPS coordinates to local coordinates in meters, the latlon2local function within MATLAB was used with the GPS origin set to the first GPS coordinate of the path (Mathworks, 2020a). These functions provided local coordinates in an east-north-up (ENU) frame. Additionally, all headings were aligned with the following matrix such that zero degrees points along the positive *x*-axis with positive heading angles being counterclockwise:

$$\begin{bmatrix} x' \\ y' \end{bmatrix} = \begin{bmatrix} \sin(\theta) & -\cos(\theta) \\ \cos(\theta) & \sin(\theta) \end{bmatrix} \begin{bmatrix} x \\ y \end{bmatrix}.$$